A Monte Carlo approach to statics and dynamics of quantum fluids

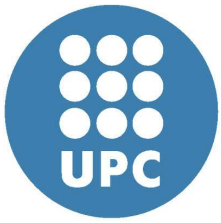

Guillem Ferré Porta

Supervisor: **Prof. Jordi Boronat Medico**

Department de Física
Universitat Politècnica de Catalunya

This dissertation is submitted for the degree of
Doctor of Physics

July 2017

Contents

Chapter 1

Introduction

1.1 Quantum Fluids

The term *quantum fluid* refers to a liquid or a gas at a sufficiently low temperature so that the interaction between its constituent particles is governed by quantum mechanics effects. Superfluids, superconductors and Bose-Einstein condensates are some of the most significant quantum fluids discovered until date.

In mid 17th century, Robert Boyle performed a series of experiments on cold, a subject left untouched since the ancient Greeks, who believed in the existence of a source of all cold. With his experiments, Boyle truly began studying cold and opened the door to further studies. At the beginning of the 18th century, Guillaume Amontons predicted an absolute zero of approximately -240 ºC by extrapolating to zero pressure the relation between air pressure and temperature. This triggered the start of liquefaction of natural gases, which became the staging point for low temperature physics. During the 19th century, chlorine, oxygen, nitrogen were liquefied at $T = 239$ K, $T = 90$ K and $T = 77$ K respectively.

In 1898 James Dewar finally liquefied hydrogen at $T = 23K$ by using a vacuum flask. Previously, in 1895, helium was first isolated on earth by William Ramsay, but it was not until 1908 that Heike Kamerlingh Onnes liquefied it at $T = 4$ K, achievement that led to Onnes being awarded the Nobel Prize in Physics on 1913. Years later, on 1926, Willem Hendrik Keesom was able to solidify helium by applying external pressures.

All these advances allowed to study the behaviour of different materials at very low temperatures. Regarding conductivity, some scientists expected that upon reaching values near absolute zero the electricity current will halt. However,

Onnes instead observed, when using liquid helium to cool mercury, the resistance simply vanishing below $T = 4K$, effect that was termed *superconductivity*.

Around 1930, Keesom [1] observed that the specific heat of liquefied helium displayed a maximum at $T = 2.17$ K, named λ-point. Since such behaviour is expected of a phase transition, the idea developed that liquid helium existed in two phases: helium I for $T > T_\lambda$ and helium II for $T < T_\lambda$, being $T_\lambda = 2.17$ K the critical temperature. Finally, in 1938, experiments performed by Allen and Misener [2], and Kapitza [3] showed that helium II flow without viscosity. This lead Kapitza to coin the term *superfluid* for helium II.

Previously, in 1924, the Bose-Einstein condensate (BEC) was predicted by Satyendra Nath Bose and Albert Einstein. At low enough temperature, a large portion of the quantum particles of a system would condensate into the same quantum state, called the *condensate*, while the remainder would behave conventionally. First thought to be a pathology of the ideal gas, that will disappear as soon as interactions were taken into account, was recovered by Fritz London in 1938 to explain superfluidity in helium II. He pointed out that ^{4}He atoms obey Bose statistics and associated the lambda transition to the formation of a Bose-Einstein condensate, suggesting that superfluid helium II is constituted by atoms occupying the lowest energy single-particle state.

Also, Laszlo Tisza proposed a two-fluid model in order to explain the superfluidity in helium. In his model, the flow of helium II acts as a mixture of two fluids: One, called the superfluid, has neither viscosity nor entropy and can flow without dissipation. The other, called normal fluid, does have a finite viscosity η and carries all the entropy S. The total density ρ is given by the sum of the superfluid density ρ_s and normal-fluid density ρ_n. Is expected that $\rho_s = 0$ at lambda transition, and $\rho_n = 0$ at $T = 0$ K.

In opposition to London, Lev Landau explained the superfluidity phenomenon by introducing the notion of quasiparticle, that is the excitation of the system from ground state with particular values of energy and momentum. Using this concept and without referring explicitly the idea of a Bose-Einstein condensate, Landau postulated that in the two-fluid model proposed by Tisza, the superfluid component is the liquid that remains at ground state. Meanwhile, the normal component is the sum of quasiparticles, excited from the superfluid in increasing numbers as the temperature is increased from absolute zero. If the velocity of the system is not high enough to excite a quasiparticle, the system remains in the ground state and is able to flow without dissipation.

In 1947, Nikolay Bogoliubov studied a Bose gas with weak repulsive interaction, assuming that it would form a Bose-Einstein condensate. The results

showed that the low energy excitations for this system are collective modes with non-zero velocity. This means that the excited states in a Bose system with weak interaction presenting BEC can be described in terms of the quasiparticles conjectured by Landau.

The London conjecture that the BEC fraction is equal to the superfluid fraction was thus proved wrong. In liquid ^{4}He, the superfluid fraction is almost 1 at zero temperature, while the BEC fraction is much lower. However, the general consensus is that superfluidity has to be seen as a consequence of Bose-Einstein condensate, or at least quasi-condensate, as many superfluid effects in liquid ^{4}He are accompanied by a non-zero BEC fraction.

The present understanding of superfluidity comes from the study of liquid helium, since no other condensed Bose system is known to become superfluid below a certain temperature. To gain a deeper insight, it is necessary to study other systems in search of superfluidity. The most plausible candidate is molecular para-hydrogen (pH_2), as first proposed by Ginzburg and Sobyanin in 1972 [4]. However, the main problem is that bulk hydrogen crystallizes at a temperature $T = 13.8$ K, while the temperature in which BEC is expected to appear is ~ 1 K. Despite this, experiments in small clusters of pH_2 at low temperature point out to a superfluid behaviour [5], keeping the interest in this matter alive. Also, non crystalline states of pH_2 can be accessed through numerical simulations.

On the other hand, the development of *laser cooling* in the 1980s provided a way to experimentally obtain gases at very low temperatures, by applying laser beams to the atoms in multiple directions thus slowing them down. In addition, magnetic fields allowed for the creation of traps that, acting as external potentials, confine the atoms. This advancements put BEC within sight again. In 1995, Cornell and Wieman cooled a ^{87}Rb gas down to 0.2μK, achieving the first gaseous BEC [6]. Later in the same year, Ketterle and his group produced a BEC of ^{23}Na atoms using the same technique [7]. From this point forward, more BEC experiments using ultracold gases have been performed, more commonly using rubidium and sodium. These gases typically exist in a temperature range between 100 and 1 nK, and 99% of the atoms lie in the condensed state. Cornell, Wieman and Ketterle shared the Nobel Prize in 2001 for these achievements.

1.2 Monte Carlo methods

Monte Carlo methods are computational algorithms that rely on stochastic sampling in order to obtain numerical results. They have a huge versatility that allows its use in different problems of different nature. They can be used, for

instance, in optimization methods, generating draws from a probability distribution or in numerical integration.

They are widely used in condensed matter physics in order to study systems with many coupled degrees of freedom. Such high number of degrees of freedom makes necessary to describe the system within a statistical approach. Being μ a state of the system, a statistical weight ω_μ is defined that indicates the probability of the system being in that state μ. These weights must satisfy $\sum_\mu \omega_\mu = 1$. The average of any observable O can then be calculated as

$$\langle O \rangle = \sum_\mu O_\mu \omega_\mu \ . \tag{1.1}$$

Of course, this sum is performed over an infinite number of states and can be solved analytically only in a few special cases. Using Monte Carlo methods, instead of requiring all the states in order to integrate equation 1.1, we sample the states that the system can occupy and compute the observable over this sampled states.

For a classical system with temperature T, the probability distribution of its states is given by the Boltzmann distribution

$$\omega_\mu = \frac{1}{Z} e^{-\beta E_\mu} \ , \tag{1.2}$$

where $Z = \sum_\mu e^{-\beta E_\mu}$ is the partition function, $\beta = 1/k_B T$ and E_μ is the energy of the state μ. With this, we obtain an approximation for the observable O,

$$\langle O \rangle_{M,p_\mu} = \frac{\sum_{i=1}^{M} O_{\mu_i} p_{\mu_i}^{-1} e^{-\beta E_{\mu_i}}}{\sum_{i=1}^{M} p_{\mu_i}^{-1} e^{-\beta E_{\mu_i}}} \ , \tag{1.3}$$

where we have sampled the system over M states μ_i according to a probability p_μ, which is a probability distribution similar to the one of the simulated system. This is called *importance sampling*, and is a fundamental part of the Monte Carlo methods. This approximation $\langle O \rangle_{M,p_\mu}$ is a gaussian variable with mean value $\langle O \rangle$ and with standard deviation $\propto 1/\sqrt{M}$. By increasing the number of sampled states M, the approximation of $\langle O \rangle$ becomes better. The choice of a good probability distribution for the importance sampling greatly improves the accuracy of the approximation.

Taking into account all that, we now need a way to sample an arbitrary probability distribution p_μ, as the pseudo-random number generators commonly used in computer applications are able to sample uniformly the real numbers in the interval $[0, 1)$. We need to use this as a basis for the sample of any

probability distribution $p(x)$. The *Metropolis algorithm* [8] provides an effective method to solve this despite the analytical complexity or the dimensionality of the problem.

Based on the theory of the Markov chains, the Metropolis algorithm makes use of the evolution of a stochastic process $\Pi(x|y)$ that satisfies the detailed balance condition with $p(x)$:

$$\Pi(x|y)p(y) = \Pi(y|x)p(x) \ . \tag{1.4}$$

The choice of $\Pi(x|y)$ needs only to satisfy this condition, and is convenient to write it as

$$\Pi(x|y) = T(x|y)A(x|y) \ , \tag{1.5}$$

where $T(x|y)$ is a stochastic process that we can sample, and $A(x|y)$ indicates the probability of accepting the change from configuration y to x sampled according to $T(x|y)$.

Commonly, $T(x|y)$ is chosen symmetric, $T(x|y) = T(y|x)$, and the Metropolis algorithm fixes $A(x|y)$ according to

$$A(x|y) = \min\left(1; \frac{T(y|x)p(x)}{T(x|y)p(y)}\right) = \min\left(1; \frac{p(x)}{p(y)}\right) \tag{1.6}$$

In the end, following this implementation yields a number of steps one must perform in order to accept a change in a state. Being x_i the i-th state in a sequence of random states, we generate a new state x' using the stochastic process $T(x'|x_i)$. We evaluate $A(x'|x_i) = \alpha \leq 1$, according to equation 1.6. The change from x_i to the new state x' is accepted with a probability α. This means, drawing a random number $r \in [0, 1)$, and verifying if $r < \alpha$. If accepted, $x_{i+1} = x'$, and if refused $x_{i+1} = x_i$. The same procedure is repeated for further states.

Despite is ability to sample any probability distribution, the Metropolis algorithm present two weak points. First, is only correct asymptotically. Second, two following variables in the sampled sequence are strongly correlated between each other.

The first problem can be avoided by thermalizing the system before computing any observable, thus discarding a certain number of steps that belong to transient regimes. The correlation between sampled variables can be relieved by performing *data blocking*, that consist in diving a sequence of M variables among N blocks, each composed by $K = M/N$ variables. By estimating the

desired observables on each of these blocks, we obtain a set of N values that, for a large enough K are to be considered statistically independent.

In this thesis we will use Monte Carlo methods in order to solve the many-body nature of quantum systems. These Monte Carlo methods applied to quantum systems are referred as Quantum Monte Carlo (QMC) methods, and will be explained in more detail in further chapters.

1.3 Thesis objectives and outline

The main objective of this thesis is to study static and/or dynamic properties of a set of quantum fluids by means of quantum Monte Carlo (QMC) techniques, mainly using the path integral formalism to obtain results both at zero and finite temperature.

The outline of the thesis is the following:

2. In Chapter 2 we present all the details regarding the Path Integral Monte Carlo method used in the other chapters, as well as its extension at ground state known as Path Integral Ground State. After introducing the basic formalism, we comment on the action we have used, as well as its comparison with other existent approximations which aim is to see if our action can be improved. We also comment on how to construct a parallelization scheme for the Path Integral Monte Carlo method, as well as the advanced sampling techniques we have used in our calculations. Finally, we comment on the physical observables whose implementation we have added in our code.

3. In Chapter 3 we show the results obtained for the phase diagram of a one-dimensional Coulomb gas, obtained using the Path Integral Monte Carlo method. The phase diagram has been constructed mainly by calculating energetic and structural properties of the one-dimensional Coulomb gas. This results extend previous knowledge of different phases in the one-dimensional Coulomb gas at zero temperature.
   This work has been published in:
   G. Ferré, G. E. Astrakharchik, and J. Boronat. "Phase diagram of a quantum Coulomb wire". *Phys. Rev. B* **92**, 245305, (2015).

4. In Chapter 4 we study different proposals for quasi-one-dimensional para-H_2 and how starting from pure one-dimensional systems affects the Luttinger parameter. This is done at zero temperature using Path Integral

Ground State. As para-hydrogen is an important candidate to superfluidity, the main idea behind study a quasi-one-dimensional system is to reduce dimensionality in order to soften intermolecular attraction.
The main results from this work has been published in:
G. Ferré, M. C. Gordillo, and J. Boronat. "Luttinger parameter of quasi-one-dimensional para$-H_2$". *Phys. Rev. B* **95**, 064502, (2017).

5. In Chapter 5 we show the results of our extensive study of the dynamic structure factor for the ^{4}He. Using Path Integral Monte Carlo, we compute the intermediate scattering function at different temperatures and perform an inversion in order to gain access at the dynamics of the system. Despite the ill-posed problem of this inversion, we obtain results in qualitative agreement with the experiments and prove that our method, despite having to yield with inversion problems, obtained better numerical results for ^{4}He at finite temperature than the ones previously in the bibliography.
The main results from this work have been published in:
G. Ferré and J. Boronat. "Dynamic structure factor of liquid ^{4}He across the normal-superfluid transition". *Phys. Rev. B* **93**, 104510, (2016).
G. Ferré, R. Rota, and J. Boronat. "Momentum Distribution of Liquid ^{4}He Across the Normal-Superfluid Phase Transition". *Journal of Low Temperature Physics* **187**, 390–397, (2017). ISSN: 1573-7357.
W. Dmowski et al. "Observation of dynamic atom-atom correlation in liquid helium in real space". *Nature Communications* **8**, 15294, (2017).

6. Finally, in Chapter 6 we work on a method to sample complex-time correlation functions whose aim is to obtain better dynamic structure factor functions than the ones obtained via pure imaginary-time correlation functions. This model has already been tested for single particle in an external potential. Our aim is to test it for multi-particle systems, and to see if we can still recover good results at a reasonable high complex-time when the number of particles is closer to the typical simulation values of real systems.

Chapter 2

Path Integral Monte Carlo method

In this chapter we introduce the Path Integral Monte Carlo method, the main Quantum Monte Carlo method used during the development of this thesis. We begin with a brief introduction on the various Quantum Monte Carlo methods that are used in order to solve quantum many-body problems. After that, we discuss the theoretical basis for the Path Integral Monte Carlo (PIMC) method. We comment on the various approximations that can be used to optimize the calculations, as well as explain how the sampling is performed. After that, we discuss how different properties are computed. Finally, we focus on the main differences between the Path Integral at Ground State (PIGS) and PIMC.

2.1 Quantum Monte Carlo methods

The term Quantum Monte Carlo (QMC) encompasses all the Monte Carlo methods aimed at the study of quantum systems, by determining the quantum expectation values of observable properties. In QMC, the multi-dimensional integrals that arise from the many-body problem formulation are handled via the Monte Carlo method. In fact, QMC methods are the most accurate tool to deal with ground-state properties. In the case of bosonic systems, these methods are able to produce essentially exact results for its equation of state and structural properties, that are in both cases in close agreement with experimental data [9]. On the other hand, they provide an approximate but very accurate description for fermionic systems. This approximation for the fermionic systems is due to the *sign problem*: the wave function is not positive defined as it must be antisymmetric under particle permutations. As it is not positive, it fails to be used

as a probability distribution that could be sampled via Monte Carlo methods. Importantly, QMC methods are not restricted to the limit of zero temperature and are equally powerful to deal with finite temperatures through the sampling of the statistical density matrix, as it is the case of Path Integral Monte Carlo (PIMC) method.

The evolution of QMC methods is strongly connected with the increasing interest in the study of ^{4}He condensed phases. Variational Monte Carlo (VMC) method was presented by McMillan [10], where he uses the expectation values of the many-body wave functions introduced by Jastrow [11] in conjunction with the Metropolis algorithm [8] (see Section 1.2) in order to sample distribution functions. This method provides an upperbound for the ground-state energy of liquid ^{4}He, which is in close agreement with experimental results. In essence, VMC is not different from any variational method except in the use of Monte Carlo techniques in order to evaluate the multi-dimensional integrals.

An improvement over the previous method is the Diffusion Monte Carlo (DMC) method [12], which provides exact results for the ground state of bosonic systems. It works solving the imaginary-time Schrödinger equation introducing importance sampling through a trial wave function. DMC is numerically exact for bosons since it could find the exact ground state energy for any quantum system, within given errors. The algorithm scales polynomically with the system size for bosons, making it one of the most efficient methods when dealing with bosonic systems at zero temperature [9].

The issues involving DMC simulations with fermions arise from the *sign problem*. As explained previously, the antisymmetry in the fermionic wave function make it unable to be used as a probability distribution that can be sampled via Monte Carlo. In order to solve that, one can use Fixed Node Diffusion Monte Carlo, that is done by performing a DMC simulation while imposing the nodes of a model trial wave function [12].

All the previous methods tackle the simulation of many-body quantum systems at zero temperature. On the other hand, the Path Integral Monte Carlo (PIMC) method [13, 14] provides a fundamental approach to the study of interacting many-body systems at low temperature [15, 16]. As commented before, PIMC relies in the sampling of the thermal density matrix. By using its convolution property, one can estimate the density matrix at low temperature from their knowledge at a higher temperature where the system is well described by classical statistical mechanics [17–19]. As suggested by Feynman [18], an isomorphism exists between the canonical partition function of quantum particles to that of classical polymers. PIMC exploits this idea by mapping a finite-temperature

quantum system to a classic system of polymers [20, 21]. Up to recently the implementation of this method by Ceperley [14] was the conventional one, but it meets important problems when trying to determine superfluid properties. In this sense, the *worm algorithm* [22] presents a different approach to the standard PIMC method that successfully samples the permutation space. More extensive information about the Path Integral Monte Carlo method theory and implementation will be introduced in the following sections.

As it was the case at zero-temperature QMC calculations, the PIMC method must also undergo some changes in order to deal with simulations of fermionic systems. In this case, the changes are computationally more expensive since the model deals with the nodes of the density matrix instead of the ones of the wave function. A generalization of the Fixed Node approximation done at zero temperature for the DMC method can be done in the PIMC method framework, called Restricted Path Integral Monte Carlo [23]. However, this method loses consistency near the critical point.

One can extend the path integral formalism from finite temperature to the ground state, in what is known as Path Integral Ground State (PIGS) [24–26]. By noticing an equivalence between the Green's function used in DMC-like methods and the thermal density matrix, one can use the path integral formalism from PIMC in order to achieve the ground state starting from an initial trial wave function. This is done by systematically improving the initial wave function used in the simulation. More detailed information about the PIGS method can be found at section 2.6.

2.2 The Path Integral Monte Carlo method

As introduced in the previous section, the PIMC method relies on the sampling of the thermal density matrix, as the properties of a quantum system in thermal equilibrium can be obtained from it [18]. The thermal density matrix operator of a quantum system with Hamiltonian $\hat{H}$ at a temperature T is given by

$$\hat{\rho} = \frac{e^{-\beta \hat{H}}}{Z} \ , \tag{2.1}$$

where $\beta = 1/(k_B T)$, k_B is the Boltzmann constant, and $Z = \mathrm{Tr}(e^{-\beta \hat{H}})$ is the partition function. The Hamiltonian can be descomposed as $\hat{H} = \hat{K} + \hat{V}$, being $\hat{K}$ and $\hat{V}$ the kinetic and potential operators respectively. In a bulk system of

N interacting particles, this operators can be written as

$$\hat{K} = -\frac{\hbar^2}{2m}\sum_{i=1}^{N}\nabla_i^2 \tag{2.2}$$

$$\hat{V} = \sum_{i<j}^{N} V(r_{ij}) \tag{2.3}$$

The knowledge of $\hat{\rho}$ allows for the calculation of the expected value of any operator $\hat{O}$,

$$\langle\hat{O}\rangle = \mathrm{Tr}(\hat{\rho}\,\hat{O}) \ , \tag{2.4}$$

which in coordinate representation turns to

$$\langle\hat{O}\rangle = \int d\boldsymbol{R}\ \rho(\boldsymbol{R},\boldsymbol{R};\beta)\,O(\boldsymbol{R}) \ , \tag{2.5}$$

with $\boldsymbol{R} = \{\boldsymbol{r}_1,\ldots,\boldsymbol{r}_N\}$ for an N-particle system and $\rho(\boldsymbol{R}_1,\boldsymbol{R}_2;\beta) = \langle\boldsymbol{R}_2|\hat{\rho}|\boldsymbol{R}_1\rangle$. One can also write the partition function as

$$Z = \int d\boldsymbol{R}\ \rho(\boldsymbol{R},\boldsymbol{R};\beta) \tag{2.6}$$

As for the product property, the product of two density matrices, $e^{-(\beta_1+\beta_2)\hat{H}} = e^{-\beta_1\hat{H}}e^{-\beta_2\hat{H}}$ is a density matrix. One can write this property in coordinate representation, which gives rise to the convolution property:

$$\rho(\boldsymbol{R}_1,\boldsymbol{R}_3;\beta_1+\beta_2) = \int d\boldsymbol{R}_2\ \rho(\boldsymbol{R}_1,\boldsymbol{R}_2;\beta_1)\rho(\boldsymbol{R}_2,\boldsymbol{R}_3;\beta_2) \ , \tag{2.7}$$

The noncommutativity of the quantum operators $\hat{K}$ and $\hat{V}$ makes impractical direct calculations of the partition function 2.6. In PIMC, this can be solved by applying some approximations to the term $e^{-\beta\hat{H}}$, beginning by making use of the convolution property.

By applying the product property M times we obtain the density matrix at a temperature $\beta = 1/T$ as the product of M density matrices at the temperature $\tau = \beta/M = 1/MT$:

$$e^{-\beta\hat{H}} = (e^{-\tau\hat{H}})^M = (e^{-\tau(\hat{K}+\hat{V})})^M \ , \tag{2.8}$$

Deep in the quantum regime, i.e., at very low temperature, the estimation of the density matrix for a many-body system is obviously a hard problem. However,

the convolution property of $\hat{\rho}$, expressed as Eq. 2.8 in coordinate representation,

$$\rho(\boldsymbol{R}_1, \boldsymbol{R}_{M+1}; \beta) = \int d\boldsymbol{R}_2 \dots d\boldsymbol{R}_M \prod_{\alpha=1}^{M} \rho(\boldsymbol{R}_\alpha, \boldsymbol{R}_{\alpha+1}; \tau) \ , \tag{2.9}$$

with M an integer and $\tau = \beta/M$, shows how to build the density matrix at the desired temperature T from a product of density matrices at a higher temperature MT. Is important to notice that the thermal density matrix operator $\hat{\rho}$ (Eq. 2.1) is formally equivalent to an evolution operator in imaginary time $t = i\beta$. From this feature, we may understand Eq. 2.9 as an evolution in imaginary time from an initial configuration $\boldsymbol{R}_1$ to a final configuration $\boldsymbol{R}_{M+1}$, rewritten with a series of intermediate steps $\boldsymbol{R}_2 \dots d\boldsymbol{R}_M$, that define a discrete path in the space of configurations. As the time increment approaches zero, the path becomes continuous.

As commented previously, one key aspect of the PIMC method is its ability to map a quantum N-particle system into a classical system of N x M particles [18]. These M classical particles are termed *beads*, and each one of them corresponds to a configuration $\boldsymbol{R}_\alpha \in (\boldsymbol{R}_1 \dots \boldsymbol{R}_M)$ that arises from Eq. 2.9. From this, one can reinterpret the Eq. 2.5 as a classical configuration integral, where

$$S\left(\boldsymbol{R}_{\alpha+1}, \boldsymbol{R}_\alpha; \tau\right) = -\ln\left[\rho\left(\boldsymbol{R}_{\alpha+1}, \boldsymbol{R}_\alpha; \tau\right)\right] \tag{2.10}$$

is an analogous to a classical potential energy divided by a fictitious temperature. In Eq. 2.10, the function S is called *action* and specifies the interaction between the *beads* in the classical polymer mapping of the quantum system. We can rewrite the thermal density matrix from Eq. 2.9 using the action as

$$\rho(\boldsymbol{R}_1, \boldsymbol{R}_{M+1}; \beta) = \int d\boldsymbol{R}_2 \dots d\boldsymbol{R}_M \prod_{\alpha=1}^{M} e^{-S(\boldsymbol{R}_1, \boldsymbol{R}_{M+1}; \beta)} \ . \tag{2.11}$$

The action used on the PIMC algorithm depends on the thermal density matrix approximation chosen, but in the end one can usually split it into kinetic and potential contributions. It is important to note that the density matrix shown in equation 2.11 is for particles without symmetry. If we want to take into account symmetry, we have to use the general form

$$\rho_{B/F}(\boldsymbol{R}_1, \boldsymbol{R}_{M+1}; \beta) = \frac{1}{N!} \sum_{\mathcal{P}} (\pm 1)^P \rho(\boldsymbol{R}_1, \mathcal{P}\boldsymbol{R}_{M+1}; \beta) \ . \tag{2.12}$$

The sampling of permutations is explained in detail in section 2.4.2.

2.3 Approximations for the action

As explained in the previous section, the noncommutativity of the quantum operators $\hat{K}$ and $\hat{V}$ force us to make some kind of approximation on Eq. 2.8. For a large enough temperature, the number of convolution terms M will be large so that the convergence to the exact value will be warranted by the Trotter formula [27]

$$e^{-\beta(\hat{K}+\hat{V})} = \lim_{M\to\infty} \left(e^{-\tau\hat{K}} e^{-\tau\hat{V}}\right)^M \ . \tag{2.13}$$

Knowing that by making M large enough we will recover the exact result, our objective is to work with a good approximation that yields converged results while maintaining the number of convolution terms as low as possible. Aiming at this, we can estimate all the commutators between $\hat{K}$ and $\hat{V}$, following the Baker-Campbell-Hausdorff formula

$$e^{-\tau(\hat{K}+\hat{V})} = e^{-\tau\hat{K}} e^{-\tau\hat{V}} e^{-\frac{\tau^2}{2}[\hat{K},\hat{V}]} e^{-\frac{\tau^3}{6}\left(2[\hat{V},[\hat{K},\hat{V}]]+[\hat{K},[\hat{K},\hat{V}]]\right)} \ldots \ . \tag{2.14}$$

The first approximation one can think of when looking at Eq. 2.14 is the called *primitive action* or *primitive approximation* (PA). In the limit of high temperatures, small imaginary time τ, we can neglect the terms of higher order on the Baker-Campbell-Hausdorff to obtain

$$e^{-\beta(\hat{K}+\hat{V})} \simeq e^{-\beta\hat{K}} e^{-\beta\hat{V}} \ . \tag{2.15}$$

Taking that into account that $\rho(\boldsymbol{R}_1, \boldsymbol{R}_2; \beta) = \langle \boldsymbol{R}_2 | \hat{\rho} | \boldsymbol{R}_1 \rangle$, we can work with the operators separately. For the kinetic operator we get

$$\langle \boldsymbol{R}_\alpha | e^{-\tau\hat{K}} | \boldsymbol{R}_{\alpha+1} \rangle = \left(\frac{1}{4\pi\lambda\tau}\right)^{dN/2} e^{-\frac{(\boldsymbol{R}_{\alpha+1}-\boldsymbol{R}_\alpha)^2}{4\lambda\tau}} \ , \tag{2.16}$$

with d as the dimensionality of the system, $\lambda = \hbar^2/2m$ and defining $(\boldsymbol{R}_{\alpha+1} - \boldsymbol{R}_\alpha)^2 = \sum_{i=1}^{N} (r_{i,\alpha+1} - r_{i,\alpha})^2$. For the potential operator we obtain

$$\langle \boldsymbol{R}_\alpha | e^{-\tau\hat{V}} | \boldsymbol{R}_{\alpha+1} \rangle = e^{-\tau V(\boldsymbol{R}_\alpha)} \delta\left(\boldsymbol{R}_\alpha, \boldsymbol{R}_{\alpha+1}\right) \tag{2.17}$$

with $V(\boldsymbol{R}_\alpha) = \sum_{i<j} V(r_{ij,\alpha})$, where i and j refer to the indices of the particles.

Finally, using equations 2.15, 2.16, 2.17 on 2.9 one gets the thermal density matrix for the primitive action

$$\rho(\boldsymbol{R}_1, \boldsymbol{R}_{M+1}; \beta) \simeq \int d\boldsymbol{R}_2 \dots d\boldsymbol{R}_M \prod_{\alpha=1}^{M} \left(\frac{1}{4\pi\lambda\tau}\right)^{dN/2} e^{-\frac{(\boldsymbol{R}_{\alpha+1}-\boldsymbol{R}_\alpha)^2}{4\lambda\tau}} e^{-\tau V(\boldsymbol{R}_\alpha)} , \tag{2.18}$$

which is a $dN(M-1)$-dimensional integral. The expectation value of any observable (Eq. 2.5) is then written as

$$\langle \hat{O} \rangle \simeq \int \prod_{\alpha=1}^{M} d\boldsymbol{R}_\alpha O(\boldsymbol{R}_\alpha) \rho(\boldsymbol{R}_\alpha, \boldsymbol{R}_{\alpha+1}; \tau) , \tag{2.19}$$

We can take advantage from the classical mapping of the PIMC method, commented in the previous section, to write Eq. 2.18 using the positions of the N x M particles that compose the classical system analogy.

$$\rho_{PA}(\boldsymbol{R}_1, \boldsymbol{R}_{M+1}; \beta) = \left(\frac{1}{4\pi\lambda\tau}\right)^{dNM/2} \int d\boldsymbol{R}_2 \dots d\boldsymbol{R}_M \tag{2.20}$$
$$\exp\left(-\frac{1}{4\lambda\tau} \sum_{\alpha=1}^{M} \sum_{i=1}^{N} (\boldsymbol{r}_{i,\alpha+1} - \boldsymbol{r}_{i,\alpha})^2 - \tau \sum_{\alpha=1}^{M} \sum_{i<j}^{N} V(\boldsymbol{r}_{ij,\alpha})\right) ,$$

with $r_{ij,\alpha} = r_{i,\alpha} - r_{j,\alpha}$, and the i,j identifying the particle index and α the index of the *bead* . Looking at the previous expression, we can see how the thermal density matrix for the primitive action defines an harmonic interaction between neighbouring *beads* within the same particle, as corresponds to a classical polymer formed by a necklace of *beads* connected by ideal springs. For the potential density matrix, one can see an inter-particle potential interaction V between *beads*, thus having the same imaginary time with the same index, between different particles i [18, 28–30].

As one can see, the final result for the thermal density matrix using this approximation (Eq. 2.20) is definite positive, thus it can be thought as a probability distribution that can be computed by Monte Carlo methods by sampling all degrees of freedom using Metropolis algorithm [8]. Furthermore, one can compute observable properties (Eq. 2.19) by averaging over sampled configurations [20].

The exactness of equation 2.20 is linked to the number of convolution terms or *beads* M. At a finite number it is indeed an approximation, but at $M \to \infty$ the result becomes exact as warranted by the Trotter formula 2.13. By increasing M, we can decrease the systematic error that arises from the approximated density matrix. By large enough values of M, this systematic error will be

lower than the unavoidable statistical error present in Monte Carlo calculations due to its stochastic essence, meaning that we could recover the exact value of the expectation value 2.19. This is the reason why the PIMC method is often referred as an exact method.

Despite all this, in practice the primitive approximation $\rho_{PA}(\boldsymbol{R}_1, \boldsymbol{R}_{M+1}; \beta)$ is not good enough in the study of certain systems. As shown in equation 2.14, the primitive approximation is only accurate up to order τ^2, meaning that its convergence to the exact value of the density matrix is slow as the number of *beads* increases. For certain high temperature systems, with reduced quantum effects, the primitive approximation performs fine. On the other hand, in the study of highly degenerate systems or computations at low temperature, the slow convergence of the primitive action requires an unaffordable large number of *beads* in the simulation. In the end, the solution goes through developing more complex forms for the action that are accurate at larger τ.

The primitive action approximation, as well as the approximations we explain in the next sections, are obtained directly from the exponential $\exp(-\beta\hat{H})$. Another approach that also provides very accurate actions for low temperature is the *pair-product approximation* [31], where the basic block of the PIMC chain is the exact action for two isolated particles. This approximation has been extensively used in the study of superfluidity and it is specially accurate for hard-sphere-like systems such as ^{4}He [14]. Its main flaw is the high complexity of the two-body density matrix when taking into account non-radial interactions.

2.3.1 The Chin action

One way to increase the convergence speed of the primitive approximation is taking into account more terms of the Baker-Campbell-Hausdorff formula (Eq. 2.14). This was done by Takahashi-Imada [32] and, later on, by Li and Broughton [33] in independent works, and approximates the imaginary-time operator as

$$e^{-\tau\hat{H}} \simeq e^{-\tau\hat{K}} e^{-\tau\hat{V}} e^{-\frac{\tau^3}{24}\left[\left[\hat{V},\hat{K}\right],\hat{V}\right]} . \tag{2.21}$$

Compared with the primitive action (Eq. 2.15), it presents a double commutator term which improves the accuracy of the approximation up to order τ^4, but only for the trace (instead of the order τ^2 offered by the primitive approximation). This double-commutator term can be calculated as

$$\left[\left[\hat{V},\hat{K}\right],\hat{V}\right] = \frac{\hbar^2}{m}|\nabla V|^2 . \tag{2.22}$$

Since its dependency is only with the potential, one can write the Takahashi-Imada (TIA) action (Eq. 2.21) as

$$e^{-\tau\hat{H}} \simeq e^{-\tau\hat{K}} e^{-\tau\hat{W}} \ , \tag{2.23}$$

with

$$\hat{W} = \hat{V} + \frac{\tau^2}{24}\left[\left[\hat{V},\hat{K}\right],\hat{V}\right] \ . \tag{2.24}$$

This improvement over the primitive action has been proved in simulations of liquid ^{4}He [34]. The overall number of *beads* needed to reach convergence decreases in a significant number. Despite the global computational effort of computing this action increases due to the need to compute a double-commutator term, the overall improvement of performance is significant.

Another way to improve the performance of the primitive action is through a symplectic expansion as

$$e^{-\tau\hat{H}} = \prod_{i=1}^{n} e^{-t_i\tau\hat{K}} e^{-v_i\tau\hat{V}} \ , \tag{2.25}$$

where $\{t_i, v_i\}$ are parameters to be determined (according to the required accuracy of the approximation). A good choice of these parameters can reduce the error term in the right hand side of the equation, providing thus a better approximation than the primitive action. It is important to note that, since the final multidimensional integral must be defined positive in order to be sampled via Monte Carlo method, all of these coefficients must be positive. However, as proved by the Sheng-Suzuki theorem [35, 36], it is impossible to go beyond second order of τ in 2.25 with the use of only positive coefficients.

In order to overcome this limitation, it is necessary to include terms with the double commutator, as shown in equation 2.21. In its work with symplectic expansions, Chin [37] recovers the result obtained in the Takahashi-Imada approximation if this term is included in the primitive approximation. Later on, Chin and Chen [38] introduced a continuous family of gradient symplectic algorithms, accurate up to the fourth order in the time step. This approach proved its efficiency in solving the Schödinger equation [39], problems in classical mechanics [40], in the implementation of evolution operators in density functional theory [41], and in some PIMC calculations [34]. In further work, Chin performed a complete analytical characterization of these fourth-order propagators, showing that they are fully fourth-order, not only in the trace, and thus improving Takahashi-Imada approximation [42].

Using a symplectic expansion with the double-commutator term yields the expression

$$e^{-\tau\hat{H}} = \prod_{i=1}^{n} e^{-t_i\tau\hat{K}} e^{-v_i\tau\hat{V}} e^{-w_i\tau\left[\left[\hat{V},\hat{K}\right],\hat{V}\right]} , \tag{2.26}$$

where the set of coefficients is now $\{t_i, v_i, w_i\}$. An optimal choice of these coefficients makes the expression 2.26 an effective sixth-order approximation.

From this basis arises the termed Chin action (CA) [34]:

$$e^{-\tau\hat{H}} \simeq e^{-v_1\tau\hat{W}_{a_1}} e^{-t_1\tau\hat{K}} e^{-v_2\tau\hat{W}_{1-2a_1}} e^{-t_1\tau\hat{K}} e^{-v_1\tau\hat{W}_{a_1}} e^{-2t_0\tau\hat{K}} , \tag{2.27}$$

where

$$\hat{W}_{a_1} = \hat{V} + \frac{u_0}{v_1} a_1\tau^2 \left[\left[\hat{V},\hat{K}\right],\hat{V}\right] \tag{2.28}$$

contains the potential operator and double-commutator term, in a similar fashion than in the Takahashi-Imada approximation (Eq. 2.24). As we can see, the Chin propagator 2.27 splits the propagator into three smaller time ones.

The double-commutator term has been written previously with a dependency only on the potential (Eq. 2.22). We can further develop this expression as

$$\left[\left[\hat{V},\hat{K}\right],\hat{V}\right] = 2\lambda\sum_{i=1}^{N} |\boldsymbol{F}_i|^2 , \tag{2.29}$$

where we can write

$$\boldsymbol{F}_i = \sum_{j\neq i}^{N} \nabla_i V(r_{ij}) \tag{2.30}$$

as the force acting on a particle i, that will of course take into account only the contributions of *beads* of the same index.

Thus, we can write the thermal density matrix approximation for the Chin action as

$$\rho_{CA}(\boldsymbol{R}_1, \boldsymbol{R}_{M+1}; \beta) = \int d\boldsymbol{R}_2 \ldots d\boldsymbol{R}_M \prod_{\alpha=1}^{M} \rho_{CA}(\boldsymbol{R}_\alpha, \boldsymbol{R}_{\alpha+1}; \tau) , \tag{2.31}$$

where $\rho_{CA}(\boldsymbol{R}_\alpha, \boldsymbol{R}_{\alpha+1}; \tau)$ is an elementary block of the propagator with width τ, and that is split into three as follows:

$$\begin{aligned}\rho_{CA}(\boldsymbol{R}_\alpha, \boldsymbol{R}_{\alpha+1}; \tau) = \left(\frac{m}{2\pi\hbar^2\tau}\right)^{3dN/2} \left(\frac{1}{2t_1^2 t_0}\right)^{dN/2} \int \boldsymbol{R}_{\alpha A}\boldsymbol{R}_{\alpha B} \exp\Bigg[\\ -\frac{1}{4\lambda\tau}\sum_{i=1}^{N}\left(\frac{1}{t_1}(\boldsymbol{r}_{i,\alpha}-\boldsymbol{r}_{i,\alpha A})^2 + \frac{1}{t_1}(\boldsymbol{r}_{i,\alpha A}-\boldsymbol{r}_{i,\alpha B})^2 + \frac{1}{2t_0}(\boldsymbol{r}_{i,\alpha B}-\boldsymbol{r}_{i,\alpha+1})^2\right) \\ -\tau\sum_{i<j}^{N}\left(\frac{v_1}{2}V(r_{ij,\alpha}) + v_2 V(r_{ij,\alpha A}) + v_1 V(r_{ij,\alpha B}) + \frac{v_1}{2}V(r_{ij,\alpha+1})\right) \\ -2\tau^3 u_0\lambda\sum_{i=1}^{N}\left(\frac{a_1}{2}\left|\boldsymbol{F}_{i,\alpha}\right|^2 + (1-2a_1)\left|\boldsymbol{F}_{i,\alpha A}\right|^2 + a_1\left|\boldsymbol{F}_{i,\alpha B}\right|^2 + \frac{a_1}{2}\left|\boldsymbol{F}_{i,\alpha+1}\right|^2\right)\Bigg].\end{aligned} \tag{2.32}$$

In this expression, we have written the Chin action in a symmetrized way. This result can be achieved by substituting the potential density matrix 2.17 for a symmetrized effective potential. In closed polymers, like in the conventional PIMC method, this symmetrized form is not needed, but it becomes necessary when performing the Worm algorithm (section 2.4.2).

To improve the efficiency of the method, one needs to find optimal values for the coefficients that appear in expression 2.27. It is important to note that not all these parameters are independent: imposing that the right side of the factorization is accurate up to τ^4, it is shown [38] that the coefficients must follow

$$\begin{aligned} t_1 &= \frac{1}{2} - t_0 \\ v_1 &= \frac{1}{6(1-2t_0)^2}, \qquad v_2 = 1 - 2v_1 \\ u_0 &= \frac{1}{12}\left(1 - \frac{1}{1-2t_0} + \frac{1}{6(1-2t_0)^2}\right), \end{aligned} \tag{2.33}$$

where only t_0 and a_1 are free parameters, and must fulfill

$$\begin{aligned} 0 \le a_1 \le 1 \\ 0 \le t_0 \le \frac{1}{2}\left(1 - \frac{1}{\sqrt{3}}\right) \end{aligned} \tag{2.34}$$

Chin has already proved to behave like an effective sixth-order approximation in a large variety of systems [34], ranging from simple model systems like one-dimensional harmonic oscillator to more complex quantum systems like ^{4}He. All

the results in this thesis have been obtained by using the this approximation, as shown in equation 2.32.

2.3.2 Other approximations

One of the preliminary objectives of this thesis was to find an action that could surpass the effectiveness of Chin Action in a PIMC calculation. One way to try this goal is to follow the fourth-order expansions proposed by Chin [42, 43]. There, he defines a general $(n-1)$-*bead* propagator of the form

$$\begin{aligned} T^{(4)}_{(n-1)B}(\tau) &= \prod_{i=1}^{n} e^{t_i \tau \hat{K}} e^{v_i \tau \hat{V}} \\ &= e^{v_1 \tau \hat{V}} e^{t_2 \tau \hat{K}} e^{v_2 \tau \hat{V}} e^{t_3 \tau \hat{K}} e^{v_3 \tau \hat{V}} \dots e^{t_n \tau \hat{K}} e^{v_n \tau \hat{V}} \ . \end{aligned} \tag{2.35}$$

We refer to $(n-1)$ as the number of stages, or the number of time slices in which the elementary block of the propagator, of width τ, is split. In this expression, Chin defines $t_1 = 0$, and the rest of coefficients are left-right symmetric ($t_n = t_2$, $t_{n-1} = t_3$, etc...). The number of free parameters will depend on the number of stages chosen in the approximation (Eq. 2.35). They should satisfy

$$\sum_{i=1}^{N} t_i = 1 \tag{2.36}$$

$$v_1 = \frac{1}{2} + \lambda_2(1 - t_2), \qquad v_i = -\lambda_2(t_i + t_{i+1}), \qquad v_N = \frac{1}{2} + \lambda_2(1 - t_N) = v_1$$

$$\lambda_2 = -\frac{1}{2\phi}, \qquad \phi = 1 - \sum_{i=1}^{N} t_i^3 \ .$$

To the general expansion in equation 2.35, Chin adds the double-commutator term $\tau^3 \left[\left[\hat{V}, \hat{K}\right] \hat{V}\right]$. Contrary to what was done in the Chin Action (Eq. 2.27), in this expansion the double-commutator term is equally divided among the time slices created from the elementary block τ. Thus, it shall be accompanied with a coefficient

$$e_{VTV} = \frac{1}{24}\left(\frac{1}{\phi} - 1\right) \ . \tag{2.37}$$

It is also important to note the order in which the operators appear in this new expansion (Eq. 2.35) when compared to the Chin Action (Eq. 2.27). One can rewrite the Chin Action factorization as

$$e^{-\tau \hat{H}} \simeq e^{-t_0 \tau \hat{K}} e^{-v_1 \tau \hat{W}_{a_1}} e^{-t_1 \tau \hat{K}} e^{-v_2 \tau \hat{W}_{1-2a_1}} e^{-t_1 \tau \hat{K}} e^{-v_1 \tau \hat{W}_{a_1}} e^{-t_0 \tau \hat{K}} \ , \tag{2.38}$$

where, in order to write the propagator in a symmetric form, we have separated the $2t_0\tau\hat{K}$ term into two. We can identify this propagator as one of type KVK, meaning that the kinetic operator appears in the extremities of the expansion. The general expansion proposed above in equation 2.35 falls into the VKV propagator type category. In the end, for $n = 4$, one can easily write a propagator of one category in a different order because of the closed paths in PIMC. Thus, in our case, these differences do not introduce important changes in the algorithm. This allows us to write a propagator of one type to take the form of a propagator of the other type. However, at a higher values of n this may not be possible since the order of appearance of the parameters is different from one type to another.

Going back at expression 2.35, for $n = 4$, we recover an approximation with 3 stages that resembles the Chin Approximation in 2.27,

$$T_{3B}^{(4)}(\tau) = e^{v_1\tau\hat{V}}e^{t_2\tau\hat{K}}e^{v_2\tau\hat{V}}e^{t_3\tau\hat{K}}e^{v_2\tau\hat{V}}e^{t_2\tau\hat{K}}e^{v_1\tau\hat{V}}\ , \tag{2.39}$$

with the main difference being that the double-commutator term in this expansion is equally distributed. The free parameter in this expansion is t_2 that must obey $0 < t_2 < 1/2$. The rest of the parameters must follow

$$\begin{aligned} t_3 &= 1 - 2t_2 \\ v_1 &= \frac{1}{2} - v_2, \qquad v_2 = \frac{1}{12t_2(1-t_2)} \\ \phi &= 6t_2(1-t_2)^2, \qquad e_{VTV} = \frac{1}{24}\left(\frac{1}{6t_2(1-t_2)^2} - 1\right) \end{aligned} \tag{2.40}$$

(2.41)

As can be seen, the range of accepted values for the free parameter is greater in this approximation than in the Chin Action. The cause of this is that the accepted range for t_2 is not excluding some values that may yield negative coefficients: some values of t_2 may cause the v_1 coefficient to be negative. In such case, we have a *negative imaginary time-step* in one term of the propagator, breaking with the global positive imaginary time-step evolution. Also, such positive value on a exponential may cause a singularity.

One can do a similar expansion for $n = 5$ and $n = 6$, obtaining 4 and 5-stages propagators respectively. The propagator with 5 stages has two free parameters, t_2 and t_3 that must obey $0 < (t_2 + t_3) < 1/2$. In order to test the performance of these propagators, we have carried out computations similar to the ones done

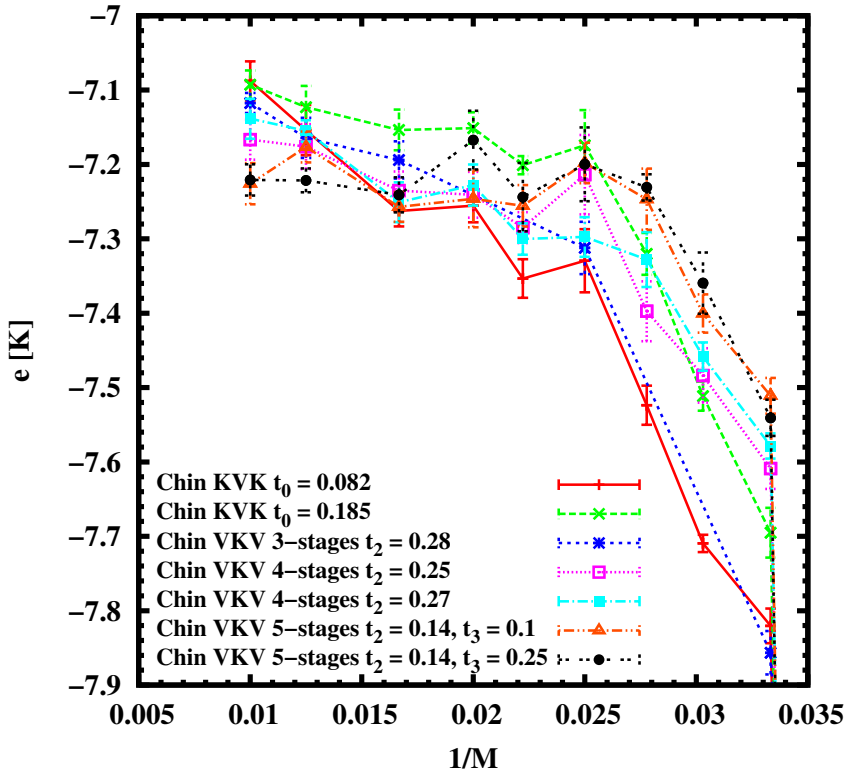

Fig. 2.1 Performance comparison between Chin Action (Eq. 2.27) of type KVK and a general symplectic expansion of type VKV with different number of stages (Eq. 2.35) in a computation of liquid ^{4}He at $T = 1$ K.

for the Chin Action in the past [34]: First, we perform various calculations at high temperature when we check the convergence of each possible free parameter value in the range with the number of *beads*. We then choose these values that present less variance with the number of *beads*. Also, we prioritize the choosing of values that present small differences with surrounding values. After that, we perform a most exhaustive analysis at low temperature with the chosen values with larger number of *beads* to see how they behave at demanding computations.

In Figure 2.1 we show the results obtained using different types of action in a simulation of liquid ^{4}He at $T = 1$ K. Chin KVK stands for the Chin Action presented in the previous section, and we have perform computations using two different t_0 coefficients, while maintaining $a_1 = 0.33$ for both, which makes the contribution from the double commutator term to be splitted equally between the time slies. For Chin VKV we have carried out calculations with differents number of stages, ranging from 3 to 5. The general behaviour observed when

the number of stages increases is a faster convergence, thus needing less *beads*. Despite this gain, the computational cost also increases since each elemental block τ is split into larger number of propagators. In the end, balancing this two factors gives the edge to the Chin Action as showed in the previous section, that yields good results despite being *only* a 3-stages method.

A recent work of Casas also present new families of propagators [44] with coefficients optimized in order to achieve as high order of accuracy as possible. From them, we have tried out a 3-stages VKV-type propagator

$$e^{\tau\hat{H}} = e^{\tau\hat{W}_{b_1,c_1}} e^{a_1\tau\hat{K}} e^{\tau\hat{W}_{b_2,c_2}} e^{a_2\tau\hat{K}} e^{\tau\hat{W}_{b_2,c_2}} e^{a_1\tau\hat{K}} e^{\tau\hat{W}_{b_1,c_1}} \ , \tag{2.42}$$

with

$$\hat{W}_{b_1,c_1} = b_1\hat{V} + c_1\tau^2[[\hat{V},\hat{K}],\hat{V}] \ . \tag{2.43}$$

This is also a symmetric propagator with coefficients $\{a_i, b_i, c_i\}$, being a_1 the free parameter. In general, this value can range $0 < a_1 < 1/2$, as with the generalization made by Chin (Eq. 2.35). However, as we have commented before, some values can yield negative values on other coefficients. If we take $\frac{3-\sqrt{3}}{6} < a_1 < \frac{1}{2}$, all coefficients are always positive except for c_1. To also have c_1 as positive, the range is reduced to $\frac{3-\sqrt{3}}{6} < a_1 < 0.350226$.

The values of the other coefficients are computed from a_1

$$\begin{aligned} a_2 &= 1 - 2a_1 \\ b_1 &= \frac{1 - 6a_1 + 6a_1^2}{12a_1(a_1 - 1)} \\ b_2 &= \frac{1}{12a_1(1 - a_1)} \end{aligned} \tag{2.44}$$

$$\begin{aligned} c_1 &= \frac{-5 + 78a_1 - 474a_1^2 + 1404a_1^3 - 2088a_1^4 + 1440a_1^5 - 360a_1^6}{2880(a_1 - 1)^2 a_1(-1 + 6a_1 - 12a_1^2 + 6a_1^3)} \\ c_2 &= \frac{-5 + 42a_1 - 126a_1^2 + 156a_1^3 - 72a_1^4}{2880(a_1 - 1)^2 a_1(-1 + 6a_1 - 12a_1^2 + 6a_1^3)} \ . \end{aligned} \tag{2.45}$$

The work by Casas also presents some propagators without a double-commutator term, supposed to work better in systems with strong short-distance potentials.

In the figure 2.2 we can see the comparison between this propagator and the Chin Action presented in the previous section. We have performed this comparison for one particle trapped in a one-dimensional Poschl-like well. Firstly, we can compare the results between two 2-stages propagators, with and without the

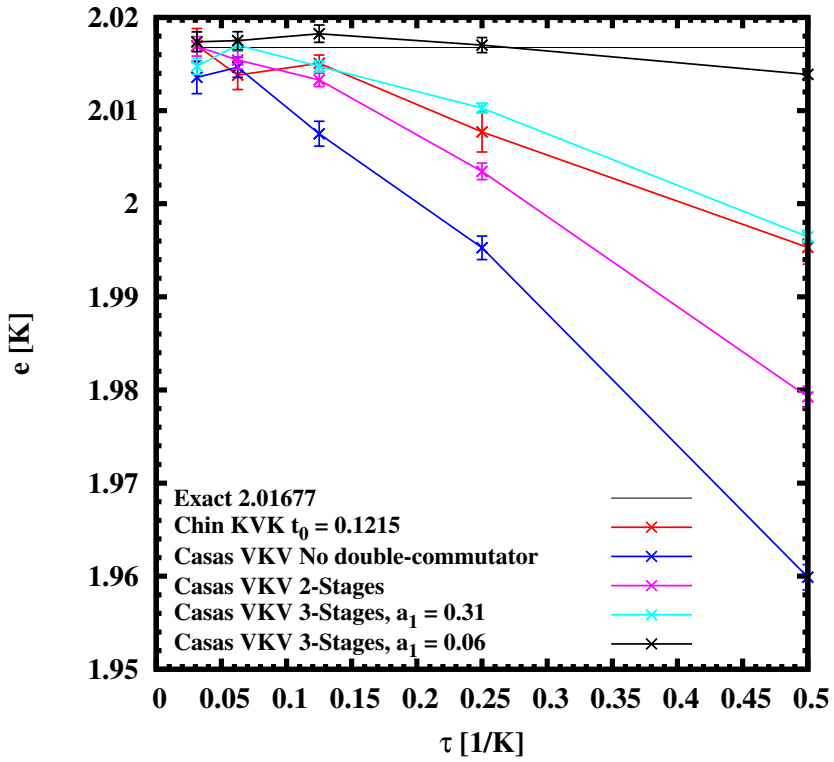

Fig. 2.2 Performance comparison between Chin Action (Eq. 2.27) of type KVK and different types of propagators proposed by Casas [44] in a computation of one particle trapped in a Poschl-type wall potential at $T = 0.5$ K.

double-commutator term. As shown in the figure, despite the difficulties we can find in computing the double-commutator in such strong wall, the propagator with double-commutator converges faster to the exact result. Of course, these 2-stages propagators converge slower than the 3-stages case. Both Chin KVK (Eq. 2.27) and Chin VKV (Eq. 2.42) with $a_1 = 0.31$ converge at the same speed. Using $a_1 = 0.31$ assures us that all the coefficients will have a positive value. We have performed the same calculation with an optimized value that falls out of this range, yielding some negative coefficients. Despite that, as shown in the figure, using $a_1 = 0.06$ yields a much faster convergence of this propagator when comparing to the other 3-stages utilized.

Despite finding this noticeable result, using the same propagator in liquid ^{4}He computations and choosing a a_1 parameter that yields some negative coefficients does not yield such a faster convergence. Instead, the observed results are quite

similar to the ones obtained using Chin general symplectic expansion 2.35 shown in Fig. 2.1.

2.4 Implementing PIMC

In order to implement the PIMC method we take advantage of the classical isomorphism, that allows us to describe the quantum N-body system as a classical system of N closed polymers formed by M particles or *beads*. By proposing movements of these polymers we are able to obtain different configurations $\{\boldsymbol{R}_1 \dots \boldsymbol{R}_M\}$, from which we will be able to sample observables (Eq. 2.19), as will be explained in section 2.5.

As introduced in 1.2, the Metropolis algorithm [8] provides a simple and efficient method to sample a probability distribution function despite its analytical complexity or high dimensionality. Mainly, the implementation of this algorithm in our PIMC method calculation consist of a few steps. First, given a configuration X_i of our quantum system described by a classical system of polymers, we generate a new configuration X_{i+1} using a stochastic process. After that, we evaluate if this new configuration is accepted or not. In the case the change is accepted, we propose a new configuration X_{i+2} and repeat the procedure.

It is important to note that if the sampled variables are computed every time we generate a new configuration, the results will be strongly correlated. This is usually solved by using *data blocking*, this is collecting a sequence of M estimated values in N blocks, each made up of $K = M/N$ elements. Then, we compute the average inside each one of these blocks to obtain a set of N estimated values for our observable that, with a large enough K, will be independent from each other.

Also, the choice of the stochastic process to generate a new configuration will affect the convergence of our method. If the proposed changes are small, the acceptance rate of the updates will be high but the number of steps needed to explore a large enough region of the configuration space, and probably the region of low probability density, will not be sampled. This is usually the case when one uses *bead*-per-*bead* sampling, which moves only one *bead* of a particle i at each update. On the other hand, if the proposed changes are too big, it is easy that the new configuration lands in a region of low probability density and will be rejected frequently. In the end, we aim for an average acceptance rate in the range of 40% - 60%.

Our PIMC method uses two main movements in the sampling of the coordinate space. We will deal with the permutation sampling in later sections (2.4.2).

The acceptance of these movements is computed as the difference between the new action S' after the change and the old one S, as $e^{S(\boldsymbol{R}_\alpha,\boldsymbol{R}_{\alpha+m};\beta)-S'(\boldsymbol{R}'_\alpha,\boldsymbol{R}'_{\alpha+m};\beta)}$ in a standard Metropolis criteria. One of them moves the center of mass of a single particle, displacing all the *beads* of the particle the same random quantity, maintaining the kinetic part of the action (the harmonic potential between neighbouring beads of a particle) intact. The second type of movement is one that only changes the position of a few *beads* of a polymer. This can be done using *bead*-per-*bead* movement, but as explained before this yields a slow convergence of the method. Instead, we will use the *staging* algorithm that will be explained in the next section.

The computational cost of computing the new action S' when we propose a movement of the center of mass of a polymer is computationally expensive since we need to recalculate all the potential interactions between all the *beads*, while the kinetic part of the action remains the same. However, it is not necessary to perform this movement at each step. Usually it is enough to propose a movement of the center of mass once per block per particle.

2.4.1 Staging algorithm

As said before, proposing the displacement of one bead at a time causes the method to converge really slow. For long enough chains, critical slowing down can appear. In order to speed up this convergence, we can propose the displacement of a finite number of neighbouring *beads* of the same particle. However, moving a large enough number of *beads* to have a reasonable acceptance value is costly. For each independent moving bead we will have to recalculate the interactions with the same-index *beads* from other particles and to compute the kinetic part. Being this type of movement the core movement, as is performed at each step of the simulation, creates a rather important slowing down.

The staging algorithm proposes a collective smart displacement of the *beads*. It takes a segment of the polymer and moves it in a way that *beads* within the segment can be considered independent and not coupled. This is done by redefining the position coordinate and the mass of the *beads* in terms of new positions and masses denoted by starred variables.

Let us consider a segment of length l of the polymer chain and consider only the free part of the action. We can write the thermal density matrix on this

segment as

$$\rho(\boldsymbol{R}_j, \boldsymbol{R}_{j+l}; \beta) = \int d\boldsymbol{R}_{j+1} \dots d\boldsymbol{R}_{j+l-1} \prod_{k=j}^{j+l-1} \rho(\boldsymbol{R}_k, \boldsymbol{R}_{k+1}; \tau) \ . \tag{2.46}$$

We are interested in rewritting the consecutive thermal density matrices at temperature $MT = \frac{1}{\tau}$, $\prod_{k=j}^{j+l-1} \rho(\boldsymbol{R}_k, \boldsymbol{R}_{k+1}; \tau)$, in a decoupled way in order to be able to sample them. In order to do so, the following identity can be stated:

$$\begin{aligned}
\rho(\boldsymbol{r}_j, \boldsymbol{r}_{j+1}; \tau) \dots \rho(\boldsymbol{r}_{j+(l-1)}, \boldsymbol{r}_{j+l}; \tau) = \rho(\boldsymbol{r}_j, \boldsymbol{r}_{j+l}; l\tau) \ \times \\
\left[\frac{\rho(\boldsymbol{r}_j, \boldsymbol{r}_{j+1}; \tau)\rho(\boldsymbol{r}_{j+1}, \boldsymbol{r}_{j+l}; (l-1)\tau)}{\rho(\boldsymbol{r}_j, \boldsymbol{r}_{j+l}; l\tau)}\right] \ \times \\
\left[\frac{\rho(\boldsymbol{r}_{j+1}, \boldsymbol{r}_{j+2}; \tau)\rho(\boldsymbol{r}_{j+2}, \boldsymbol{r}_{j+l}; (l-2)\tau)}{\rho(\boldsymbol{r}_{j+1}, \boldsymbol{r}_{j+l}; (l-1)\tau)}\right] \ \times \dots \\
\left[\frac{\rho(\boldsymbol{r}_{j+(l-2)}, \boldsymbol{r}_{j+(l-1)}; \tau)\rho(\boldsymbol{r}_{j+(l-1)}, \boldsymbol{r}_{j+l}; \tau)}{\rho(\boldsymbol{r}_{j+(l-2)}, \boldsymbol{r}_{j+l}; 2\tau)}\right]
\end{aligned}$$

where $\boldsymbol{r}_k$ stands for the position of the *bead* k in the polymer where we are performing the staging. By expanding each of these terms separately, we are able to rewrite the previous expression as

$$\begin{aligned}
\rho(\boldsymbol{r}_j, \boldsymbol{r}_{j+1}; \tau) \dots \rho(\boldsymbol{r}_{j+(l-1)}, \boldsymbol{r}_{j+l}; \tau) = \\
\left(\frac{m}{2\pi\hbar^2 l\tau}\right)^{\frac{1}{2}} \exp\left[-\frac{m}{2\hbar^2 l\tau}\left(\boldsymbol{r}_j - \boldsymbol{r}_{j+l}\right)^2\right] \ \times \\
\prod_{k=0}^{l-2} \left(\frac{m_k}{2\pi\hbar^2\tau}\right)^{\frac{1}{2}} \exp\left[-\frac{m_k}{2\hbar^2\tau}\left(\boldsymbol{r}_{j+k+1} - \boldsymbol{r}^*_{j+k+1}\right)^2\right] \ ,
\end{aligned} \tag{2.47}$$

where we define a reduced mass for each *bead*,

$$m_k = m\left(\frac{l-k}{l-(k+1)}\right) \ , \tag{2.48}$$

and staging coordinates defined as

$$\boldsymbol{r}^*_{j+k+1} = \frac{\boldsymbol{r}_{j+l} + \boldsymbol{r}_{j+k}(l-(k+1))}{l-k} \ . \tag{2.49}$$

A more detailed explanation on how to achieve the staging identity can be found in the thesis by Brualla [45]. As one can see, the density matrix for a *bead* $j+k+1$ depends only in the position of previous *bead* $j+k$ and the staging extremity $j+l$, which is fixed. Thanks to that, we can sample exactly the free density matrix as a set of free gaussians, beginning with the first *bead* $j+1$, since the

extremity j is also fixed. These new positions $\boldsymbol{r}'_{j+k}$ can be obtained by

$$\boldsymbol{r}'_{j+k+1} = \boldsymbol{r}^*_{j+k+1} + \eta\sqrt{\frac{\hbar^2\tau}{m_k}} \ , \tag{2.50}$$

where η is a uniform random number $\eta \in (0,1)$. As the sampling of the free density matrix is exact, we only need to run the Metropolis test on the potential part of the action.

The above expressions for the staging movement can be used directly with an action such as the Primitive Approximation, but need some changes when we want to use it with the Chin Action, since each term of the symplectic expansion has differents constants factors in the kinetic part of the action. An exhaustive explanation on the staging algorithm for the Chin Action can be found in the Appendix A.

2.4.2 Permutation sampling: Worm algorithm

Up to now, the PIMC scheme discussed in the previous chapters holds for systems made up of distinguishable particles. As we want to deal with quantum many-body systems at low temperature, we must take into account the quantum statistics governing the particles. All states, and in extension the thermal density matrix, are either symmetric or antisymmetric with respect to a given permutation. In Bose or Fermi statistics with N particles we can write the thermal density matrix as a sum over all possible permutations of particle labels in one of its two arguments

$$\rho_{B/F}(\boldsymbol{R}_\alpha, \boldsymbol{R}_{\alpha+1}; \beta) = \frac{1}{N!}\sum_{\mathcal{P}} (\pm 1)^P \rho(\boldsymbol{R}_\alpha, \mathcal{P}\boldsymbol{R}_{\alpha+1}; \beta) \ , \tag{2.51}$$

with $\mathcal{P}$ is a permutation of the particle labels, $N!$ is the number of permutations and P is the number of transpositions of these permutations. The term (± 1) depends of the kind of statistics we choose for our systems: $+$ stands for bosons and $-$ for fermions. The expectation value of any observable (Eq. 2.19) can be rewritten as

$$\langle \hat{O} \rangle_{B/F} \simeq \frac{1}{N!}\sum_{\mathcal{P}} \int \prod_{\alpha=1}^{M} d\boldsymbol{R}_\alpha O(\boldsymbol{R}_\alpha)(\pm 1)^P \rho(\boldsymbol{R}_\alpha, \boldsymbol{R}_{\alpha+1}; \tau) \ . \tag{2.52}$$

Despite the complexity of equation 2.52 due to the high number of permutations to tackle with a large number of particles, equation 2.52. expression can still be understood as a probability distribution that can be sampled via Monte

Carlo. For fermions, an additional sign will appear in front of each term, creating contributions to $\langle \hat{O} \rangle$ of opposing signs. This will create a constant noise in our expected results that will make unfeasible the calculations at low temperature or high N. This is what is known as the *sign problem* for fermions, and requires of the introduction of some systematic approximations as, for instance, in the Restricted Path Integral Monte Carlo method [46]. For bosons, Ceperley proposed a scheme to include permutations in PIMC simulations [14], but it was proved to have some performance problems [47] and was not able to provide a good sampling of bosonic permutations, especially when the number of particles increases.

A different approach in the sampling of bosonic permutations can be done by using the *worm algorithm*. Developed first by Prokof'ev *et al.* for interacting bosons in a lattice [48], it was latter extended to continuous-space calculations [22, 49–51].

The worm algorithm works in a extended configurational space given by the union of the ensemble Z, formed by the usual closed polymer configurations, and the ensemble G, where all polymers are closed except for one, which is left open and is referred as the *worm*.

This extension of the configurational space creates the necessity to implement new update methods in order to change from Z to G and vice versa. These updates are referred as *open* and *close*. In the *open* update, we choose a random particle i to become the worm, and propose a movement of a segment of it. The worm then remains open while in the ensemble G, i. e., it does not have a kinetic density matrix between two unique consecutive *beads*. In our case, we perform the *open* update for the last or first numbered *beads*, moving from a configuration $X_i = \{r_1 \dots r_M, r_{M+1} = r_1\}$ to $X_i' = \{r_1 \dots r_M', r_{M+1}' \neq r_1\}$. Similarly, for the *close* update, we propose a movement that moves the system back to the ensemble Z by closing the worm and imposing $r_{M+1} = r_1$.

In order to implement permutations using the *worm algorithm*, we use the *swap* update. The main idea of this movement is to rebuild a free particle path between an open extremity of the worm and a *bead* belonging to a different polymer. In this way we are able to modify both the permutations $p(i)$ and the configuration of the system $\boldsymbol{R}_\alpha$ by means of following updates which do not suffer of low acceptance probability, as was the case of other methods. In the end, performing permutations between only two particles at a time yields a larger chains, while in the algorithm presented by Ceperley [14, 47] a single permutation becomes less probable since the permutations are proposed in groups of three or four particles at a time.

It is important to notice that the probability distribution used to sample configurations while in the ensemble G is different from the one introduced before for the ensemble Z. Therefore, the configurations in the subset G cannot be used to compute diagonal observables (Eq. 2.19), as will be explained in section 2.5. However, they can be used to compute off-diagonal observables, such as the one body density matrix (see section 2.5.6 and 2.5.7).

Summarizing, the worm algorithm is able to sample the exchanges between bosons by means of single particle updates with an acceptance probability comparable to that of other updates in the sampling of polymers. Also, it allows for an efficient description of thermodynamic properties connected to the bosonic statistics of the quantum systems such as superfluidity effects or off-diagonal correlations. More details on the worm algorithm can be found in the PhD. Thesis by Rota [51].

2.4.3 Parallelization

Despite the use of a fourth-order approximation for the action (as is the Chin Action, section 2.3.1), some Path Integral Monte Carlo simulations requires the sampling of quantum systems at very low temperature and/or the use of a large number of particles. Achieving good results for a simulation with a large number of particles or a large number of *beads* when working at low temperature requires an important amount of computational time. Naturally, one can think on parallelization as a way to gain computational efficiency.

As we have commented in previous sections, our PIMC scheme proposes a movement of a single particle at a time, being it either a global translation or a partial segment movement following staging algorithm. The same applies to the movements introduced by the worm algorithm, with the difference that these movements are performed only for the *worm*, while the movement of the center of mass and segment movements are performed once per particle. The costly part of each of these movements arise when computing the probability for the Metropolis algorithm. The kinetic part of the density matrix is not computed, since we are either performing a global translation or moving a segment of the polymer via staging algorithm in all the cases. In this sense, we need to compute only the potential and double-commutator part of the density matrix, that arises from interactions between particles. The computational time of this calculation goes as mN^2, being N the number of particles and m the number of moved *beads*.

One could think in parallelizing this N^2 loop in order to gain speed, but in fact this is not even needed. For performing the Metropolis algorithm we are only interested in the change in the action, so by saving in memory the contribution on each *bead* we can gain speed. Doing it that way reduces mN^2 to mN, since we only need to compute the potential interaction change on the moved *beads*. On the other hand, MN^2 loops will appear in the estimations of certain observables, like the energy per particle. In this cases, paralellizing will indeed yield faster calculations. However, in the end the calculation of the energy per particle is not performed at every step and a significant improvement in this estimation is not a big gain in the global computation time. The same could be said about the movement of the center of mass. This movement is performed once per block for each particle, but always one particle at a time. This means that the only choice for parallelization is to distribute the M *beads* into a k number of threads. This, for a large enough number of *beads*, could provide some speed gain. On the other hand, the more repeated movement is a segment movement, that can be performed more than once per step per particle. The quickness of this update depends on the length of the segment moved, that usually decreases at low temperature in order to achieve the aimed acceptance rate. Despite being a fast update, it is performed so many times that the total time spend in this update is important.

In the end, the time spent computing the movement of the center of mass, estimators with a MN^2 loop, and segment movement will depend on the number of steps per block K and the number of *beads* M. For a large K and small M, most of the computational time will be spent in the segment movement update. For large M and small K, most of the time will be spent on the movement of the center of mass and computation of some observables. The parallelization for these two last methods has already been commented, as it simply consist in parallelize MN loops.

The parallelization of the staging algorithm is more complex. One easy solution is to parallelize the mN loop, as commented before, but the gain is only substantial if the number of moving *beads* m is large, which is usually not the case. A more interesting approach is to propose more than one segment movement at a time. Since the kinetic part of the density matrix is sampled via the staging algorithm, the only part we need to evaluate is the potential and double-commutator part, and these contributions only depend on the same-indexed *beads* of all the other particles. So, in order to perform more than one movement at once, we can divide the total length M of a polymer in a number $j = M/m$ of segments, where m is the number of *beads* moved using staging

algorithm. Each of these segments is updated in a parallelized way following the staging algorithm. Usually, we take each of these segments from different polymers. Of course, the number of parallelized segments must fulfill $j < N$, since otherwise we will probably move a particle more times than the desired each step.

This parallelization of the staging algorithm fastens our segment updates proportional to the number j of parallelized threds. This number is high for a large number of *beads* M and a small segment update length. Usually, this is the case of lower temperature systems.

For instance, we can look at a PIMC simulation of solid ^{4}He crystal hcp at $T = 0.2$ K, with $N = 180$ particles and $M = 480$ *beads*. In order to have a good acceptance rate, the number of moving beads per staging is $m = 10$. In this case, we can perform a parallelization in $j = 48$ different processors. Even only using 8 different processors give us a $\sim 50\%$ time reduction of the staging update. Also, as we have a large number of *beads*, the parallelization on the center of mass movement will also be effective. In the same case as before, we observe a time reduction of $\sim 60\%$. Which one of the two parallelization schemes is more effective depends on the number of steps per block, as commented before.

2.5 Computing properties

Once we have defined which approximation for the action we are using and the chosen strategy for the sampling, it is important to tackle how we can compute properties in our PIMC scheme.

Before explaining the properties one by one, it is interesting to rewrite some of the expressions introduced in previous sections explicitly showing the Chin Action approximation. We can write the partition function (Eq. 2.6) as

$$\begin{aligned} Z =& \frac{1}{N!}\sum_{\mathcal{P}}\left(\frac{1}{4\pi\lambda\tau}\right)^{\frac{3dNM}{2}}\left(\frac{1}{2t_1^2 t_0}\right)^{\frac{dNM}{2}} \\ & \int d\vec{R}_1 d\vec{R}_{1A} d\vec{R}_{1B}...d\vec{R}_{MB}\ \prod_{\alpha=1}^{M}\exp\left[-S(\boldsymbol{R}_\alpha,\boldsymbol{R}_{\alpha+1};\tau)\right], \end{aligned} \tag{2.53}$$

using the condition $\mathcal{P}\boldsymbol{R}_1 = \boldsymbol{R}_{M+1}$, and with $S(\boldsymbol{R}_\alpha, \boldsymbol{R}_{\alpha+1}; \tau)$ being the action for an elementary imaginary time block τ,

$$\begin{aligned} S(\boldsymbol{R}_\alpha,\boldsymbol{R}_{\alpha+1};\tau) = \frac{1}{4\lambda\tau}\sum_{i=1}^{N}\left(\frac{1}{t_1}(\boldsymbol{r}_{i,\alpha}-\boldsymbol{r}_{i,\alpha A})^2+\frac{1}{t_1}(\boldsymbol{r}_{i,\alpha A}-\boldsymbol{r}_{i,\alpha B})^2+\frac{1}{2t_0}(\boldsymbol{r}_{i,\alpha B}-\boldsymbol{r}_{i,\alpha+1})^2\right) \\ +\tau\sum_{i<j}^{N}\left(\frac{v_1}{2}V(r_{ij,\alpha})+v_2V(r_{ij,\alpha A})+v_1V(r_{ij,\alpha B})+\frac{v_1}{2}V(r_{ij,\alpha+1})\right) \\ +2\tau^3u_0\lambda\sum_{i=1}^{N}\left(\frac{a_1}{2}\left|\boldsymbol{F}_{i,\alpha}\right|^2+(1-2a_1)\left|\boldsymbol{F}_{i,\alpha A}\right|^2+a_1\left|\boldsymbol{F}_{i,\alpha B}\right|^2+\frac{a_1}{2}\left|\boldsymbol{F}_{i,\alpha+1}\right|^2\right). \end{aligned} \tag{2.54}$$

In order to write equation 2.54 in a more compact way, one can define the terms

$$T_N^t = \sum_{i=1}^{N}\left(\frac{1}{t_1}(\boldsymbol{r}_{i,\alpha}-\boldsymbol{r}_{i,\alpha A})^2+\frac{1}{t_1}(\boldsymbol{r}_{i,\alpha A}-\boldsymbol{r}_{i,\alpha B})^2+\frac{1}{2t_0}(\boldsymbol{r}_{i,\alpha B}-\boldsymbol{r}_{i,\alpha+1})^2\right), \tag{2.55}$$

$$V_N = \sum_{i<j}^{N}\left(\frac{v_1}{2}V(r_{ij,\alpha})+v_2V(r_{ij,\alpha A})+v_1V(r_{ij,\alpha B})+\frac{v_1}{2}V(r_{ij,\alpha+1})\right), \tag{2.56}$$

$$W_N = \sum_{i=1}^{N}\left(\frac{a_1}{2}\left|\boldsymbol{F}_{i,\alpha}\right|^2+(1-2a_1)\left|\boldsymbol{F}_{i,\alpha A}\right|^2+a_1\left|\boldsymbol{F}_{i,\alpha B}\right|^2+\frac{a_1}{2}\left|\boldsymbol{F}_{i,\alpha+1}\right|^2\right), \tag{2.57}$$

that allows us to write the total action as

$$S(\boldsymbol{R}_\alpha, \boldsymbol{R}_{\alpha+1};\tau) = \frac{1}{4\lambda\tau}\sum_{i=1}^{N}T_N^t+\tau\sum_{i<j}^{N}V_N+2\tau^3u_0\lambda\sum_{i=1}^{N}W_N\,. \tag{2.58}$$

In the next subsection we will write the different estimators of the properties directly specifically for the Chin Action.

2.5.1 Energy per particle

The energy per particle E/N is one of the most important quantities obtainable from our PIMC simulations. At a finite temperature, one can obtain a estimation of the energy by deriving it from the partition function with the formula

$$\frac{E}{N} = -\frac{1}{NZ}\frac{\partial Z}{\partial\beta} = -\frac{1}{NMZ}\frac{\partial Z}{\partial\tau} \tag{2.59}$$

By applying this formula to the definition of the partition function Z (Eq. 2.53) we find the expression:

$$\frac{E_T}{N} = \left\langle\frac{3d}{2\tau}-\frac{1}{MN}\left(\frac{1}{4\lambda\tau^2}T_{MN}^t-V_{MN}-6\tau^2u_0\lambda W_{MN}\right)\right\rangle, \tag{2.60}$$

where the brackets indicate an average over all the configurations $\boldsymbol{R}$ sampled in the PIMC simulation. The terms T^t_{MN}, V_{MN} and W_{MN} stands as the same as the ones appearing previously (Eq. 2.55, 2.56 and 2.57), but with a summation over all the *beads*, i.e. $T^t_{MN} = \sum_{\alpha=1}^{M} T^t_N$. The first term $3d/(2\tau)$ in the formula remembers the energy of a classical ideal gas, $d/(2\beta)$, where d stands as the dimension of the system. However, in equation 2.60 the classic term appears with a dependence with the number of *beads*, and the factor 3 arises from the total number of beads when using the Chin Action.

This is the so called *thermodynamic estimator* for the energy per particle. One can use a formula similar 2.59 to obtain the thermodynamic estimator for the kinetic energy

$$\frac{K}{N} = \frac{m}{N\beta Z}\frac{\partial Z}{\partial m} = -\frac{\lambda}{N\beta Z}\frac{\partial Z}{\partial \lambda} = -\frac{\lambda}{NM\tau Z}\frac{\partial Z}{\partial \lambda} \ , \tag{2.61}$$

and then one can obtain the potential energy by subtracting $V/N = E/N - K/N$. One then obtains

$$\frac{K_T}{N} = \left\langle \frac{3d}{2\tau} - \frac{1}{NM}\left(\frac{1}{4\lambda\tau^2}T^t_{MN} - 2\tau^2 u_0 \lambda W_{MN}\right)\right\rangle \tag{2.62}$$

and

$$\frac{V_T}{N} = \left\langle \frac{1}{NM}\left(V_{MN} + 4\tau^2 u_0 \lambda W_{MN}\right)\right\rangle \ . \tag{2.63}$$

The thermodynamic estimators can be easly implemented in a PIMC scheme but, as we can see in equation 2.60, some of its terms have an important dependence with the number of *beads* M, causing them to become large at small τ. This causes this estimator to have a large variance due to the balancing of two large terms. In order to overcome this problem, is better to use an estimator without any such cancellations. One way to do this is to use the so called *virial estimator* [14, 52]:

$$\begin{aligned}\frac{E_V}{N} = \Bigg\langle \frac{d}{2\beta} &+ \frac{1}{12\lambda N M^2\tau^2}\sum_{\alpha=1}^{M}\sum_{i=1}^{N}\left(\boldsymbol{r}_{i,M+\alpha} - \boldsymbol{r}_{i,\alpha}\right)\left(\boldsymbol{r}_{i,M+\alpha-1} - \boldsymbol{r}_{i,M+\alpha}\right) \\ &+ \frac{1}{2N\beta}\sum_{\alpha=1}^{M}\sum_{i=1}^{N}\left(\boldsymbol{r}_{i,\alpha} - \boldsymbol{r}^C_{i,\alpha}\right)\frac{\partial}{\partial \boldsymbol{r}_{i,\alpha}}\left(U(\boldsymbol{R}_\alpha)\right) \\ &+ \frac{1}{NM}\sum_{\alpha=1}^{M}\frac{\partial U(\boldsymbol{R}_\alpha)}{\partial\tau}\Bigg\rangle\end{aligned} \tag{2.64}$$

where $d/(2\beta)$ is the classical energy and $U(\boldsymbol{R}_\alpha)$ stands for the potential part of the action, which in the Chin Action case is

$$U(\boldsymbol{R}_\alpha) = \tau \sum_{i<j}^{N} V_N + 2\tau^3 u_0 \lambda \sum_{i=1}^{N} W_N \ , \tag{2.65}$$

and

$$\boldsymbol{r}_{i,\alpha}^{C} = \frac{1}{2M} \sum_{l=0}^{M-1} \left(\boldsymbol{r}_{i,\alpha+l} + \boldsymbol{r}_{i,\alpha-l} \right) \ . \tag{2.66}$$

A full derivation of this formula can be found in the PhD. Thesis by Rota [51]. It mainly consist in defining a quantity that can be solved in two ways, by integrating by parts or by computing directly a derivative appearing inside the integral, in a way similar to what is done in this thesis with the virial estimator for the pressure (Appendix C). The last term of the equation 2.64 yields the same results as the equation 2.59 for the thermodynamic estimator, but without the neighbouring *beads* harmonic interaction. Thus, for the Chin Action, the new terms will arise from the third term of equation 2.64.

A full calculation of the virial estimator for the Chin Action can be found in the Appendix B. From the terms that arise from equation 2.64, the final expression for the virial estimator is:

$$\frac{E_V}{N} = \left\langle \frac{d}{2\beta} + \frac{1}{NM} \left(\frac{1}{12\lambda M\tau^2} T_{MN}^{\text{off}} + \frac{1}{2} T_{MN}^{V} + 2\tau^2 u_0 \lambda Y_{MN} \right. \right. \\ \left. \left. + V_{MN} + 6\tau^2 u_0 \lambda W_{MN} \right) \right\rangle \ . \tag{2.67}$$

The potential energy using this estimator is the same as in the thermodynamic estimator (Eq. 2.63), while the kinetic energy is

$$\frac{K_V}{N} = \left\langle \frac{d}{2\beta} + \frac{1}{NM} \left(\frac{1}{12\lambda M\tau^2} T_{MN}^{\text{off}} + \frac{1}{2} T_{MN}^{V} \right. \right. \\ \left. \left. + 2\tau^2 u_0 \lambda (W_{MN} + Y_{MN}) \right) \right\rangle \ . \tag{2.68}$$

For both cases we have defined some terms to ease the reading, as in the case for the thermodynamic estimator and partition function:

$$\begin{aligned} T^{\text{off}}_{MN} = \sum_{\alpha=1}^{M}\sum_{i=1}^{N}\Bigg(&\frac{1}{t_1}\left(\boldsymbol{r}_{i,M+\alpha}-\boldsymbol{r}_{i,\alpha}\right)\left(\boldsymbol{r}_{i,\alpha}-\boldsymbol{r}_{i,\alpha A}\right) \\ &+\frac{1}{t_1}\left(\boldsymbol{r}_{i,M+\alpha A}-\boldsymbol{r}_{i,\alpha A}\right)\left(\boldsymbol{r}_{i,\alpha A}-\boldsymbol{r}_{i,\alpha B}\right) \\ &+\frac{1}{2t_0}\left(\boldsymbol{r}_{i,M+\alpha B}-\boldsymbol{r}_{i,\alpha B}\right)\left(\boldsymbol{r}_{i,\alpha B}-\boldsymbol{r}_{i,\alpha+1}\right)\Bigg)\ , \end{aligned} \tag{2.69}$$

$$\begin{aligned} T^{V}_{MN} = \sum_{\alpha=1}^{M}\sum_{i=1}^{N}\Bigg(&\frac{v_1}{2}(\boldsymbol{r}_{i,\alpha}-\boldsymbol{r}^{C}_{i,\alpha})\boldsymbol{F}_{i,\alpha}+v_2(\boldsymbol{r}_{i,\alpha A}-\boldsymbol{r}^{C}_{i,\alpha A})\boldsymbol{F}_{i,\alpha A} \\ &+v_1(\boldsymbol{r}_{i,\alpha B}-\boldsymbol{r}^{C}_{i,\alpha B})\boldsymbol{F}_{i,\alpha B}+\frac{v_1}{2}(\boldsymbol{r}_{i,\alpha+1}-\boldsymbol{r}^{C}_{i,\alpha+1})\boldsymbol{F}_{i,\alpha+1}\Bigg)\ , \end{aligned} \tag{2.70}$$

$$\begin{aligned} Y_{MN} = \sum_{\alpha=1}^{M}\sum_{i=1}^{N}\sum_{\substack{j=1\\ j\neq i}}^{N}\sum_{a=1}^{d}\sum_{b=1}^{d}\Bigg(&\frac{a_1}{2}(r_{i,\alpha}-r^{C}_{i,\alpha})^{a}T(i,j,\alpha)^{b}_{a}(F_{i,\alpha}-F_{j,\alpha})_{b} \\ &+(1-2a_1)(r_{i,\alpha A}-r^{C}_{i,\alpha A})^{a}T(i,j,\alpha A)^{b}_{a}(F_{i,\alpha A}-F_{j,\alpha A})_{b} \\ &+a_1(r_{i,\alpha B}-r^{C}_{i,\alpha B})^{a}T(i,j,\alpha B)^{b}_{a}(F_{i,\alpha B}-F_{j,\alpha B})_{b} \\ &+\frac{a_1}{2}(r_{i,\alpha+1}-r^{C}_{i,\alpha+1})^{a}T(i,j,\alpha+1)^{b}_{a}(F_{i,\alpha+1}-F_{j,\alpha+1})_{b}\Bigg)\ , \end{aligned} \tag{2.71}$$

with $T(i,j,\alpha)^{b}_{a}$ being a tensor defined by

$$\begin{aligned} T(i,j,\alpha)^{b}_{a} = &\left[\frac{\delta^{b}_{a}}{r_{ij,\alpha}}-\frac{(r_{ij,\alpha})^{b}(r_{ij,\alpha})_{a}}{r^{3}_{ij,\alpha}}\right]\frac{dV(r_{ij,\alpha})}{dr_{ij,\alpha}} \\ &+\frac{(r_{ij,\alpha})^{b}(r_{ij,\alpha})_{a}}{r^{2}_{ij,\alpha}}\frac{d^{2}V(r_{ij,\alpha})}{dr^{2}_{ij,\alpha}} \end{aligned} \tag{2.72}$$

The term T^{off}_{MN} from equation 2.69 arises from the permutations in the system. If there are no permutations, this term would drop to zero since $\boldsymbol{R}_{\alpha+M}=\boldsymbol{R}_{\alpha}$.

2.5.2 Pressure

For computing the pressure of the system, we can follow the same pattern as with the energy per particle. We can compute the thermodynamic estimator by using the definition

$$P=\frac{1}{\beta Z}\frac{\partial Z}{\partial V}\ , \tag{2.73}$$

with the partition function for the Chin action defined at equation 2.53. In order to evaluate this expression, it is convenient to introduce the rescaled coordinates $\boldsymbol{R}^*_\alpha = \boldsymbol{R}_\alpha / V^{1/d}$. By using this coordinates, we obtain

$$P_T = \left\langle \frac{3N}{\tau V} - \frac{1}{2d\lambda M \tau^2 V} T^t_{NM} - \frac{1}{2dVM} T^{pT}_{MN} - \frac{4\tau^2 u_0 \lambda}{dVM} Y^{pT}_{MN} \right\rangle \ , \tag{2.74}$$

where the term $T^t_{NM} = \sum_{\alpha=1}^{M} T^t_N$ (Eq. 2.55) already appears in the thermodynamic estimator of the energy, while the others are similar to the ones appearing in the virial estimator of the energy:

$$\begin{aligned} T^{pT}_{MN} = \sum_{\alpha=1}^{M} \sum_{i=1}^{N} \sum_{\substack{j=1 \\ j\neq i}}^{N} \Bigg(& \frac{v_1}{2} (\boldsymbol{r}_{i,\alpha} - \boldsymbol{r}_{j,\alpha}) \boldsymbol{\nabla}_{i,\alpha} V(r_{ij,\alpha}) \\ & + v_2 (\boldsymbol{r}_{i,\alpha A} - \boldsymbol{r}_{j,\alpha A}) \boldsymbol{\nabla}_{i,\alpha A} V(r_{ij,\alpha A}) \\ & + v_1 (\boldsymbol{r}_{i,\alpha B} - \boldsymbol{r}_{j,\alpha B}) \boldsymbol{\nabla}_{i,\alpha B} V(r_{ij,\alpha B}) + \frac{v_1}{2} (\boldsymbol{r}_{i,\alpha+1} - \boldsymbol{r}_{j,\alpha+1}) \boldsymbol{\nabla}_{i,\alpha+1} V(r_{ij,\alpha+1}) \Bigg) \ , \end{aligned} \tag{2.75}$$

$$\begin{aligned} Y^{pT}_{MN} = \sum_{\alpha=1}^{M} \sum_{i=1}^{N} \sum_{\substack{j=1 \\ j\neq i}}^{N} \sum_{a=1}^{d} \sum_{b=1}^{d} \Bigg(& \frac{a_1}{2} (r_{i,\alpha} - r_{j,\alpha})^a T(i,j,\alpha)^b_a (F_{i,\alpha})_b \\ & + (1 - 2a_1)(r_{i,\alpha A} - r_{j,\alpha A})^a T(i,j,\alpha A)^b_a (F_{i,\alpha A})_b \\ & + a_1 (r_{i,\alpha B} - r_{j,\alpha B})^a T(i,j,\alpha B)^b_a (F_{i,\alpha B})_b \\ & + \frac{a_1}{2} (r_{i,\alpha+1} - r_{j,\alpha+1})^a T(i,j,\alpha+1)^b_a (F_{i,\alpha+1})_b \Bigg) \ , \end{aligned} \tag{2.76}$$

where the tensor $T(i,j,\alpha)^b_a$ is the same as for the energy (Eq. 2.72). As can be seen, similar to the expression for the energy some of the terms in 2.74 appear with a dependence with τ that may cause problems at a large number of *beads*. Therefore, we can use the virial estimator in order to avoid this pathology. A full derivation for both pressure estimators can be found in Appendix C.

$$P_V = \left\langle \frac{N}{V\beta} + \frac{1}{6d\lambda\beta^2 V} T^{\text{off}}_{MN} - \frac{1}{2dVM} T^{pV}_{MN} - \frac{4\tau^2 u_0 \lambda}{dVM} Y^{pV}_{MN} \right\rangle \ , \tag{2.77}$$

where T^{off}_{MN} is the same term that appears in the formula of the virial estimator for the energy (Eq. 2.69), and the other terms are similar to the ones obtained

before,

$$T_{MN}^{pV} = \sum_{\alpha=1}^{M}\sum_{i=1}^{N}\sum_{\substack{j=1\\ j\neq i}}^{N}\Bigg(\frac{v_1}{2}(\boldsymbol{r}_{i,\alpha}^{C}-\boldsymbol{r}_{j,\alpha}^{C})\boldsymbol{\nabla}_{i,\alpha}V(r_{ij,\alpha}) + v_2(\boldsymbol{r}_{i,\alpha A}^{C}-\boldsymbol{r}_{j,\alpha A}^{C})\boldsymbol{\nabla}_{i,\alpha A}V(r_{ij,\alpha A}) + v_1(\boldsymbol{r}_{i,\alpha B}^{C}-\boldsymbol{r}_{j,\alpha B}^{C})\boldsymbol{\nabla}_{i,\alpha B}V(r_{ij,\alpha B}) + \frac{v_1}{2}(\boldsymbol{r}_{i,\alpha+1}^{C}-\boldsymbol{r}_{j,\alpha+1}^{C})\boldsymbol{\nabla}_{i,\alpha+1}V(r_{ij,\alpha+1})\Bigg)\ , \tag{2.78}$$

$$\begin{aligned} Y_{MN}^{pT} = \sum_{\alpha=1}^{M}\sum_{i=1}^{N}\sum_{\substack{j=1\\ j\neq i}}^{N}\sum_{a=1}^{d}\sum_{b=1}^{d}\Bigg(&\frac{a_1}{2}(r_{i,\alpha}^{C}-r_{j,\alpha}^{C})^{a}T(i,j,\alpha)_{a}^{b}(F_{i,\alpha})_{b} \\ &+(1-2a_1)(r_{i,\alpha A}^{C}-r_{j,\alpha A}^{C})^{a}T(i,j,\alpha A)_{a}^{b}(F_{i,\alpha A})_{b} \\ &+a_1(r_{i,\alpha B}^{C}-r_{j,\alpha B}^{C})^{a}T(i,j,\alpha B)_{a}^{b}(F_{i,\alpha B})_{b} \\ &+\frac{a_1}{2}(r_{i,\alpha+1}^{C}-r_{j,\alpha+1}^{C})^{a}T(i,j,\alpha+1)_{a}^{b}(F_{i,\alpha+1})_{b}\Bigg)\ , \end{aligned} \tag{2.79}$$

and as before, the tensor $T(i,j,\alpha)_a^b$ appears in equation 2.72 and $r_{i,\alpha}^C$ is defined by equation 2.66.

2.5.3 Pair-correlation function

The pair correlation function $g(\boldsymbol{r}_1,\boldsymbol{r}_2)$ is proportional to the probability of finding a particle in $\boldsymbol{r}_2$ while another particle is placed in $\boldsymbol{r}_1$, and can be defined as

$$g(\boldsymbol{r}_1,\boldsymbol{r}_2) = \frac{V^2}{Z}\int \rho(\boldsymbol{R},\boldsymbol{R};\beta)\mathrm{d}\boldsymbol{r}_3\ldots\mathrm{d}\boldsymbol{r}_N \tag{2.80}$$

using Feynman's density matrix formalism. For uniform systems, that is our case in this thesis, the pair correlation function depends only in the norm of the relative distance $\boldsymbol{r}=\boldsymbol{r}_2-\boldsymbol{r}_1$. This allows us to define our estimator as

$$g(\boldsymbol{r}) = \frac{V^2}{Z}\left\langle \frac{1}{M}\sum_{\alpha=1}^{M}\sum_{i=1}^{N}\sum_{\substack{j=1\\ j\neq i}}^{N}\delta\left(\boldsymbol{r}-(\boldsymbol{r}_{i,\alpha}-\boldsymbol{r}_{j,\alpha})\right)\right\rangle\ . \tag{2.81}$$

In practice, the appearance of a delta function in the estimator means we can calculate the pair correlation function by constructing an histogram of the frequencies of the relative distances between all pair of particles. Also, as the estimator has a symmetry over the imaginary time, we can take into account all the time slices M when constructing the histogram, which provides us with larger statistics. Each column of the histogram, of width $\Delta/2$, has to be nor-

malized dividing by the volume associated to the shell of radius $r - \Delta/2$ and $r + \Delta/2$.

One can notice that the estimator in equation 2.81 only works in the assumption of knowing the exact thermal density matrix. In order to obtain an estimator that holds at any imaginary time step instead of only at $\tau \to 0$, we can compute it as a functional derivative of the free energy [53]. For the primitive action, the estimator presented above works properly since the estimator of the distance between to atoms is simply the distance between its *beads* in periodic boundary conditions. However, for the Chin action the presence of the double commutator term in the expression of the potential action inserts a term that depends on the temperature in the evaluation of the distance between particles. This term may affect the construction of the histogram and should be taken into account when performing the estimation [54]. In the end, the effect of this term is shown to be really small [51] and it is an irrelevant quantity when compared to the statistical error.

2.5.4 Static structure factor

We can access the spatial order of the atoms in the reciprocal space by computing the static structure factor:

$$S(\boldsymbol{q}) = \frac{1}{NZ} \int \mathrm{d}\boldsymbol{R} \rho(\boldsymbol{R}, \boldsymbol{R}; \beta) \left(\sum_{i=1}^{N} \exp\left(-i\boldsymbol{q}\boldsymbol{r}_i\right) \right) \left(\sum_{i=1}^{N} \exp\left(i\boldsymbol{q}\boldsymbol{r}_i\right) \right) \ . \tag{2.82}$$

One can obtain this property by performing the Fourier transform of the pair-correlation function, but we can compute it directly along the PIMC simulation. We perform simulations by choosing a box with a finite size and periodic boundary conditions, which discretize the values the vector $\boldsymbol{q}$ can take. For a three dimensional box with size L_x, L_y and L_z, the vector $\boldsymbol{q}$ is then

$$\boldsymbol{q} = 2\pi \left(\frac{n_x}{L_x}, \frac{n_y}{L_y}, \frac{n_z}{L_z} \right) \ , \tag{2.83}$$

where n_x, n_y and n_z are integer numbers. As we have explained for the pair-correlation function, we take advantage on the symmetry over imaginary time to use all *bead* configurations to evaluate the static structure factor with more statistics. The static structure factor is then computed as

$$S(\boldsymbol{q}) = \frac{1}{NM} \left\langle \sum_{\alpha=1}^{M} \sum_{i=1}^{N} \sum_{\substack{j=1 \\ j \neq i}}^{N} \cos(\boldsymbol{q}\boldsymbol{r}_{i,\alpha}) \cos(\boldsymbol{q}\boldsymbol{r}_{j,\alpha}) + \sin(\boldsymbol{q}\boldsymbol{r}_{i,\alpha}) \sin(\boldsymbol{q}\boldsymbol{r}_{j,\alpha}) \right\rangle \ . \tag{2.84}$$

2.5.5 Intermediate scattering function in imaginary time

In a similar way to the static structure factor, we can compute the intermediate scattering function in imaginary time $F(\boldsymbol{q}, t)$

$$F(\boldsymbol{q}, t) = \frac{1}{NZ} \int \mathrm{d}\boldsymbol{R} \rho(\boldsymbol{R}, \boldsymbol{R}; \beta) \hat{\rho}_{\boldsymbol{q}}(\tau) \hat{\rho}_{\boldsymbol{q}}^{\dagger}(0) \ . \tag{2.85}$$

with

$$\hat{\rho}_{\boldsymbol{q}}(t) = \sum_{i=1}^{N} e^{i\boldsymbol{q}\boldsymbol{r}_i(t)} \ . \tag{2.86}$$

Our PIMC scheme works with discrete imaginary time, so the values t in which we are able to compute the intermediate scattering function will depend on the value $\tau = \beta/M$. On the other hand, the intermediate scattering function is a periodic function, so we only need to sample it up to $t = \beta/2$.

In a similar fashion to the static structure factor, we can rewrite equation 2.85 as

$$F(\boldsymbol{q}, t) = \frac{1}{NM} \Bigg\langle \sum_{\alpha=1}^{M} \sum_{i=1}^{N} \sum_{\substack{j=1 \\ j \neq i}}^{N} \cos(\boldsymbol{q}\boldsymbol{r}_{i,\alpha}(t)) \cos(\boldsymbol{q}\boldsymbol{r}_{j,\alpha}(0)) + \sin(\boldsymbol{q}\boldsymbol{r}_{i,\alpha}(t)) \sin(\boldsymbol{q}\boldsymbol{r}_{j,\alpha}(0)) \Bigg\rangle \ . \tag{2.87}$$

Also, the symmetry of these property over imaginary time allows us to use all the *beads* for a single imaginary time t calculations, as long as the time difference between the density fluctuation operators (Eq. 2.86) is t, $\left\langle \hat{\rho}_{\boldsymbol{q}}(\tau_0 + t) \hat{\rho}_{\boldsymbol{q}}^{\dagger}(\tau_0) \right\rangle$.

2.5.6 One-body density matrix

The one-body density matrix $\rho_1(\boldsymbol{r}, \boldsymbol{r}')$ is the inverse Fourier transform of the momentum distribution, and can provide insight on the Bose-Einstein condensation (BEC) properties of a quantum system.

The one-body density matrix can be written as

$$\rho_1(\boldsymbol{r}_1, \boldsymbol{r}_1') = \frac{V}{Z} \int d\boldsymbol{r}_2 \ldots d\boldsymbol{r}_M \rho(\boldsymbol{R}, \boldsymbol{R}'; \beta) \ , \tag{2.88}$$

where $\rho(\boldsymbol{R}, \boldsymbol{R}'; \beta)$ is the thermal density matrix computed for two configurations $\boldsymbol{R} = \{\boldsymbol{r}_1, \boldsymbol{r}_2 \ldots, \boldsymbol{r}_N\}$ and $\boldsymbol{R}' = \{\boldsymbol{r}_1', \boldsymbol{r}_2 \ldots, \boldsymbol{r}_N\}$ which differs for the position of only one particle.

In a strongly interacting system, a macroscopic occupation of the ground state shows a delta-peak in the momentum distribution for $\boldsymbol{q} = 0$. This is shown in the one-body density matrix as a non-zero asymptotic value in the limit of large distances $\boldsymbol{r} = \boldsymbol{r}_1 - \boldsymbol{r}_1'$. This can be related with the condensate fraction n_0 as

$$\lim_{|\boldsymbol{r}|\to\infty} \rho_1(\boldsymbol{r}, \boldsymbol{r}') = n_0 \tag{2.89}$$

Observing the equation 2.90 one can see that ρ_1 is an off-diagonal observable. In our PIMC scheme, this means that the *worm* (see Section 2.4.2) needs to be open. The one-body density matrix is then computed in the same classical mapping as the other estimators, but when the worm polymer is open.

As for equation 2.90, only the position of one atom needs to be different. Thus, we can compute the one-body density matrix with the positions of the *worm*,

$$\rho_1(\boldsymbol{r}) = \frac{V}{NZ} \left\langle \delta \left(\boldsymbol{r} - (\boldsymbol{r}_{\text{worm},1} - \boldsymbol{r}_{\text{worm},M+1}) \right) \right\rangle \ , \tag{2.90}$$

where $\boldsymbol{r}_{\text{worm},1}$ stands for the position of the *bead* which is the *tail* of the worm, and $\boldsymbol{r}_{\text{worm},M+1}$ as the *head* of the worm, taking into account that since there will be permutations the index of the polymer which contains the head and tail may not be the same.

Contrary to previous properties, we cannot take advantage from the symmetry over imaginary time, thus the calculation of this property is less efficient. A easy way to improve this efficiency is to perform various calculations of this property, proposing small movements of the head and tail of the worm whereas the worm is open.

2.5.7 Superfluid density

One can think of the superfluid density of a quantum liquid as the fraction of the system that does not respond to movements of the walls of its vessel. It can be defined as

$$I = \frac{\mathrm{d}^2 F}{\mathrm{d}\omega^2}|_{\omega=0} = \frac{\mathrm{d}\langle \hat{L}_z \rangle}{\mathrm{d}\omega}|_{\omega=0} \ , \tag{2.91}$$

where I is the momentum of inertia, F the free energy and $\hat{L}_z$ the total angular momentum operator in the rotation axis.

By defining the classical momentum of inertia

$$I_c = \left\langle \sum_{i=1}^{N} m_i (r_i^*)^2 \right\rangle \ , \tag{2.92}$$

with r_i^* being the distance of the i-th atom from the rotation axis, one can write the superfluid density as

$$\frac{\rho_s}{\rho} = 1 - \frac{I}{I_c} \ , \tag{2.93}$$

i.e., it is the fraction of the system which does not respond classically to the rotation.

The attainment of an estimator for ρ_s/ρ for the PIMC scheme is not trivial, since equation 2.93 considers a rotation. Switching the reference frame to the rotating bucket, Pollock and Ceperley proposed a path integral expression for the effective momentum of inertia [55] that yields

$$\frac{\rho_s}{\rho} = \frac{2m\langle A_z^2 \rangle}{\beta\lambda I_c} \ , \tag{2.94}$$

where A_z is the component along the z-axis of the projected area

$$\boldsymbol{A} = \frac{1}{2}\sum_{i=1}^{N}\sum_{\alpha=1}^{M} \boldsymbol{r}_{i,\alpha} \times \boldsymbol{r}_{i,\alpha+1} \ . \tag{2.95}$$

The previous estimator works in cylindrical geometry, but is more common to have periodic boundary conditions (PBC) in a PIMC simulation. In this sense, we define the winding number W as the flux of paths winding through the PBC,

$$\boldsymbol{W} = \sum_{i=1}^{N}\sum_{\alpha=1}^{M} \boldsymbol{r}_{i,\alpha+1} - \boldsymbol{r}_{i,\alpha} \ . \tag{2.96}$$

With this term, the estimator of the superfluid fraction is

$$\frac{\rho_s}{\rho} = \frac{\langle W^2 \rangle}{\beta\lambda I_c} \ , \tag{2.97}$$

that needs to be averaged over all the closed polymer configurations in our PIMC simulation.

2.6 Path Integral Ground State method (PIGS)

As commented at the beginning of this section, the path integral formalism can be extended to the ground state in what is known as the Path Integral Ground State method. The ground state average of an observable of a quantum system,

$$\langle \Psi_0 | \hat{O} | \Psi_0 \rangle = \frac{\int \mathrm{d}\boldsymbol{R} O(\boldsymbol{R}) \Psi_0^2(\boldsymbol{R})}{\int \mathrm{d}\boldsymbol{R} \Psi_0^2(\boldsymbol{R})} \ , \tag{2.98}$$

can be calculated by sampling the coordinates of a quantum system according to the probability distribution $\Psi_0^2/\int \mathrm{d}\boldsymbol{R}\Psi_0^2(\boldsymbol{R})$. As generally the exact ground state wave function is unknown, we can approximate $\Psi_0(\boldsymbol{R})$ with a *trial wave function* $\Psi_T(\boldsymbol{R})$.

It is important that the trial wave function has the correct symmetry under particle permutations: It must be symmetric for bosons and antisymmetric for fermions. From the variational principle of quantum mechanics, $E(\Psi) = \langle\Psi|\hat{H}|\Psi\rangle \geq E_0$, with E_0 being the ground-state energy of the system. Thus, a good approximation Ψ_T for Ψ_0 will lower the value of

$$E_T = \frac{\int \mathrm{d}\boldsymbol{R}E_L(\boldsymbol{R})\Psi_T^2(\boldsymbol{R})}{\int \mathrm{d}\boldsymbol{R}\Psi_T^2(\boldsymbol{R})} \tag{2.99}$$

where the *local energy* E_L is defined as

$$E_L = \frac{\hat{H}\Psi_T(\boldsymbol{R})}{\Psi_T(\boldsymbol{R})} \ . \tag{2.100}$$

The *Variational Monte Carlo* method uses this scheme to construct a trial wave function with some free parameters, and then optimize them by minimizing E_T. However, E_T is an upper bound of the energy, thus it is desirable to make some improvements in this method.

For this end, we introduce the Schrödinger equation in imaginary time $\tau = it$,

$$-\frac{\partial}{\partial\tau}\Psi(\boldsymbol{R};\tau) = \hat{H}\Psi(\boldsymbol{R};\tau) \ , \tag{2.101}$$

where we can use the presented trial wave function as a description at $\tau = 0$, $\Psi(\boldsymbol{R},\tau=0) = \Psi_T(\boldsymbol{R})$. The solution for the wave function is then

$$\Psi(\boldsymbol{R},\tau) = e^{-\tau\hat{H}}\Psi_T(\boldsymbol{R}) = \sum_{n=0}^{\infty}\langle\Psi_n|\Psi_T\rangle\Psi_n(\boldsymbol{R})e^{-\tau E_n} \ , \tag{2.102}$$

where E_n is the eigenstate of Ψ_n. For large enough τ we can write

$$\Psi_0(\boldsymbol{R}) = \lim_{\tau\to\infty}\Psi(\boldsymbol{R};\tau) = \lim_{\tau\to\infty}\int \mathrm{d}\boldsymbol{R}'G(\boldsymbol{R},\boldsymbol{R}';\tau)\Psi_T(\boldsymbol{R}') \ , \tag{2.103}$$

with $G(\boldsymbol{R},\boldsymbol{R}';\tau) = \langle\boldsymbol{R}|e^{-\tau\hat{H}}|\boldsymbol{R}'\rangle$ being the imaginary time propagator, which is equivalent to a thermal density matrix for a quantum system at temperature $T = 1/(k_B\tau)$. This allows us to write an accurate approximation for the ground state wave function by means of the Path Integral formalism previously used at finite temperature in what is known as the *Path Integral Ground State* scheme.

Using the convolution property (Eq. 2.7) we obtain

$$\Psi_{\text{PIGS}}(\boldsymbol{R}_M) = \int \sum_{\alpha=0}^{M-1} \mathrm{d}\boldsymbol{R}_\alpha G(\boldsymbol{R}_{\alpha+1}, \boldsymbol{R}_\alpha; \tau)\Psi_T(\boldsymbol{R}_0) \ . \tag{2.104}$$

The main advantage of PIGS in front of other methods such as VMC is that we can control the systematic error by means of the number of time slices M. By increasing this value, we provide a better approximation for Ψ_0 until the estimated energy E_T will become independent of M, indicating that the systematic error that arises from the choice of Ψ_T has been lowered below statistical uncertainties, in a way similar to what happens for PIMC. This is way PIGS method is regarded as an *exact* method, as with PIMC.

With the basis of the method explained, all the relevant observables can be calculated as shown in equation 2.98,

$$\langle\Psi_0|\hat{O}|\Psi_0\rangle = \frac{\int \prod_{\alpha=1}^{2M} \mathrm{d}\boldsymbol{R}_\alpha O(\boldsymbol{R}_M)\Psi_T(\boldsymbol{R}_{2M})G(\boldsymbol{R}_\alpha, \boldsymbol{R}_{\alpha-1}; \tau)\Psi_T(\boldsymbol{R}_0)}{\int \prod_{\alpha=1}^{2M} \mathrm{d}\boldsymbol{R}_\alpha \Psi_T(\boldsymbol{R}_{2M})G(\boldsymbol{R}_\alpha, \boldsymbol{R}_{\alpha-1}; \tau)\Psi_T(\boldsymbol{R}_0)} \ . \tag{2.105}$$

As for the probability distribution to be sampled via Monte Carlo procedure,

$$p(\boldsymbol{R}_0 \ldots \boldsymbol{R}_{2M}) = \frac{\prod_{\alpha=1}^{2M} \Psi_T(\boldsymbol{R}_{2M})G(\boldsymbol{R}_\alpha, \boldsymbol{R}_{\alpha-1}; \tau)\Psi_T(\boldsymbol{R}_0)}{\int \prod_{\alpha=1}^{2M} \mathrm{d}\boldsymbol{R}_\alpha \Psi_T(\boldsymbol{R}_{2M})G(\boldsymbol{R}_\alpha, \boldsymbol{R}_{\alpha-1}; \tau)\Psi_T(\boldsymbol{R}_0)} \ , \tag{2.106}$$

can be interpreted as a classical system of interacting polymers, similarly to PIMC analogy, but each with $2M+1$ *beads*. Thus, the same mapping we applied to the PIMC method can be used with the Path Integral Ground State. The main difference is that we do not need to impose periodic boundary conditions in imaginary time in the trace of the propagator, so the the classical isomorphism will not be polymer rings but open polymers. Also, the parameter τ is related to the temperature in the PIMC method while it does not have a physical meaning for PIGS and must be considered only as a variational parameter.

In the end, our PIGS chains impose the trial wave function Ψ_T in its extremities, while propagating it along a high enough number of *beads* towards the center of chain provides a better approximation of Ψ_0 near its center. In this sense, the estimation of observables (Eq. 2.105) is only exact in the center point of the chain.

Chapter 3

Phase diagram of a one-dimensional Coulomb gas

In this chapter, we present the quantum phase diagram of a one-dimensional Coulomb wire obtained using the PIMC method. The exact knowledge of the nodal points of this system permits us to find the energy in an exact way, solving the sign problem which spoils fermionic calculations at higher dimensions. The results obtained allow for the determination of the stability domain, in terms of density and temperature, of the one-dimensional Wigner crystal. At low temperatures, the quantum wire reaches the quantum-degenerate regime, which is also described by the diffusion Monte Carlo method. By increasing the temperature the system transforms to a classical Boltzmann gas, which we simulate using classical Monte Carlo. At large enough density, we identify a one-dimensional ideal Fermi gas which remains quantum up to higher temperatures than in two- and three-dimensional electron gases. The obtained phase diagram as well as the energetic and structural properties of this system are relevant to experiments with electrons in quantum wires and to Coulomb ions in one-dimensional confinement.

3.1 Introduction

Few systems are more universal than electron gases. Their study started long-time ago and the compilation of knowledge that we have now at hand is very wide, with impressive quantitative and qualitative results [56]. Phase diagrams for the electron gas in two and three dimensions appear now quite well understood thanks to progressively more accurate many-body calculations using mainly quantum Monte Carlo methods [57]. However, the theoretical knowl-

edge of the electron gas in the one-dimensional (1D) geometry is more scarce and a full determination of the density-temperature phase diagram is still lacking. The present results are intended as a contribution towards filling this gap by means of a microscopic approach based on the path integral Monte Carlo (PIMC) method.

The quasiparticle concept introduced by Landau in his Fermi liquid theory is able to account for the excitations of the electron gas in two and three dimensions. This is not the case in one dimension where the enhancement of correlations makes all excitations, even at low energy, to be collective. The appropriate theoretical framework is an effective low-energy Tomonaga-Luttinger (TL) theory [58–60], properly modified by Schulz [61] to account for the long-range nature of the Coulomb interaction. Probably, the most noticeable prediction of the TL theory is the separation between spin and charge degrees of freedom, whose excitations are predicted to travel at different velocities. At the same time, a Coulomb wire is fundamentally different from other TL systems in that at low densities it forms a Wigner crystal, as manifested by the emergence of quasi-Bragg peaks [61]. Also the strongly repulsive nature of interactions might lead to a formation of a Coulomb Tonks-Girardeau gas[62, 63]. In spite of the experimental difficulties in getting real 1D environments, strong evidences of having reached the TL liquid and the 1D Wigner crystal have been reported in the last years [64–72]. Therefore, the continued theoretical interest on this 1D system is completely justified and can help to understand future experimental findings.

3.2 Quantum Monte Carlo methods for fermionic systems

The ground-state properties of the 1D Coulomb gas have been studied in the past using several methods, the most accurate results being obtained using the diffusion Monte Carlo (DMC) method [73–76]. One of the main goals of these calculations was the estimation of the interaction energy of the gas with as higher precision as possible to generate accurate density functionals to be used within density functional theory of quasi-one-dimensional systems. All these calculations have been carried out assuming a quasi-1D geometry imposed by a tight transverse confinement, normally of harmonic type. In the latter case, one assumes that electrons occupy the ground-state of the transverse harmonic potential and so in the resulting effective Coulomb interaction the divergence

at $x = 0$ is eliminated. Proceeding in this way, the effective one-dimensional interatomic potential can be Fourier transformed. However, a recent DMC calculation [77] has shown that the use of the bare Coulomb interaction is not a problem for the estimation of the energy and structural properties because the wave function becomes zero when $|x| \to 0$. More importantly, the presence of a node at $x = 0$ makes Girardeau's mapping applicable [78] which means that the many-particle bosonic wave function is the absolute value of the fermionic one, with the same Hamiltonian. In other words, the non-integrable divergence of the interaction at small distances acts effectively as a Pauli principle for bosons. From the computational point of view, this is highly relevant because knowing the exact position of the nodes allows us to perform an exact simulation without the usual upper-bound restriction imposed by the fixed-node approximation when the nodal surfaces are unknown.

For our calculations at finite temperature, we consider a system composed of N particles with charge e and mass m in a 1D box of length L with periodic boundary conditions, that interact by means of a pure Coulomb potential. We work in atomic units, the Bohr radius $a_0 = \hbar^2/(me^2)$ for the length and the Hartree $\mathrm{Ha} = e^2/a_0$ for the energy. In these reduced units, the Hamiltonian is given by

$$H = -\frac{1}{2}\sum_{i=1}^{N}\frac{\partial^2}{\partial x_i^2} + \sum_{i<j}^{N}\frac{1}{|x_i - x_j|}\ . \tag{3.1}$$

With this knowledge we can estimate the properties of the system using a PIMC scheme (see section 2.2) by means of the Chin action (see section 2.3.1). The number of beads M is adjusted for any temperature and density to ensure unbiased results; it is rather large at the lowest temperatures and high densities, $M = 500$, and it becomes smaller when the temperature increases and the density is low, $M = 20$. The fourth-order dependence of the energy on $1/M$ is recovered at larger M values than in ^{4}He due to the pathological behavior of the Coulomb potential for the lowest approximation for the action (primitive approximation) [33]. Nevertheless, the high-order PIMC method is able to explore the major part of the density-temperature phase diagram with accuracy and without any bias coming from the fixed-node constraint.

Our main goal is the calculation of the phase diagram of the 1D Coulomb quantum wire. To this end, we mainly determine the energetic and structure properties of this system. For the energy we use the virial estimator from section 2.5.1, which relies on the invariance of the partition function under a scaling of the coordinate variables, thus providing good results at large values of M, where the thermodynamic estimator fails to provide converged results [34]. The

structure properties of the system are obtained from the behavior of the static structure factor (see section 2.5.4).

3.3 Energy per particle at finite temperature

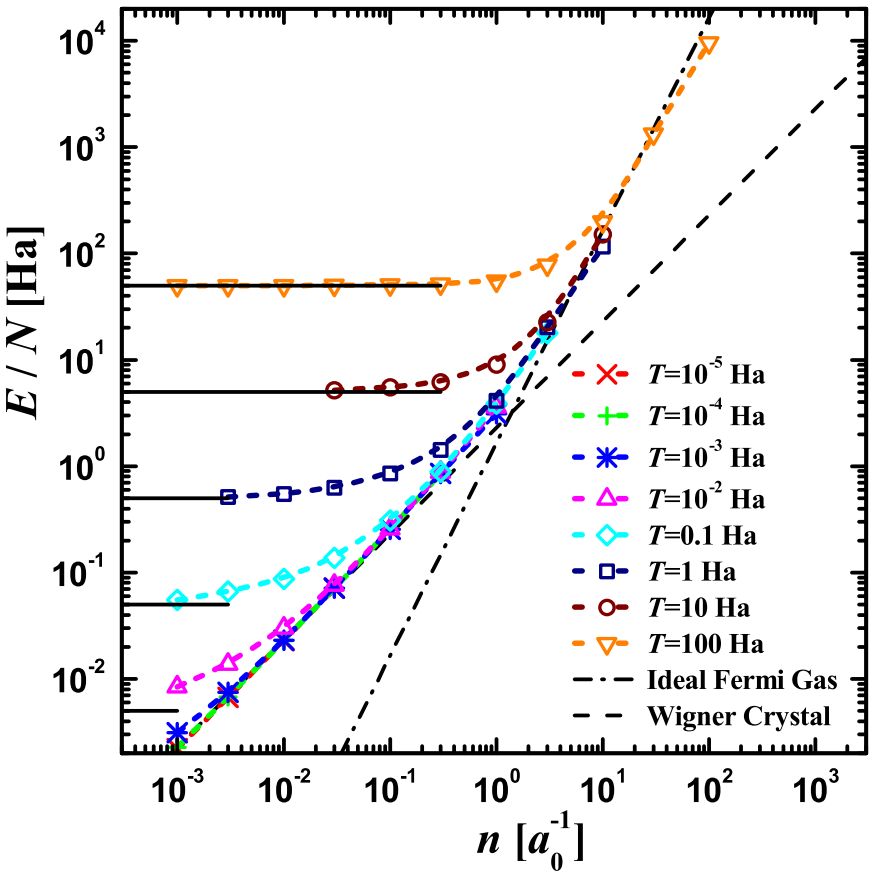

Fig. 3.1 Energy per particle as a function of the density for $N = 10$. Symbols, PIMC results at different temperatures; dashed line, energy of a Wigner crystal at $T = 0$; dash-dotted line, IFG energy at $T = 0$. Solid lines, classical limit $E/N = T/2$.

The energies obtained at different temperatures and densities are shown in Fig. 3.1. When both the temperature and density are low, the potential energy dominates and the total energy can be estimated by summing up all pair Coulomb potential energies for a set of particles at the fixed positions of a Wigner crystal. For a given number of particles N, the leading term in the energy is linear with the density n [79],

$$\frac{E_{\mathrm{W}}}{N} = e^2 n \ln N \ . \tag{3.2}$$

If one fixes the density and changes the number of particles, Eq. (3.2) predicts an energy per particle which diverges logarithmically with N. This is, in fact, a well known effect of the long-range behavior of the Coulomb potential in strictly 1D problems [77]. When the density increases, the kinetic energy increases faster than the potential energy due to its quadratic dependence with n. Then, the system reaches a regime where the energy is well approximated by the ground-state energy of an ideal Fermi gas (IFG),

$$\frac{E_{\,\mathrm{IFG}}}{N} = \frac{\hbar^2 k_F^2}{6m} \,, \tag{3.3}$$

with $k_F = \pi n$ being the 1D one-component Fermi momentum. Both limiting behaviors, E_{W}/N (Eq. 3.2) and $E_{\,\mathrm{IFG}}/N$ (Eq. 3.3) are shown as straight lines which cross at $n \simeq 1$ in the log-log plot of Fig. 3.1. The ground-state energy obtained with the DMC method for $T = 0$ is recovered in our PIMC simulation when the temperature drops below some critical temperature, which value depends on the density. Increasing the density in the ground state, the system evolves from a Wigner crystal to a zero-temperature ideal Fermi gas [77]. For a fixed finite temperature, $T \lesssim 1$ Ha, the dilute regime of low density corresponds to a classical gas with the energy per particle given by the classical value $E_{\mathrm{C}} = T/2$ (solid horizontal lines) , the Wigner crystal is realized at larger densities and, finally, the quantum wire behaves as an ideal Fermi gas for $n \gtrsim 1$. For temperatures $T \gtrsim 1$ Ha, the Wigner crystal behavior is no more observed and the system evolves directly from a classical gas to a Fermi one.

3.4 Properties of Quantum Wigner crystal

In order to get an insight on the properties of a quantum Wigner crystal it is important to derive the equation of states as a perturbative series in terms of powers of na_0. The leading term is provided by the potential energy of a classical crystal and is pathologic in the sense that it diverges in the thermodynamical limit. On the other hand this divergency is caused by the long-range part of the Coulomb energy and effectively does not change the short-range physics which is important, for example, for understanding the applicability of the bare Coulomb potential to quantum wires of a finite width. Thus, it is of importance to derive the subleading term in the equation of state, which will behave properly in the thermodynamic limit and will be relevant for the short-range physics. This is done by means of the harmonic crystal theory.

The leading term $E^{(0)}$ in the equation of state of a Wigner crystal, $na_0 \to 0$, is given by the potential energy of a crystal with perfect packing, $E^{(0)} = 1/2 \sum_{i\neq j}^{N} e^2 n/|i-j|$. For N electrons in a box with periodic boundary conditions the Wigner crystal energy is

$$\frac{E^{(0)}}{N} = (na_0)\ \mathrm{Ha} \times \begin{cases} \mathrm{H}_{\frac{N}{2}-1} + \frac{1}{N}, & \text{for even } N \\ \mathrm{H}_{\frac{N-1}{2}}, & \text{for odd } N \end{cases} \tag{3.4}$$

where $\mathrm{H}_n = \sum_{i=1}^{n} \frac{1}{i}$ is the n-th harmonic number. That is, the leading term grows linearly with the density na_0 and it suffers from a logarithmic divergency. caused long-range Coulomb interaction, $E^{(0)}/N = \mathrm{Ha}(na_0)\ln(\gamma' N/2) + O(N^{-2})$ where $\gamma' = 1.781$ is the Euler's constant.

In the physical description of the subleading term, the electrons oscillate close to the minima in the potential energy, generating excitations $\omega(k)$ with plasmonic dispersion relation, as can be obtained from the harmonic theory [77, 80, 81]

$$\left[\frac{\hbar\omega(k)}{\mathrm{Ha}/2}\right]^2 = (na_0)^3[4\zeta(3) - 2\mathrm{Li}_3(e^{\frac{ik}{n}}) - 2\mathrm{Li}_3(e^{-\frac{ik}{n}})]\ , \tag{3.5}$$

where $\mathrm{Li}_n(z) = \sum_{k=1}^{\infty} z^k/k^n$ is the polylogarithm function.

The quantum correction to the energy of a Wigner crystal (3.4) comes from the zero-point motion of plasmons in the first Brillouin zone (BZ) [82, 83]

$$\frac{E^{(1)}}{N} = \int_{\mathrm{BZ}} \frac{\hbar\omega(k)}{2}\ \frac{dk}{V_{\mathrm{BZ}}}\ , \tag{3.6}$$

where $V_{\mathrm{BZ}} = 2k_{\mathrm{BZ}} = 2\pi n$ is the volume of the first Brilloin zone. Finally, we obtain the subleading term in the form of

$$\frac{E^{(1)}}{N} = C(na_0)^{3/2}\mathrm{Ha} \tag{3.7}$$

with the constant equal to

$$C = \int_0^{\pi} \frac{1}{2}\sqrt{4\zeta(3) - 2Li_3(e^{ix}) - 2Li_3(e^{-ix})}\ \frac{dx}{\pi} = 0.50\ .$$

In particular this means that the kinetic energy scales as $(na_0)^{3/2}$ with the density.

3.5 Static structure factor

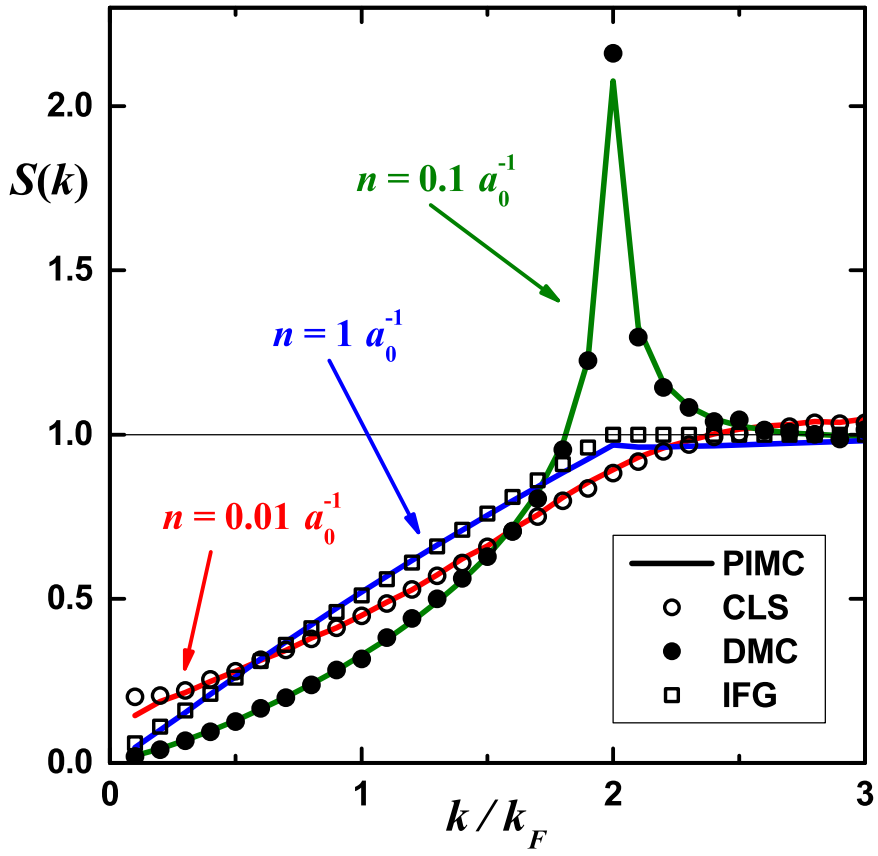

Fig. 3.2 Static structure factor for $N = 20$ and $T = 10^{-2}$ Ha for different densities. At the lowest density, we compare the PIMC result with a classical Monte Carlo simulation (CLS). For densities $n \geq 0.1\, a_0^{-1}$, we make a comparison with the ground-state properties obtained by the DMC method ($T = 0$). For densities $n \geq 1\, a_0^{-1}$, we compare the PIMC results with the Ideal Fermi Gas.

In spite of the absence of real phase transitions in this 1D system one can identify different regimes with well-known limiting cases. As we have shown in Fig. 3.1, the energy shows a rich variety of behaviors as both the density and temperature are changed. However, it is the study of the structural properties which provides us a deeper understanding on the difference between regimes. To this end, we use the PIMC method to calculate the density and temperature dependence of the static structure factor $S(k)$. Its behavior at a constant temperature ($T = 10^{-2}$ Ha) and different densities is shown in Fig. 3.2. At the lowest density $n = 0.01\, a_0^{-1}$, the quantum PIMC results are nearly indistinguishable of the classical $S(k)$ obtained by the classical Monte Carlo method (Boltzmann distribution) at the same density and temperature. Increasing more

the density, the static structure factor shows clearly the emergence of a Bragg peak at $k/k_F = 2$ signaling the formation of a Wigner crystal in 1D [61]. At low temperatures, the quantum degeneracy is reached and $S(k)$ agrees with that of a DMC estimation at $T = 0$ at the same density. Similarly to what happens at zero temperature [77], increasing even more the density the system evolves to an ideal Fermi gas. In Fig. 3.2, we also compare the PIMC result for $S(k)$ at $n = 1\, a_0^{-1}$ with the IFG $S(k)$ at the same density and $T = 0$: the agreement between both curves is excellent.

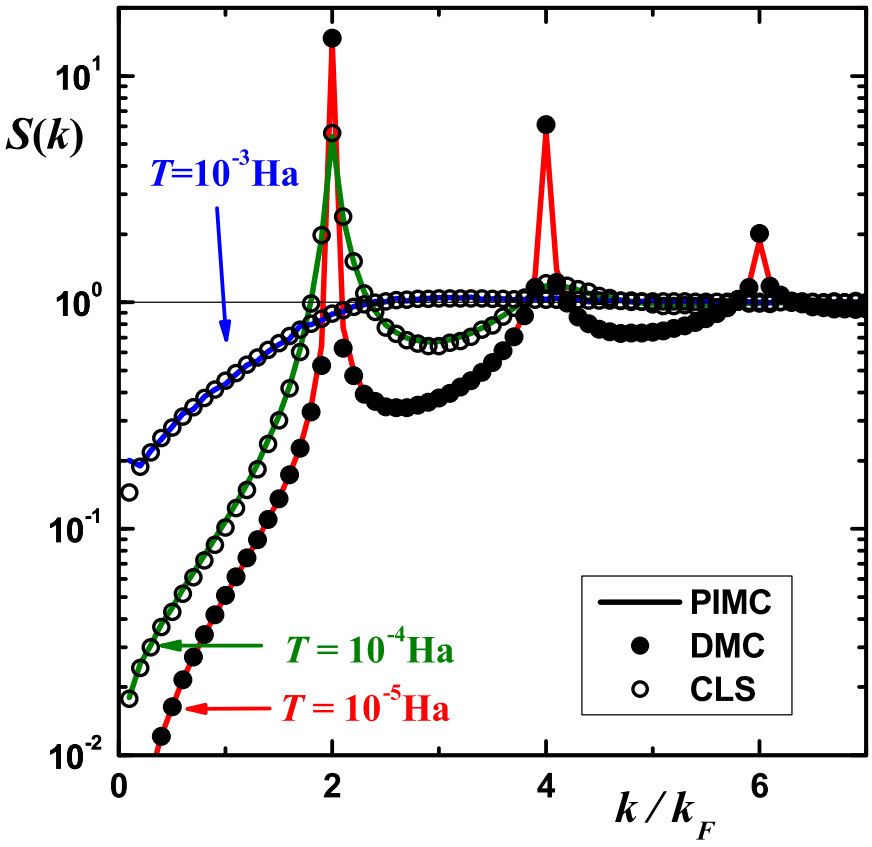

Fig. 3.3 A semilogarithmic plot of the static structure factor for $N = 20$ and $n = 10^{-3}$ for different temperatures. At the lowest temperature we compare the PIMC result with the DMC result of $T = 0$. At high temperature, we compare the PIMC result with a classical Monte Carlo simulation (CLS).

It is important to understand how the temperature affects the structural properties, when the density is fixed and the temperature is progressively increased. Figure 3.3 reports PIMC results obtained at low density, $n = 10^{-3}\, a_0^{-1}$. At low temperatures, one identifies the characteristic Bragg peaks at $k/k_F = 2l$ with integer l. At the lowest considered temperature, $T = 10^{-5}$ Ha, we observe a quantum crystal and $S(k)$ is in nice agreement with the $T = 0$ result obtained by

the DMC method. Increasing the temperature by a factor of ten, the presence of Bragg peaks confirms the formation of a Wigner crystal while its structure is very different from the quantum one, observed at $T = 0$. Importantly, we find out that the correlations at $T = 10^{-4}$ Ha are the same as in a crystal with electrons obeying Boltzmann statistics.

Once in the classical regime, by increasing the temperature the crystal *melts* and becomes a gas. In Fig. 3.3, one can observe that PIMC and classical simulations predict the same $S(k)$ in a gas at temperature $T = 10^{-3}$ Ha. It becomes clear from Figs. 3.2 and 3.3 that the transition between different regimes can be induced by changing the density or the temperature.

3.6 Phase diagram

From the PIMC results for both energy and structure we establish the temperature-density *phase* diagram of the 1D Coulomb wire. The phase diagram is reported in Fig. 3.4 and constitutes the main result of this chapter. We identify three different regimes: classical Coulomb gas, Wigner crystal and ideal Fermi gas, where the last two regimes show a crossover from quantum to classical behavior. The Wigner crystal is identified by calculating the ratio of the peak's height of $S(k)$ at $k/k_F = 2$ for two values of the number of particles ($N = 20$, 10). When the height of the peak increases with N, the system behaves as a Wigner crystal. In Fig. 3.4, we use a contour plot to show that ratio in a grey scale, where black color stands for large ratio and white for ratio equal to one. In the T-n plane, the Wigner crystal phase shows a triangular shape, with the strongest signal localized in the vertex of lowest density and temperature, delimited by transitions to a Coulomb or an ideal Fermi gas. This quantum Wigner crystal is well described by the zero-temperature theory, as we have shown in Figs. 3.2 and 3.3. Increasing the temperature, one can see how the quantum crystal transforms into a classical Wigner lattice. In both regimes, particles move around the lattice points but these fluctuations are of quantum and thermal nature in quantum and classic crystals, respectively. Starting from a high-temperature crystal and by decreasing the temperature we see that the system becomes more ordered and the height of the peaks increases. Indeed, at zero temperature the classical system would always form a perfect crystal with no fluctuations. Instead, we see that the height of the peaks stops growing when we decrease the temperature down to the quantum-degeneracy regime. By lowering the temperature further the system remains in the ground state. In fact, the classical crystal regime is realized when the temperature is large compared to the height of the first

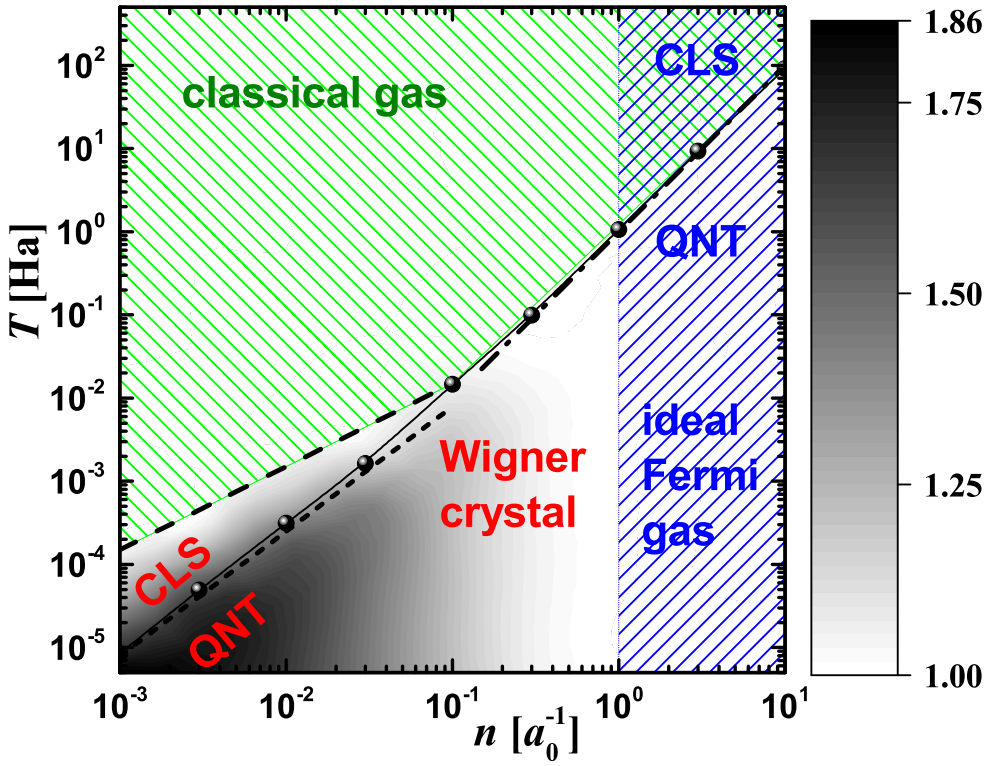

Fig. 3.4 Temperature – density *phase* diagram. Long-dashed line, gas-Wigner crystal crossover; dash-dotted line, locates the crossover between a quantum Fermi gas and a classical thermal gas ($T_F \propto n^2$); short-dashed line separates the classical (CLS) and quantum (QNT) regimes within the Wigner crystal, $T \propto n^{3/2}$; symbols connected with a thin line (guide to an eye), position of the classical-quantum crossover estimated as $E_{\rm kin} = T$. Ideal Fermi gas and Wigner crystal regimes for the considered number of particles are separated by $n \approx 1$. Within the Wigner phase, the ratio of the peak value in $S(k)$ for $N = 20$ and $N = 10$ is shown with a contour plot (white color, no difference; black, large difference).

Brillouin zone ($E_{\rm BZ}$), $E_{\rm BZ} \ll T$. That can be estimated from the phonon spectrum (Eq. 3.5) at the border of the Brillouin zone, $E_{\rm BZ} = E_{\rm ph}(k_{\rm BZ}) \approx \hbar c|k_{\rm BZ}|$, with $k_{\rm BZ} = k_F = \pi n$. The speed of sound c is related to the chemical potential through the compressibility relation $mc^2 = n\partial\mu/\partial N$. As μ in the Wigner crystal is linear in n, one can locate the transition from the quantum to the classical Wigner crystal as $T \sim n^{3/2}$ (short-dashed line in Fig. 3.4). When the temperature is high enough, thermal fluctuations become large compared to the potential energy of the Coulomb crystal and thus the Wigner crystal melts to a classical Coulomb gas. As the energy of the Wigner crystal is linear with the density (for a fixed number of particles N) (Eq. 3.2) this *melting* transition line follows approximately the law $T \sim n$ (dashed line in Fig. 3.4).

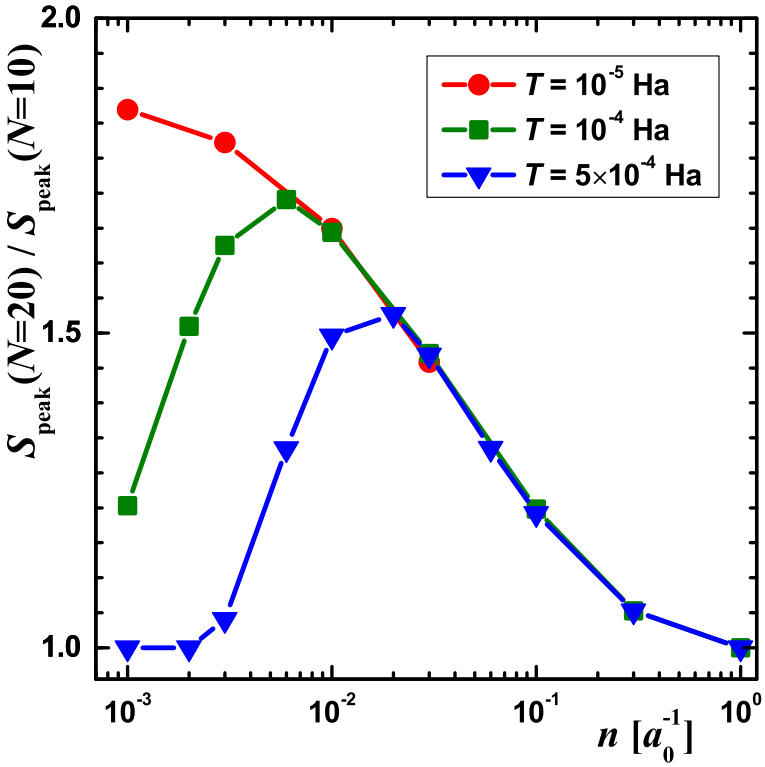

Fig. 3.5 (Color online) Ratio of main peak height of $S(k)$ at $N = 10$ and 20 as a function of the density and for three different temperatures. At the lowest T, the behavior is monotonously decreasing, from a Wigner crystal to a Fermi gas. At the two higher temperatures, a double crossing gas-crystal-gas is observed.

By changing the density while keeping the temperature fixed to a very low value, the system evolves from a Wigner crystal towards an ideal Fermi gas. This evolution is driven by the different dependence of the potential and kinetic energies on the density. The kinetic energy grows quadratically, $E_{kin}/N \propto n^2$, instead of the linear dependence of the potential energy, $E_W \propto n \ln N$. At $n \approx 1$, we observe this transition both in energy and in the shape of the static structure factor $S(k)$. For temperatures smaller than $T \lesssim 10^{-2}$ Ha, we observe two different transitions: at low densities an evolution from a thermal classical gas to a Wigner crystal, and at $n \approx 1$ the *melting* of the crystal towards the Fermi gas. This is clearly shown in Fig. 3.5, where we plot the ratio of peak heights at three different temperatures and as a function of the density. When $T > 10^{-2}$ Ha, the Wigner crystal is no more stable and the evolution with the density is from a classical gas to an IFG for densities $n > 1$. On the other hand, the finite-size dependence is very weak as it can be appreciated from the logarithmic dependence of the Wigner crystal energy on N, (Eq. 3.2). Still, it becomes important when the number of electrons is large. It is expected that the

stability region of the Wigner crystal will increase with N both in density [77] and in temperature.

The transition from the zero-temperature ideal Fermi gas to a classical gas is governed by a single parameter, namely the ratio of the temperature and the Fermi temperature, $T/T_F = T/[\pi^2 n^2/2m]$. When this ratio is much smaller than one, the system stays in the ground-state of a quantum degenerate gas. When this ratio is much larger than one, the energy approaches that of a Boltzmann classical gas. In between, the system properties are that of a finite-temperature quantum ideal Fermi gas. A special feature of the one-dimensional world is that the stability of the quantum degenerate regime is greatly increased. Indeed, the stability regime grows rapidly as the density is increased since $T/T_F \propto n^2$. This should be contrasted with $T/T_F \propto n$ in two dimensions and even weaker $n^{2/3}$ dependence in three dimensions.

In a quantum wire of a finite width b, the effective one-dimensional interaction still has a Coulomb long-range tail while the short-range part is no longer divergent and is limited by the width of the wire, $V_{\max} \propto e^2/b$ [73, 74]. The strictly one-dimensional model (Eq. 3.1) still remains applicable if the kinetic energy is small compared to the maximum of the interaction potential $V_{\max}$. The system properties are the same if the temperature is not too high and the density is not too large. Specifically, the restriction on the temperature is $k_B T \ll e^2/b$. In a Wigner crystal, the kinetic energy is proportional to the energy of the zero-point motion of plasmons $E^{\text{plasmon}} = C(na)^{3/2}$ (Eq. 3.7), posing the restriction on the density, $na_0 \ll (a_0/b)^{2/3}$. In an ideal Fermi gas, the Fermi energy E_F should be small compared to $V_{\max}$, leading to $n \ll 1/\sqrt{a_0 b}$. In typical experiments with semiconductor quantum wires the thickness is $b/a_0 = (0.1 - 1)$, so that the major part of the phase diagram presented in Fig. 3.1 remains valid. The situation is even better for experiments with carbon nanotubes placed on SrTiO3 substrates[84], for which values of $b/a_0 = 0.0001$ can be reached.

Experimental results to compare with are mainly located in the Wigner crystal domain. This phase has been observed at the following points: $T = 10^-9$Ha , $n = 3.5 \cdot 10^{-8}\ a_0^{-1}$; [64] $T = 10^{-6}$ Ha, $n = 0.001\ a_0^{-1}$ [65]; $T = 5 \cdot 10^{-6}$ Ha, $n = 0.002\ a_0^{-1}$ [68]; and $T = 10^{-5}$ Ha, $n = 0.001\ a_0^{-1}$ [69]. Only the latter one fits inside our studied regime and agrees with the prediction of a crystal; the other are deeper inside the Wigner crystal phase and presumably will be in agreement with theory.

3.7 Summary

Summarizing, in this chapter we have carried out a complete PIMC study of the density-temperature phase diagram of a 1D quantum Coulomb wire. The singularity of the Coulomb interaction at $x = 0$ allows us to solve the sign problem and makes it possible to carry out an exact calculation of the electron gas problem since we know a priori the exact position of the Fermi nodes. This is clearly a special feature of the 1D environment which cannot be translated to higher dimensions. There, in 2D and 3D, one can only access to approximate solutions to the many-body problem which worsen when the the temperature is not zero. Focusing our analysis on energetic and structural properties we have been able to characterize the different regimes of the electron wire. In spite of the lack of real phase transitions due to the strictly 1D character of the system, we have been able to define different physical regimes, including the Wigner crystal (classical and quantum), the classical Coulomb gas, and the universal ideal Fermi gas. Two relevant features make this phase diagram specially interesting: the large stability domain of the ideal Fermi gas and the double crossing gas-crystal-gas with increasing density within a quite wide temperature window. Our results are relevant to current and future experiments with electrons in a quantum wire and to Coulomb ions in one-dimensional confinement.

Chapter 4

Luttinger parameter of quasi-one-dimensional para-H_2

In this chapter, we present the results of the ground-state properties of para-hydrogen in one dimension and in quasi-one-dimensional configurations using the path integral ground state Monte Carlo method. This method produces zero-temperature exact results for a given interaction and geometry. The quasi-one-dimensional setup has been implemented in two forms: the inner channel inside a carbon nanotube preplated with H_2 and a harmonic confinement of variable strength. Our main result is the dependence of the Luttinger parameter on the density within the stable regime. Going from one dimension to quasi-one dimension, keeping the linear density constant, produces a systematic increase of the Luttinger parameter. This increase is however not enough to reach the superfluid regime and the system always remain in the quasi-crystal regime, according to Luttinger liquid theory.

4.1 Introduction

The search for a superfluid phase in molecular *para*-hydrogen (p-H_2) started from the theoretical proposal by Ginzburg and Sobyanin in 1972 [4]. They suggested that p-H_2, with spin 1, should be superfluid under a transition temperature T_λ that they estimated to be $T_\lambda \sim 6$ K using ideal Bose gas theory. This relatively high temperature, compared with the well-known transition temperature in ^{4}He ($T_\lambda(^4\text{He}) = 2.17$ K), was the result of the smaller mass of p-H_2. However, this estimation is too crude because the strong interactions between the p-H_2 molecules are simply ignored. Moreover, the transition temperature for the ideal Bose gas increases with the density ρ as $\rho^{2/3}$ whereas it is known that

in superfluid ^{4}He it slightly decreases with ρ. Later on, Apenko [85] proposed a phenomenological theory similar to the Lindemann criterion for classical crystal melting. He concluded that in p-H_2 T_λ should vary between 1.1 and 1.2 K, depending on the density. A recent PIMC simulation of p-H_2 at low temperatures, in which it was possible to frustrate the formation of the stable crystal, showed that superfluidity appears at temperatures around 1 K [86].

Superfluidity in bulk hydrogen is not observed because it crystallizes in an hcp phase at a temperature $T = 13.8$ K which is much higher than the estimated transition temperature T_λ. The mean reason is that the intermolecular interaction is around three times more attractive and the one between He atoms. This enhanced attraction dominates over the positive effect produced by the smaller mass of H_2 respect to the ^{4}He one. There have been a number of supercooling attempts to create a metastable liquid phase but even at $T \sim 9$ K the liquid phase freezes quickly into a crystal [87]. One of the a priori more interesting options was to confine hydrogen in a porous media, like a vykor glass, with pores in the nanometer scale. However, the lowest temperature at which the system was detected to be liquid was $T \sim 8$ K and so still far from the pursued superfluid [88].

At present, the only experimental signatures of superfluid p-H_2 come from experiments with small doped clusters [5]. By measuring the rotational spectra of the embedded molecule it was possible to determine the effective moment of inertia of the cluster and thus the superfluid fraction. These experiments show significant evidence of superfluidity in clusters made up of $N \leq 18$ molecules. Larger clusters of up to $N \sim 10^4$ molecules down to a temperature $T = 2$ K have recently been produced but with no signature of superfluidity due to this still too high temperature [89]. Another way of frustrating the formation of the crystal was the generation of continuous hydrogen filaments of macroscopic dimensions, but again without signature of superfluidity [90].

On the theoretical side, the search for superfluidity in p-H_2 has been intense in the last decades. The well-known radial interaction between the molecules and the progress achieved in quantum Monte Carlo methods have allowed for accurate results in different geometries. To frustrate the crystal formation and reduce the strength of the interactions it was proposed to work with a two-dimensional geometry with some impurities arranged in a periodic lattice [91, 92]. First results obtained within this scheme found finite superfluid densities but posterior simulations were not able to reproduce these signatures [93–95]. The greatest effort was devoted to the study of small clusters, both pure [96–105] and doped with impurities [106–108]. There is an overall consensus that p-H_2

becomes superfluid at temperatures smaller than 1-2 K and that the superfluid fraction decreases fast with the number of molecules of the cluster. For $N > 18 - 25$ the superfluidity vanishes and solid-like structures are observed.

Recently, there has been interest in the study of p-H_2 in quasi-one-dimensional environments [109–111]. Again, the idea is to reduce dimensionality to soften the intermolecular attraction. Quantum Monte Carlo calculations of hydrogen adsorbed inside narrow pores of different size and nature have been performed showing, in some cases, the existence of inner channels which behave as effectively one-dimensional systems. Interestingly, a recent ground-state quantum Monte Carlo calculation [110] has shown that the inner channel of p-H_2 adsorbed inside a (10,10) armchair carbon nanotube is superfluid.

In this chapter, we study the one-dimensional character of narrow channels of p-H_2 and determine the Luttinger parameter [112–115] as a function of the linear density. We have studied three different cases: a purely 1D array of molecules, p-H_2 inside a (10,10) carbon nanotube preplated with an incommensurate layer of hydrogen, and p-H_2 confined harmonically to move in a channel of different widths. Our results show that moving from 1D to quasi-1D reduces effectively the interaction producing an increase of the Luttinger parameter. However, this slight increment is not enough to arrive to the superfluid-like behavior within Luttinger theory. The system breaks its homogeneity when crossing the spinodal point and this is clearly before of getting superfluity, in contradiction with the recent findings of Ref. [110].

4.2 Confinement potentials

We use the PIGS method, as explained in section 2.6, in order to study the ground-state energy and structural properties of quasi-one-dimensional p-H_2. We have used a Jastrow model with McMillan correlation factors, $\psi_{\rm m}(\boldsymbol{R}) = \prod_{i<j} \exp(-0.5(b/r_{ij})^5)$, with $b = 3.71$ Å. The Hamiltonian of the system is

$$H = \frac{\hbar^2}{2m} \sum_{i=1}^{N} \boldsymbol{\nabla}_i^2 + \sum_{i<j}^{N} V(r_{ij}) + \sum_{i=1}^{N} U(r_i) \ , \tag{4.1}$$

with $V(r)$ the intermolecular interaction and $U(r)$ the confining potential in the quasi-1D simulations.

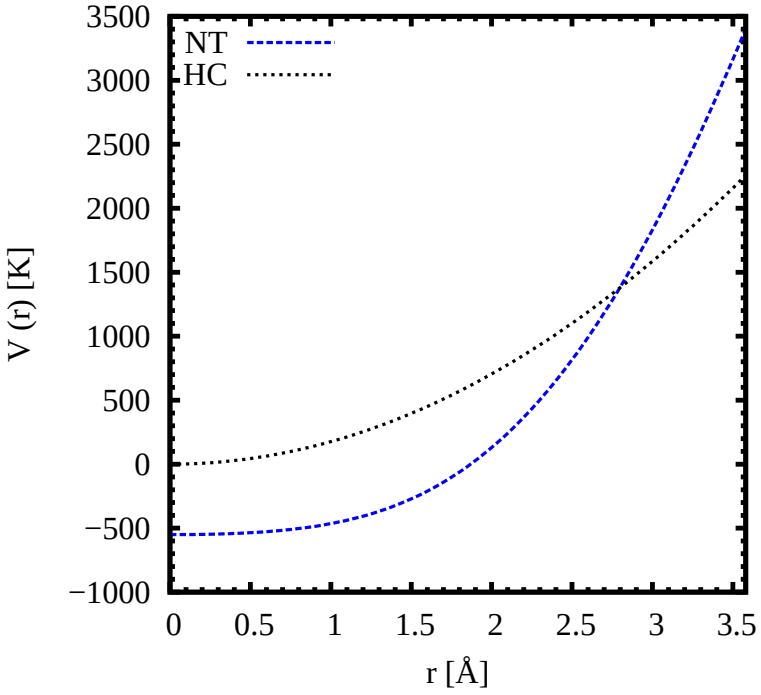

Fig. 4.1 External potential profiles for NT and HC quasi-1D systems. Harmonic case with $r_0 = 0.51$ Å.

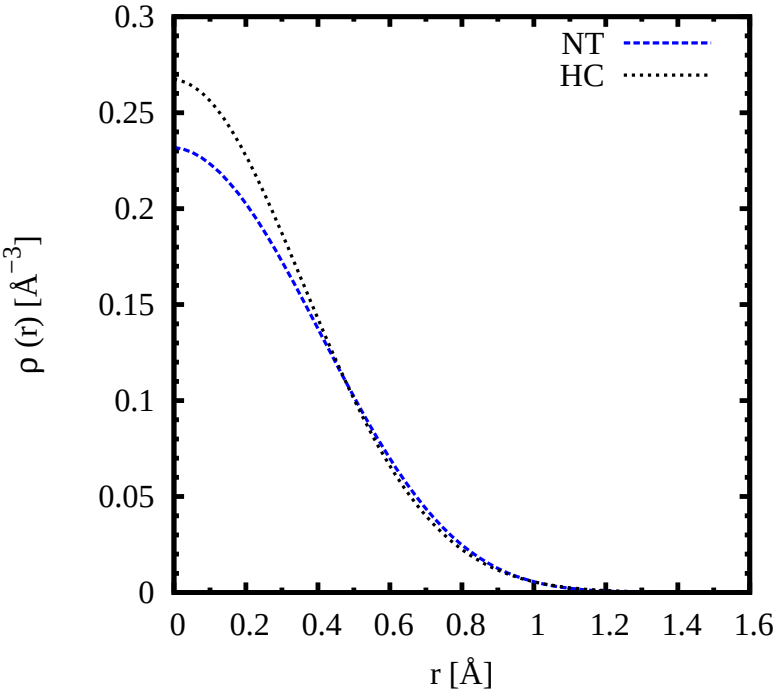

Fig. 4.2 Radial density profile for NT and HC quasi-1D systems at the equilibrium density. Harmonic case with $r_0 = 0.51$ Å.

Upon the condition of moderate pressures, it is justified to use a radial interaction between p-H_2 molecules because in the *para* state the H_2 molecule is spherically symmetric with a total angular momentum zero. We use the semi-empirical Silvera-Goldman potential [116] which has been extensively used in the past. When the system is not strictly 1D, we include an external potential $U(r)$ which confines in the radial direction. In particular, for the quasi-1D calculations we have worked on two cases. In a first one, we study the inner channel inside a (10,10) carbon nanotube (NT) of radius $R = 6.80$ Å preplated with an incommensurate lattice of p-H_2 of density $\sigma = 0.112$ Å^{-2}. This configuration coincides with the one obtained in Ref. [110] for the same nanotube. In our case, we obtain the potential $U(r)$ as a sum of the interaction that an H_2 molecule located at an r distance to the center would feel due to the C atoms of the nanotube and the H_2 molecules of the inert layer. At difference with other approaches which used the potential inside the nanotube by direct integration of the Lennard-Jones potential [117, 118], we include here explicitly the real positions of the atoms and then summed up all to give the total interaction. The C-H_2 potential is of Lennard-Jones type, with the same parameters than in Ref. [109].

The second model to study the effects of departing from a strictly 1D geometry is a harmonic potential $U(r) = \hbar^2/(2mr_0^4)(x^2 + y^2)$, with r_0 a parameter which controls the strength of the harmonic confinement (HC). A similar harmonic model was used recently in a PIMC simulation [111]. Both potential profiles are shown in Fig. 4.1. We adjusted the parameter r_0 in the HC case to be close to the particle density profile of the NT case. By taking $r_0 = 0.51$Å we obtain in fact very similar density profiles, as shown in Fig. 4.2.

We used $N = 30$ in the major part of our simulations; partial runs with larger number of particles were also performed but the results were not significantly different, almost for the quantities of our interest. The time step was $\Delta\tau = 10^{-3}$ K^{-1} and convergence was achieved at imaginary times $\tau \simeq 0.25$ K^{-1}.

4.3 Equation of state

The energy per particle as a function of the linear density ρ is shown in Fig. 4.3 for the three studied systems: 1D, (10,10) carbon nanotube (NT), and harmonic confinement (HC). Coming back to the energy results, one can see that near the equilibrium point the equations of state are rather similar (in the NT and HC cases we have subtracted to the energy per particle the energy of a single molecule in the same environment). The equilibrium densities ρ_0 for 1D, NT,

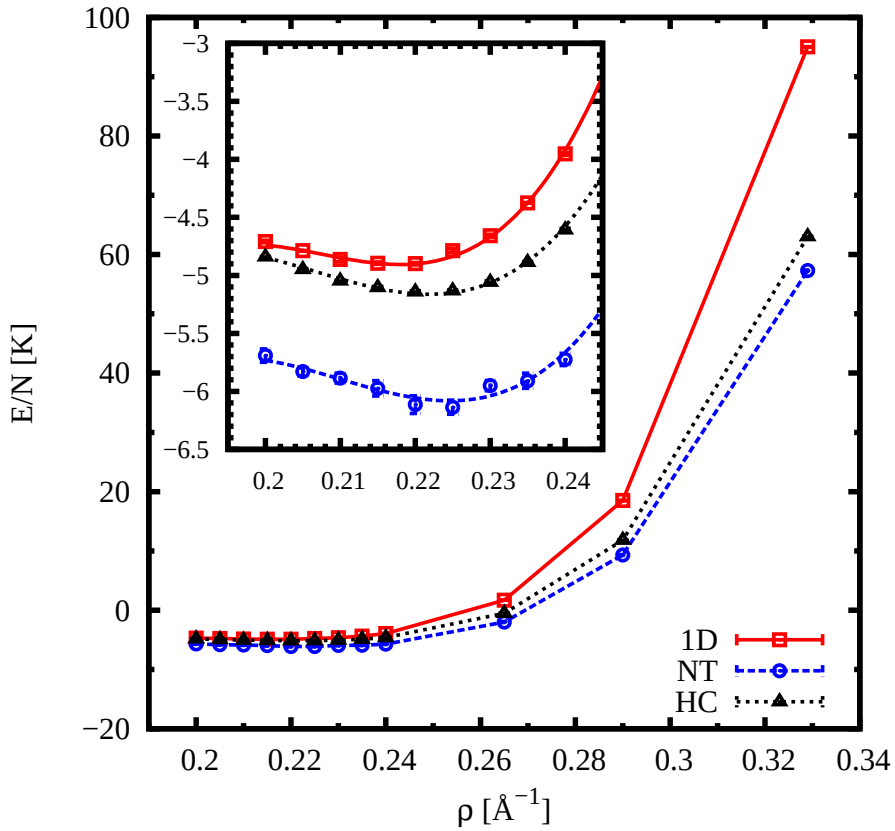

Fig. 4.3 Energy per particle of p-H_2 as a function of the density. The insert shows the same values around the equilibrium density. Harmonic case with $r_0 = 0.51$ Å.

and HC are 0.218(2), 0.224(2), and 0.221(2) Å^{-1}, respectively (numbers within parenthesis are the statistical errors). The possibility of movement in the radial direction makes that the quasi-1D configuration equilibrates at a slightly larger density with respect to the 1D limit. On the other hand, the spinodal point ρ_s, defined as the point where the speed of sound becomes zero, appears in quasi-1D at densities statistically indistinguishable of the 1D limit, $\rho_s = 0.208$ Å^{-1}. However, the most significant effect of opening the radial direction is produced at large densities in which the growth of the energy with the density is clearly steeper in 1D than in the NT and HC cases.

The results for equilibrium energy and spinodal point have been obtained by fitting a polynomical function with the energy per particle data. The spinodal point can be reached by searching the point when the speed of sound goes to zero. The Luttinger parameter could theoretically be accessed in the same way,

but it seems that the proximity of the spinodal point hinders its calculation at densities below the equilibrium. We can recover better results for the Luttinger parameter by extracting them from structural properties, such as the static structure factor or the pair distribution function.

4.4 Static structure factor for different confinements

In this section we present the results of the static structure factor obtained as explained in section 2.5.4 for the three studied cases. For the quasi-1D cases, the static structure factor is calculated along the z-direction of the system.

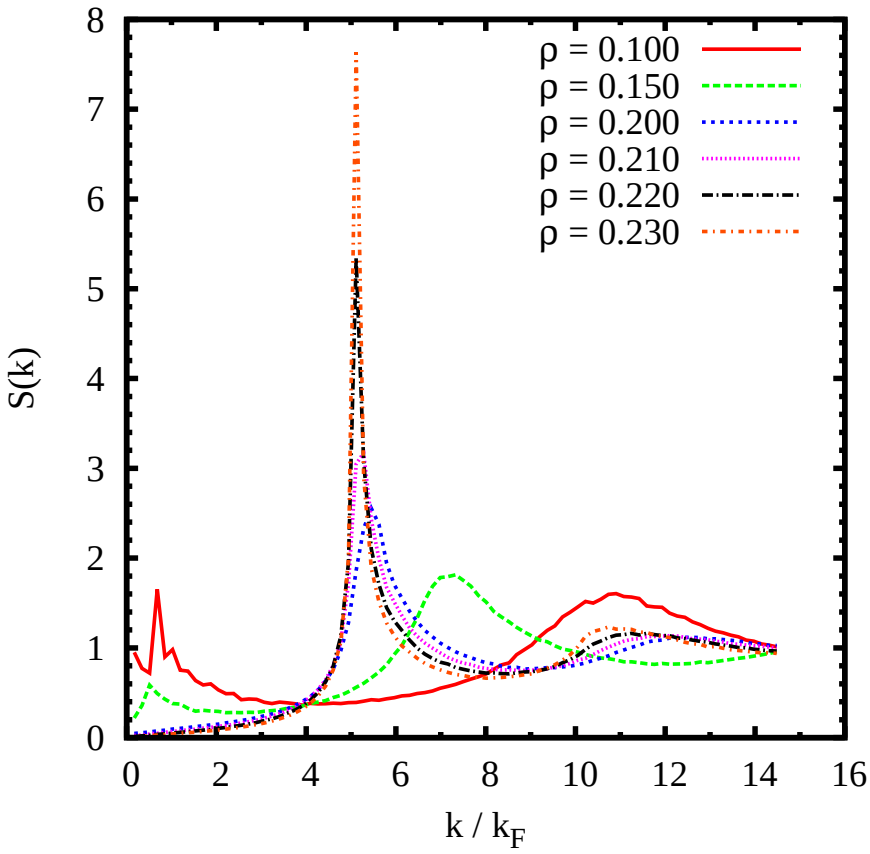

Fig. 4.4 Static structure factor for one-dimensional H_2 at different densities (in $Å^{-1}$).

In 1D systems with gapless excitation spectrum, $\varepsilon(k) = \hbar kc$ when $k \to 0$, one can make use of the Luttinger liquid theory. This phenomenological

theory predicts the large-distance (small momenta) of the distribution functions. Within this model, the results are universal in terms of the Luttinger parameter K. In a homogeneous system, like the one we are studying here, K is determined by the Fermi velocity $v_{\rm F} = \hbar k_{\rm F}/m$ and the speed of sound through the relation $K = v_F/c$. In 1D, the Fermi momentum is $k_{\rm F} = \pi\rho$. The estimation of K for different densities requires of a full many-body calculation since the speed of sound depends strongly on the intermolecular interaction.

According to Luttinger theory [112–115], the pair distribution function in one dimension behaves at large distances as

$$g(z) = 1 - \frac{K}{2(k_{\rm F}z)^2} + \sum_{l=1}^{\infty} A_l \frac{\cos(2lk_{\rm F}z)}{|k_{\rm F}z|^{2l^2K}} \ , \tag{4.2}$$

that is a sum of oscillating terms modulated by a power-law decaying amplitude. The exponents of the attenuation are only dependent on the Luttinger parameter K, whereas the amplitudes A_l of each term of the sum are determined within the Luttinger theory. The oscillations in $g(z)$ (4.2) can produce divergences at momentum values $k = 2lk_{\rm F}$. This can be observed in the static structure factor $S(k) = \langle\hat{\rho}(k)\hat{\rho}^(-k)\rangle$, with $\hat{\rho}(k) = \sum_i \exp(-ikz)$. In fact, the height of the l peak in $S(k)$ is given by

$$S(k = 2lk_{\rm F}) = A_l N^{1-2l^2K} \ , \tag{4.3}$$

which diverges with the number of particles N for values $K < 1/(2l^2)$. In particular, the first peak diverges when $K < 1/2$. In Luttinger theory this regime is termed quasicrystal for the resemblance to Bragg peaks in two and three dimensions. However, a *true* crystal in 2D and 3D shows real Bragg peaks in which the height of the peak increases linearly with N whereas in 1D this only happens when asymptotically $K \to 0$.

In Fig. 4.4, we report results for the static structure factor $S(k)$ at different densities. The limit of stability of the homogeneous phase, signaled by the spinodal point $\rho_s = 0.208$ Å^{-1}, is clearly shown in the results. As one can see, below the spinodal, and when $k \to 0$, the static structure factor shows an anomalous behavior, the linear behavior is lost, and the signal of a divergence is observed. Snapshots of configurations generated along the PIGS runs also show this break of homogeneity.

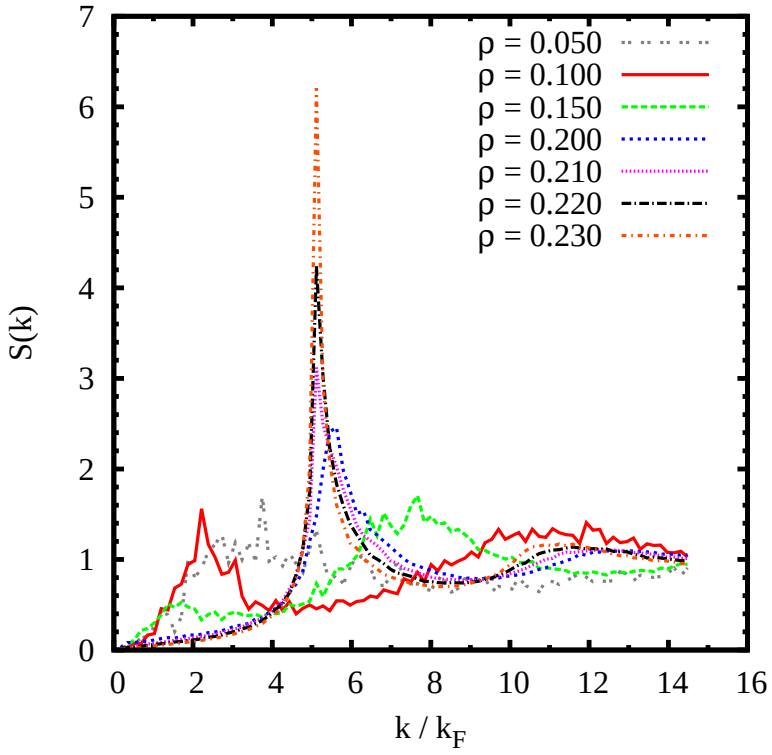

Fig. 4.5 Static structure factor for quasi-1D H_2 in the NT case at different densities (in $Å^{-1}$).

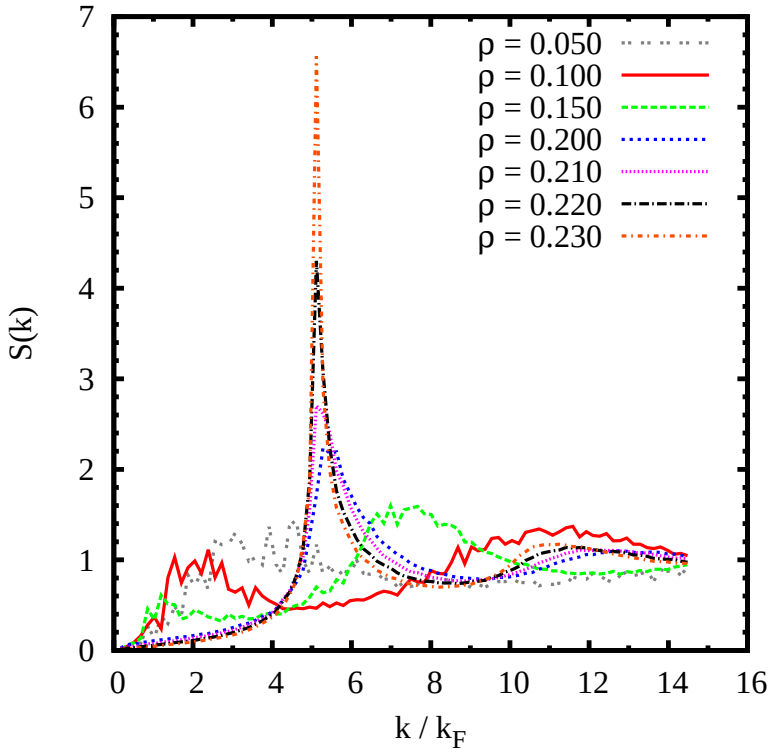

Fig. 4.6 Static structure factor for quasi-1D H_2 with harmonic confinement HC with $r_0 = 0.51$ Å at different densities (in $Å^{-1}$).

Results for $S(k)$ along the z-direction in the quasi-1D NT case are shown in Fig. 4.5. Above the spinodal point, the behavior of $S(k)$ is very similar to the purely 1D case shown in Fig. 4.4, with a clear linear phononic behavior when $k \to 0$. From this behavior we estimate the speed of sound and the Luttinger parameter K.

A similar analysis has been carried out in the case of a quasi-1D system with harmonic confinement HC. The PIGS results for $S(k)$ are shown in Fig. 4.6 at several densities. The observed behavior is quite close to the NT case since the density profiles in both cases are very similar (Fig. 4.2), and one observes the break of homogeneity at the spinodal point too.

4.5 Luttinger parameter as a function of density

From the low-k linear behavior of $S(k)$ we can obtain the speed of sound c,

$$S(k \to 0) = \frac{\hbar k}{2mc} , \tag{4.4}$$

and, from it, the Luttinger parameter K. The dependence of K with the density is shown in Fig. 4.7. For the 1D case it has a value ~ 0.3 at the equilibrium density and decreases monotonically with ρ. The spinodal point is quite close to ρ_0 and thus 1D p-H_2 remains always in the quasicrystal regime.

The same can be done for the quasi-1D cases. Results of K as a function of the density for the NT case are also shown in Fig. 4.7. At equal linear density, the K values in the NT configuration are systematically larger than in purely 1D due to the effective reduction of the intermolecular interaction produced by the opening of radial movements. However, it still remains $K < 1/2$, i.e., in the quasicrystal regime. When the density is lowered below the spinodal point the system breaks its homogeneity. As in the previous analyzed 1D case, this instability is clearly shown in the results of $S(k)$ (Fig. 4.5). In spite of having larger statistical noise than in 1D, due to the radial degree of freedom, one can see as the linear k dependence at low k is lost and a tendency to divergence is observed. For the HC case, there is a break of homogeneity at the spinodal point and the results for K in this case are also very similar to the NT case. These are also shown in Fig. 4.7; close to the equilibrium density K in HC is slightly smaller than in NT but then both results converge to common values when the density grows.

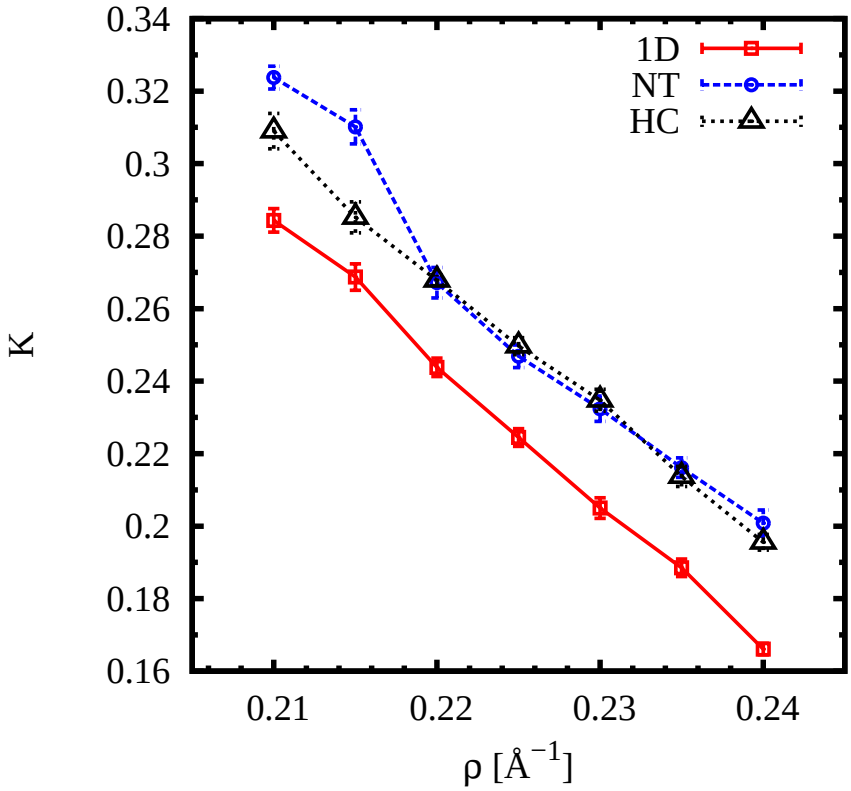

Fig. 4.7 Luttinger parameter K for the three systems under study as a function of the density.

One can check that the Luttinger liquid theory applies to this quasi-1D system by checking if the asymptotic behavior of the computed $g(z)$ is well reproduced by Eq. (4.2) using the K value obtained from the low k linear behavior of $S(k)$. As one can see in Fig. 4.8, the agreement with Luttinger theory is excellent confirming our premises.

The quasi-1D results for the Luttinger parameter show an enhancement of its value with respect the purely 1D geometry. An interesting question is to know if this increase could be even larger if one releases slightly the radial confinement, producing setups that depart more from the 1D constraint. We have explored this possibility by tunning the strentgh r_0 of the harmonic confinement HC. In Fig. 4.9, we show results for $S(k)$ for the HC model at a fixed density $\rho = 0.22$ Å^{-1} and varying the parameter $r_{=}0$ in the range 0.1-1.5 Å. When the Gaussian potential is narrow enough, $r_0 \leq 0.5$ Å, the static structure factor is very similar to the 1D case, with a linear slope at low k and with a strength

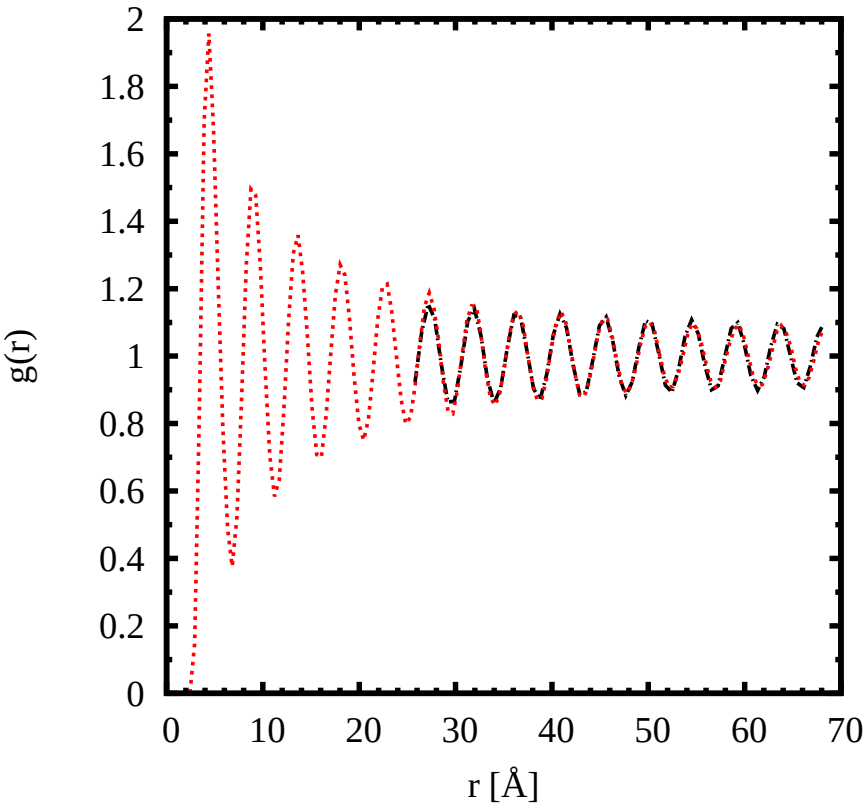

Fig. 4.8 Two-body distribution function for the NT configuration at the equilibrium density. The red line is the PIGS result and the black one corresponds to the asymptotic behavior predicted by Luttinhger theory (4.2) with K derived from the low$-k$ behavior of $S(k)$.

of the peak decreasing slightly with r_0. However, when $r_0 \geq 0.8$Å $S(k)$ shows an anomalous behavior, with a main peak located at very small k. This reflects that the system breaks its homogeneity. In fact, we observe in snapshots of the simulations as the system aggregates in clusters of larger density.

In Fig. 4.10, we show results for K within the HC model as a function of the strength of the confinement r_0. They are obtained at the same linear density $\rho = 0.22$ Å^{-1} and within the r_0 range in which the system is stable. We observe a linear increase of K with r_0 up to $r_0 \simeq 1$Å and then it tends to decrease slowly. At 1.3 Å$K = 0.35$, a value which is significantly larger than in 1D at the same density $K = 0.25$, but still below the threshold for reaching the quasi-superfluid regime.

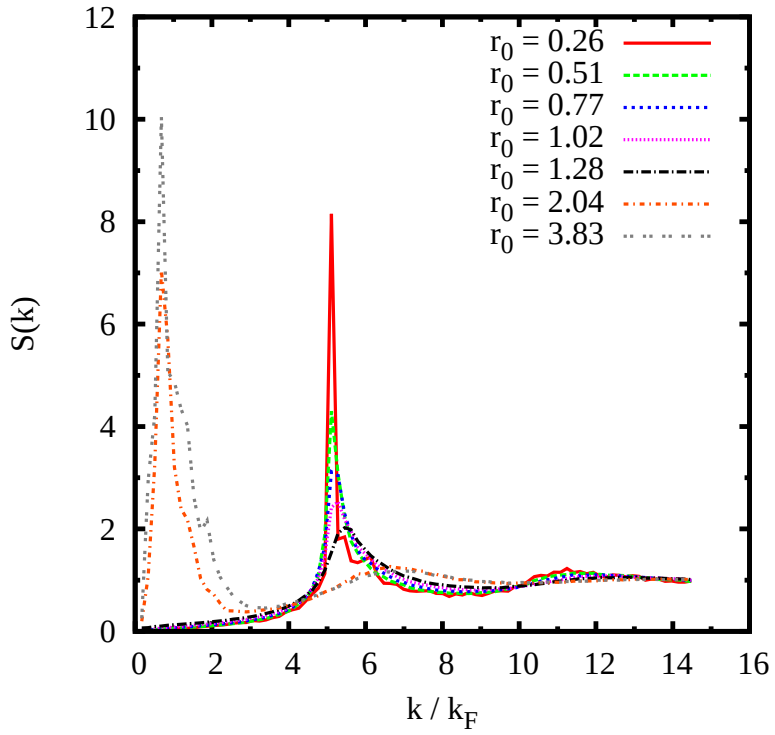

Fig. 4.9 Static structure factor for the quasi-1D H_2 system with harmonic confinements (HC) of different strength, at a fixed density $\rho = 0.22$ Å^{-1}.

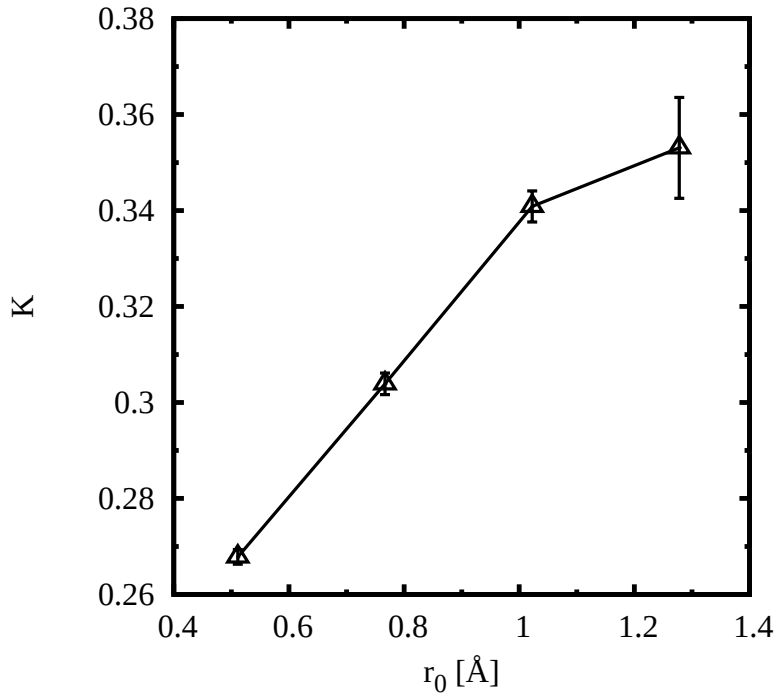

Fig. 4.10 Luttinger parameter of the quasi-1D HC model at density $\rho = 0.22$ Å^{-1} as a function of the strength of the confinement r_0.

4.6 Summary

By means of the path integral ground state Monte Carlo method we have studied the ground-state (zero temperature) properties of 1D and quasi-1D p-H_2. For the quasi-1D case we have used two models: the inner channel inside a (10,10) carbon nanotube preplated with H_2 and a radial harmonic confinement with variable strength. The calculation of the equations of state in the three cases has allowed for an accurate determination of the equilibrium densities of the three systems. As expected, ρ_0 increases slightly when radial direction opens because the strong H_2-H_2 interaction is effectively reduced. The effect is however quite small. The spinodal point of the three problems is indistinguishable within our numerical resolution and remains very close to ρ_0.

From the low-k behavior of the static structure factor we estimate the speed of sound, and from it, the Luttinger parameter K. In this way, we report results for the evolution of K with the density. K decreases monotonically with ρ in all cases. In all the density regime in which the system is stable, $K < 1/2$ and thus, according to Luttinger theory p-H_2 is a quasi-crystal. For a particular density, we observe as K increases going from strictly 1D to quasi-1D but the effect is not large enough to surpass the quasi-crystal threshold.

Chapter 5

Dynamic structure factor of ^{4}He across the normal-superfluid transition

In this chapter we have carried out a microscopic study of the dynamic structure factor of liquid ^{4}He across the normal-superfluid transition temperature using the path integral Monte Carlo method. The ill-posed problem of the inverse Laplace transform, from the imaginary-time intermediate scattering function to the dynamic response, is tackled by stochastic optimization. Our results show a quasi-particle peak and a small and broad multiphonon contribution. In spite of the lack of strength in the collective peaks, we clearly identify the rapid dropping of the roton peak amplitude when crossing the transition temperature T_λ. Other properties such as the static structure factor, static response, momentum distribution, and one-phonon contribution to the response are also calculated at different temperatures. The changes of the phonon-roton spectrum with the temperature are also studied. An overall agreement with available experimental data is achieved.

We have also carried out a study of the momentum distribution across the normal-superfluid transition temperature. Our results in the superfluid regime show that a kink is present in the range of momenta corresponding to the roton excitation. This effect disappears when crossing the transition temperature to the normal fluid, in a behavior currently unexplained by theory.

5.1 Introduction

The most relevant information on the dynamics of a quantum liquid is contained in the dynamic structure factor $S(\boldsymbol{q},\omega)$, which is experimentally measured by means of inelastic neutron scattering [119]. Probably, superfluid ^{4}He has been the most deeply studied system from both theory and experiment and a great deal of information about it is nowadays accessible [120]. For many years, liquid ^{4}He was the only quantum fluid showing Bose-Einstein condensation and superfluidity until the discovery of the fully Bose-Einstein condensate in 1995 [6, 7]. Therefore, the number of measures of $S(\boldsymbol{q},\omega)$ at different temperatures and momentum transfer has been continuously growing, with more refined data along the years [121–126]. The emergence of strong quasi-particle peaks going down the normal-superfluid transition ($T_\lambda = 2.17$ K) has been associated with the superfluidity of the system by application of the Landau criterium. Much of the interest on the dynamics of strongly-correlated liquid ^{4}He is then related to the effects on the dynamics of this second-order λ-transition.

In the limit of zero temperature, the richest and most accurate microscopic description of the dynamic response of liquid ^{4}He has been achieved by progressively more sophisticated correlated basis function (CBF) theory [127]. The development of this theory has been stimulated by the continuous improvement of the experimental resolution in inelastic neutron scattering. Recently, Campbell *et al.* [128] have incorporated three-body fluctuations in an extended CBF approach and proved a remarkable improvement of both the excitation spectrum and full $S(\boldsymbol{q},\omega)$, with features not so clearly seen before and that are in nice agreement with the most recent experimental data [129].

As we already know, the most accurate tools to deal with ground-state properties are the quantum Monte Carlo (QMC) methods (see section 2.1), which simulate quantum systems using imaginary-time dynamics since they are intended for achieving the lowest-energy state. Therefore, having no access to real-time evolution one looses the possibility of getting the dynamic structure factor by a Fourier transform of the intermediate scattering function $F(\boldsymbol{q},t)$, as it happens in simulations of classical systems using Molecular Dynamics. Quantum simulations are able to sample this time-dependent function but in imaginary time τ, $F(\boldsymbol{q},\tau)$, and from it to get the dynamic response through an inverse Laplace transform. But it is well known that this inverse transform is an ill-posed problem. This means, at the practical level, that the always finite statistical error of QMC data makes impossible to find a unique solution for the dynamic structure factor.

Inverse problems in mathematical physics are a long-standing topic in which elaborated regularization techniques have been specifically developed [130]. Focusing on the inversion of QMC data, to extract the dynamic response, several methods have been proposed in the last years. Probably, the most used approach is the Maximum Entropy (ME) method which incorporates some a priori expected behavior through an entropic term [131]. This method works quite well if the response is smooth but it is not able to reproduce responses with well-defined peaks. In this respect, other methods have recently proved to be more efficient than ME. For instance, the average spectrum method (ASM) [132], the stochastic optimization method (SOM) [133], the method of consistent constraints (MCC) [134], and the genetic inversion via falsification of theories (GIFT) method [135] have been able to recover sharp features in $S(\boldsymbol{q},\omega)$ which ME smoothed out. All those methods are essentially stochastic optimization methods using different strategies and constraints. It is also possible to work out the inverse problem without stochastic grounds [136] by using the Moore-Penrose pseudoinverse and a Tikhonov regularization [137]. Other approaches try to reduce the ill-conditioned character of this inverse problem by changing the kernel from the Laplace transform to a Lorentz one [138]. Finally, the computation of complex-time correlation functions has been recently realized in simple problems and proved to be able to severely reduce the ill-nature of the Laplace transform [136].

In our work, we use the PIMC method to estimate the dynamic response of liquid ^{4}He in a range of temperatures covering the normal-superfluid transition at $T_\lambda = 2.17$ K. The inversion method from imaginary time to energy is carried out via the simulated annealing method, which is a well-known stochastic multidimensional optimization method widely used in physics and engineering [139]. Our method is rather similar to the GIFT one [135] but changing the genetic algorithm by simulated annealing. The GIFT method was applied to the study of the dynamic response of liquid ^{4}He at zero temperature and proved to work much better than ME, producing a rather sharp quasi-particle peak and also some structure at large energies, corresponding to multiparticle excitations [135]. The temperature dependence of $S(\boldsymbol{q},\omega)$ has been much less studied. Apart from a quantum-semiclassical estimation of the response at high q [140], the only reported results where obtained by combining PIMC and the ME method which worked well in the normal phase but not in the superfluid part [141]. Therefore, the significant effect of the temperature on the dynamics of the liquid through the λ transition was lost. We show that the improvement on the inversion method leads to a significantly better description of $S(\boldsymbol{q},\omega)$ in

all the temperature range studied, with reasonable agreement with experimental data.

Apart from the effects on the dynamic structure factor, it is also interesting the behavior of the momentum distribution of the ^{4}He atoms $n(\mathbf{k})$, that is notably different in the two sides of the transition with the change being mainly in the limit of low momenta. First of all, in the superfluid regime, the presence of a condensate gives rise to a sharp delta contribution at $\mathbf{k} = 0$. Furthermore, $n(\mathbf{k})$ shows a singular $1/k$ behavior which can be explained in terms of a coupling between the condensate and the long-wavelength excitations (phonons) [142, 143]. On the other hand, the width of $n(\mathbf{k})$ increases slightly with T by a merely thermal effect. However, some theoretical calculations in the limit of zero temperature point out that the shape of $n(\mathbf{k})$ presents a change in the slope, or a kink, at $k \simeq 2$ Å^{-1} [144–146], i.e. in the regime of momenta in which the dynamic structure factor displays a strong quasiparticle peak corresponding to the roton. This tiny effect was not studied in previous calculations at finite temperature [13]. It is therefore plausible to think that the kink in $n(\mathbf{k})$ can be related to the roton mode, in a similar way as the $1/k$ divergence at low momenta is ascribed to phonons.

In this sense, a second aim of the work contained in this chapter is to investigate the relation between the presence of the kink in $n(\mathbf{k})$ and that of the roton-mode in $S(\mathbf{k}, \omega)$. Our results do show that, as the liquid enters the normal phase, the kink is slowly smoothed out and the strength of the roton mode vanishes, supporting thus the hypothesis that the kink in the momentum distribution is a signal of the presence of the roton mode.

5.2 Simmulated annealing as a stochastic optimization

We use the path integral Monte Carlo method, as explained in chapter 2, in order to obtain results about static properties of ^{4}He at different temperatures crossing the normal-superfluid transition. We are mainly interested in calculating the intermediate scattering function $F(\boldsymbol{q}, \tau)$ (section 2.5.5), from which we recover the dynamic properties of the system.

The function $F(\boldsymbol{q}, \tau)$ is the Laplace transform of the dynamic structure factor $S(\boldsymbol{q}, \omega)$ which satisfies the detailed balance condition,

$$S(\boldsymbol{q}, -\omega) = e^{-\beta\omega} S(\boldsymbol{q}, \omega) \ , \tag{5.1}$$

relating the response for negative and positive energy transfers ω. Taking into account Eq. (5.1), one gets

$$F(\boldsymbol{q},\tau) = \int_0^\infty d\omega \; S(\boldsymbol{q},\omega)(e^{-\omega\tau} + e^{-\omega(\beta-\tau)}) \; . \tag{5.2}$$

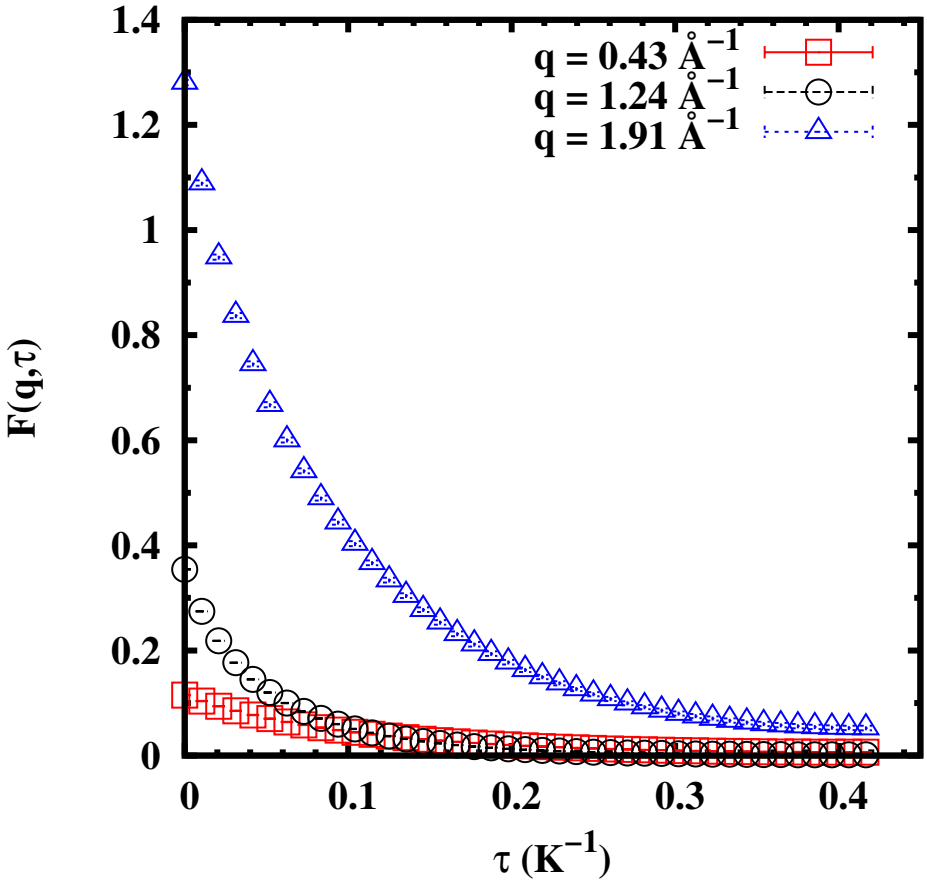

Fig. 5.1 Intermediate scattering function computed for ^{4}He at saturated vapor pressure ($\rho = 0.021858\,\text{Å}^{-3}$) and $T = 1.2$ K, for different values of q.

The intermediate scattering function is periodic with τ, as it can be immediately seen from Eq. (5.2): $F(\boldsymbol{q},\beta-\tau) = F(\boldsymbol{q},\tau)$. Therefore, it is necessary to sample this function only up to $\beta/2$ (half of the polymer representing each particle in PIMC terminology). From the PIMC simulation, one samples $F(\boldsymbol{q},\tau)$ at the discrete points in which the action at temperature T is decomposed.

In Fig. 5.1, we show the characteristic behavior of $F(\boldsymbol{q},\tau)$ for three different q values at $T = 1.2$ K. These are monotonously decreasing functions ending at a finite value at $T/2$ which approaches zero when $T \to 0$. The initial point at $\tau = 0$ corresponds to the zero energy-weighted sum rule of the dynamic response,

which in turn is the static structure factor at that specific q value,

$$m_0 = S(\boldsymbol{q}) = \int_{-\infty}^{\infty} d\omega \; S(\boldsymbol{q}, \omega) \; . \tag{5.3}$$

With the PIMC results for $F(\boldsymbol{q}, \tau)$, the next step is to find a reasonable model for $S(\boldsymbol{q}, \omega)$ having always in mind the ill-conditioned nature of this goal. In our scheme, we assume a step-wise function,

$$S_{\mathrm{m}}(q, \omega) = \sum_{i=1}^{N_s} \xi_i \; \Theta(\omega - \omega_i) \, \Theta(\omega_{i+1} - \omega) \; , \tag{5.4}$$

with $\Theta(x)$ the Heaviside step function, and ξ_i and N_s parameters of the model. As our interest relies on the study of homogeneous translationally invariant systems, the response functions depend only of the modulus q. Introducing $S_{\mathrm{m}}(q, \omega)$ in Eq. (5.2), one obtains the corresponding model for the intermediate scattering function,

$$\begin{aligned} F_{\mathrm{m}}(q, \tau) = \sum_{i=1}^{N_s} \; \xi_i \quad & \left[\frac{1}{\tau} \left(e^{-\tau \omega_i} - e^{-\tau \omega_{i+1}} \right) \right. \\ & \left. + \frac{1}{\beta - \tau} \left(e^{-(\beta - \tau) \omega_i} - e^{-(\beta - \tau) \omega_{i+1}} \right) \right] \end{aligned} \tag{5.5}$$

Written in this way, the inverse problem is converted into a multivariate optimization problem which tries to reproduce the PIMC data with the proposed model, Eq. 5.5. To this end, we use the simulated annealing method which relies on a thermodynamic equilibration procedure from high to low temperature according to a predefined template schedule. [139] The cost function to be minimized is the quadratic dispersion,

$$\chi^2(q) = \sum_{i=1}^{N_p} \left[F(q, \tau_i) - F_{\mathrm{m}}(q, \tau_i) \right]^2 \; , \tag{5.6}$$

with N_p the number of points in which the PIMC estimation of the intermediate scattering function is sampled. Eventually, one can also introduce as a denominator of Eq. (5.6) the statistical errors coming from the PIMC simulations. However, we have checked that this is not affecting so much the final result since the size of the errors is rather independent of τ.

The optimization leading to $S(q, \omega)$ is carried out over a number N_t of independent PIMC calculations of $F(q, \tau)$. Typically, we work with a population $N_t = 24$ and for each one we perform a number $N_a = 100$ of independent sim-

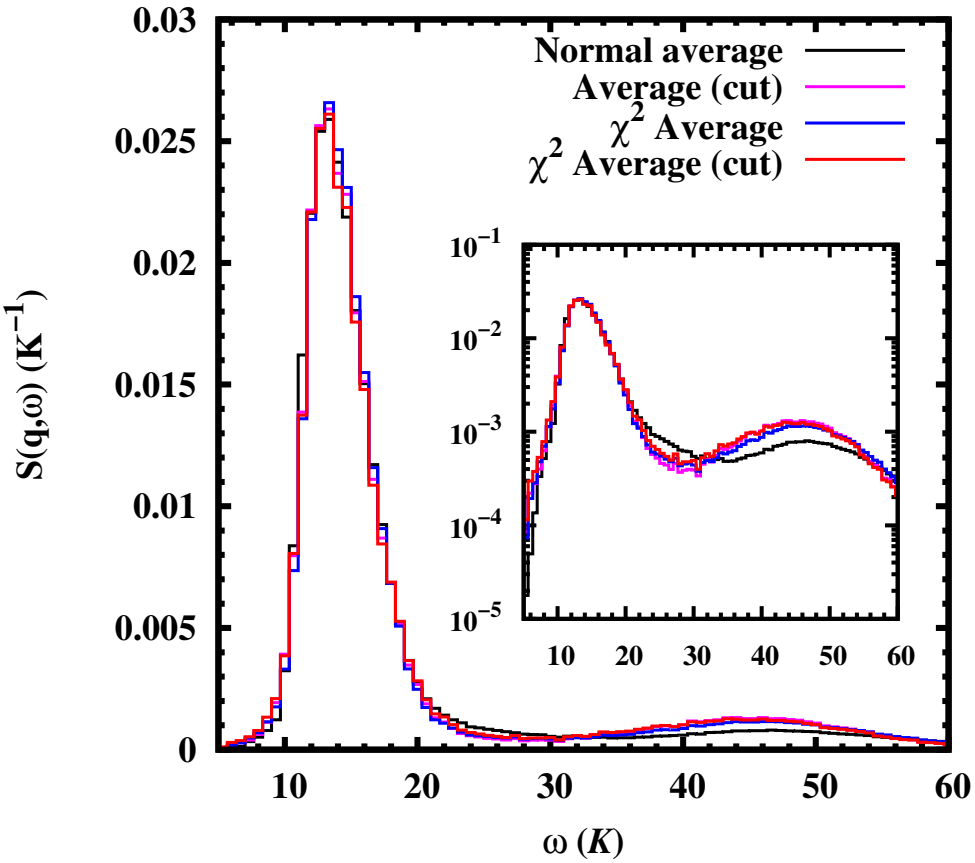

Fig. 5.2 Dynamic structure factor at $T = 1.2$ K, saturated vapor pressure (SVP), and $q = 0.76$ Å^{-1} using different averaging methods. Inset shows same data but using a log scale in the y-axis.

ulated annealing searches. The mean average of these N_a optimizations is our prediction for the dynamic response for a given $F(q,\tau)$. We also register the mean value of χ^2 (Eq. 5.6) of the N_a optimizations. As an example, the mean value of χ^2 in a simulation with data at $T = 1.2$ K and $q = 1.91$ Å^{-1} is $2.19 \cdot 10^{-5}$, with minimum and maximum values of $2.37 \cdot 10^{-6}$ and $3.80 \cdot 10^{-4}$, respectively. At this same temperature, $N_p = 41$ and the number of points of the model $S(q,\omega)$ (Eq. 5.5) is $N_s = 150$.

With the outcome for the N_t series we have tried different alternatives to get the final prediction. We can take just the statistical mean of the series or a weighted mean, in which the weight of each function is the inverse of its corresponding χ^2, to give more relevance to the best-fitted models. Additionally, we have also tried to make both of these estimations but selecting the 20% best functions according to its χ^2. In Fig. 5.2, we plot the results obtained following these different possibilities. All the results are quite similar, with

minor differences; only at large energies we can observe that the weighted mean gives slightly more structure (see inset in Fig. 5.2). Also, the effect of selecting the best χ^2 models seems to be not much relevant

5.3 Comparisons with the Maximum Entropy method

Is interesting to compare our results obtained for the dynamic structure factor at $T = 1.2$ K and saturated vapor pressure (SVP) with previous results obtained using the Maximum Entropy (ME) method [141]. This is done in Fig. 5.3. The ME results are significantly broader, mainly at the lowest q value, and with only smooth features. This broadening is probably a result of the entropic prior used in those estimations, which seems to favor smooth solutions. In the figure, we can observe that the position of the ME peak is coincident with ours but the ME solution lacks of any structure beyond the quasi-particle peak. In our estimation, we do not use any prior information in the search of optimal reconstructions and thus it is free from any a priori information except that the function is positive definite for any energy. Moreover, the simulated annealing optimization leads to dynamic responses that fulfil the energy-weighted sum rules m_0 and m_1,

$$m_1 = \int_{-\infty}^{\infty} d\omega \; \omega S(q,\omega) = \frac{\hbar^2 q^2}{2m} \; , \tag{5.7}$$

without imposing them as constraints in the cost function (Eq. 5.6). Also, the m_{-1} sum-rule, related to the static response, is in agreement with experiment (section 5.4).

As the intermediate scattering function $F(q,\tau)$ used in both estimations is different and used by different authors it could happen that the differences observed in Fig. 5.3 were due more to the differences between the calculated imaginary-time response than to the inversion method itself. To clarify this point, we can perform two additional comparisons.

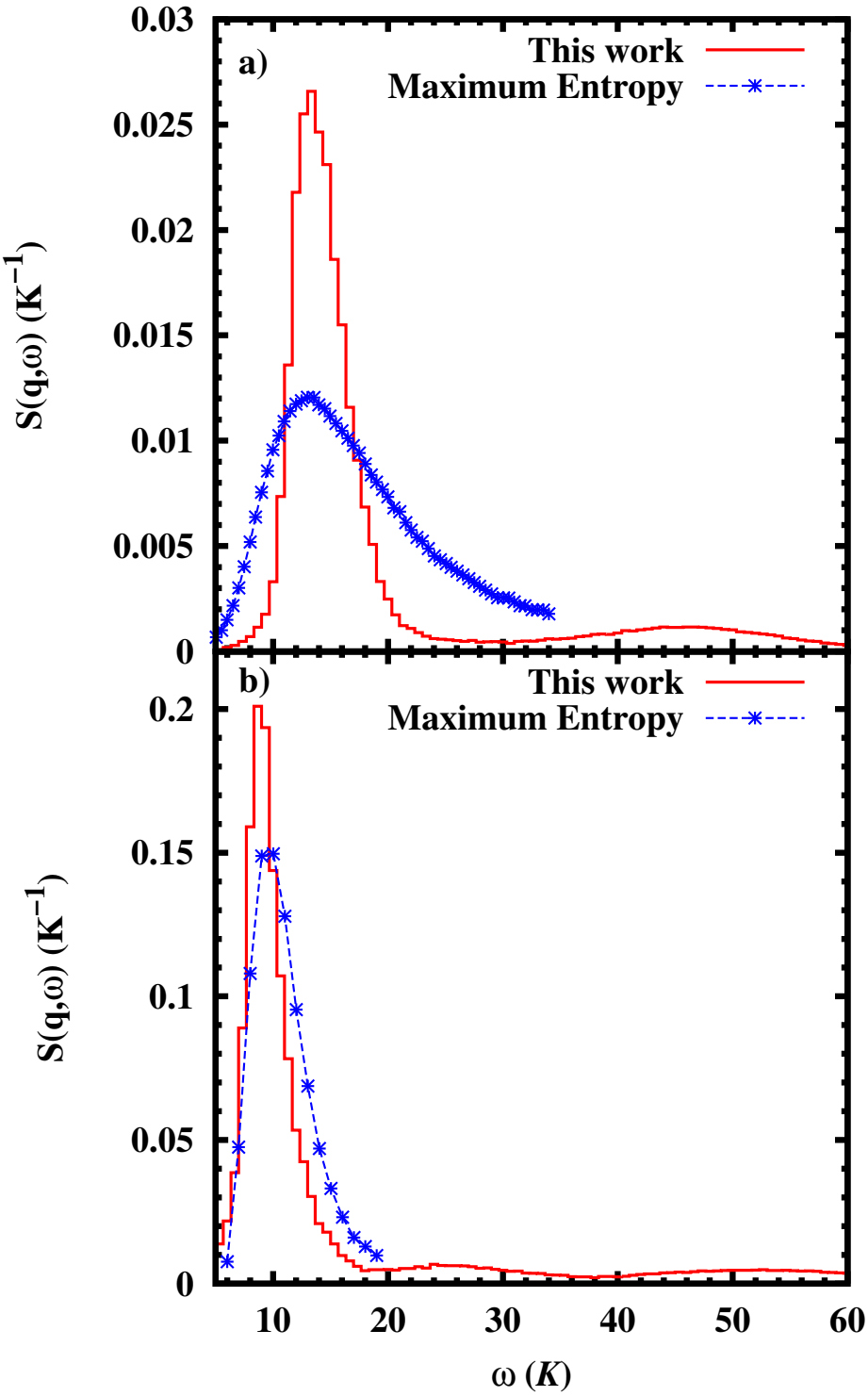

Fig. 5.3 Comparison between the present results for the dynamic structure factor and those obtained in Ref. [141] using the maximum entropy method for $q = 0.76$ Å^{-1}(a) and 1.81 Å^{-1} (b). Both results are calculated at SVP and $T = 1.2$ K.

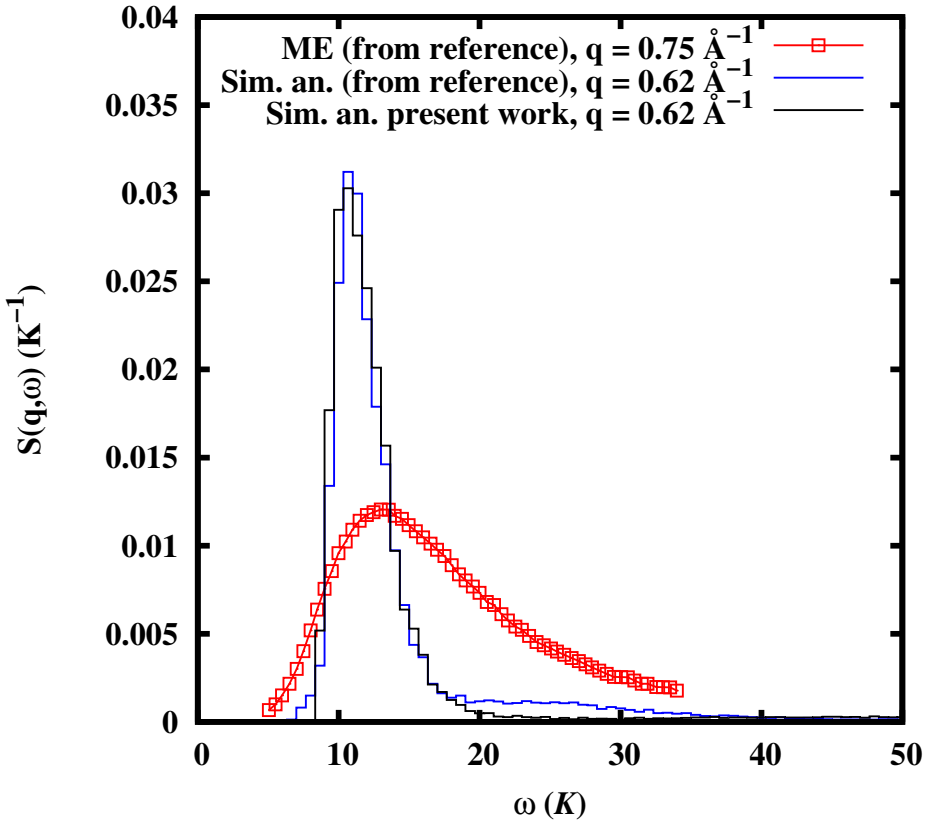

Fig. 5.4 Comparison between the dynamic response obtained with ME and our stochastic optimization method using intermediate scattering data from Ref. [141].

In Fig. 5.4, we report results for $S(q,\omega)$ at $q = 0.62$ Å^{-1} using our imaginary-time data and stochastic optimization. In the figure, we also show the dynamic response that we have obtained by applying our inversion method to the imaginary-time data reported in Ref. [141]. Finally, the figure also shows the ME results reported in Ref. [141] but for a slightly different q value since results for $q = 0.62$ Å^{-1} are not given in that paper. As one can see, starting from their published data and applying our method the results compare favorably with our response $S(q,\omega)$. Therefore, the different quality of the input data is so small that no effect is observed.

In order to make a more clear comparison between both inversion methods we show in Fig. 5.5 results for the dynamic response using our data for $F(q,\tau)$. At the same q value than in Fig. 5.4, we report results obtainded with stochastic optimization and using the ME method. The results are similar to the ones shown in Fig. 5.4 and lead to the same conclusion, that is, the ME method

generates smoother functions than our method. This conclusion is in agreement with a similar analysis reported by Vitali *et al.* [135].

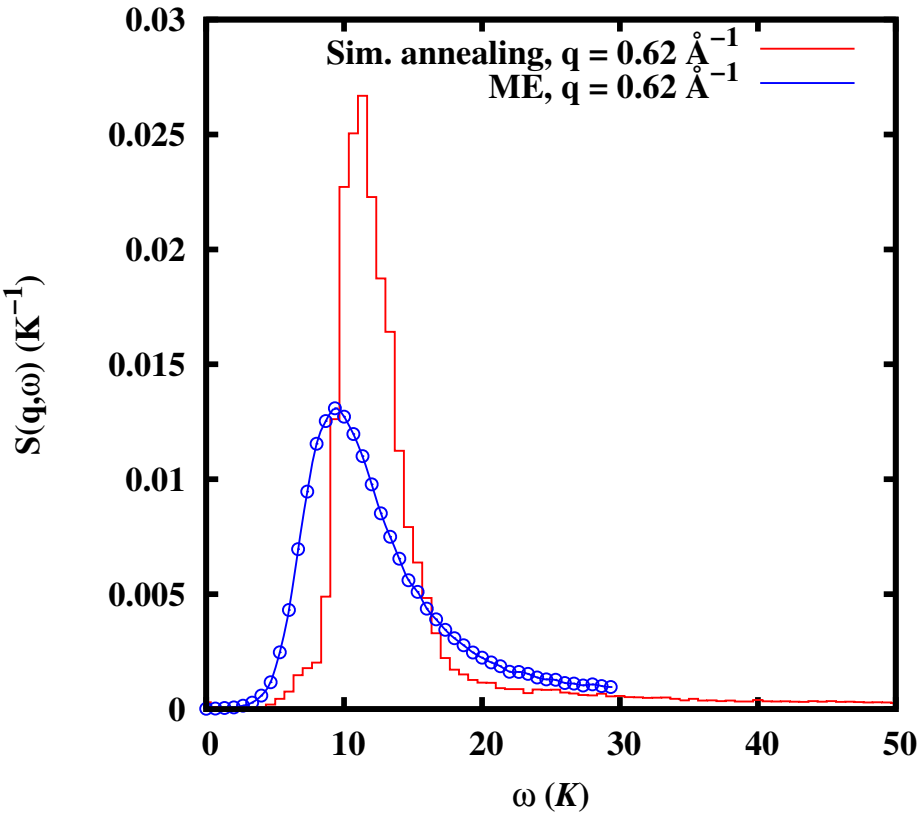

Fig. 5.5 Comparison between the dynamic response obtained with ME and our stochastic optimization method using our intermediate scattering data.

5.4 Comparisons with experiments

We have performed PIMC calculations of liquid ^{4}He following the SVP densities, from $T = 0.8$ to 4 K. The interatomic potential is of Aziz type [147] and the number of particles in the simulation box, under periodic boundary conditions, is $N = 64$. In some cases we have used a larger number of particles ($N = 128$) without observing any significant change in $F(q, \tau)$. The number of convolution terms M is large enough to eliminate any bias coming from the path discretization; we used $\tau = 0.0104$ K^{-1}.

We compare our result for the dynamic response in the superfluid phase with experimental data from Ref. [121] in Fig. 5.6. The theoretical peak is located around an energy which is very close to the experimental one but it is still broader than in the experiment. However, the strength (area) of this peak

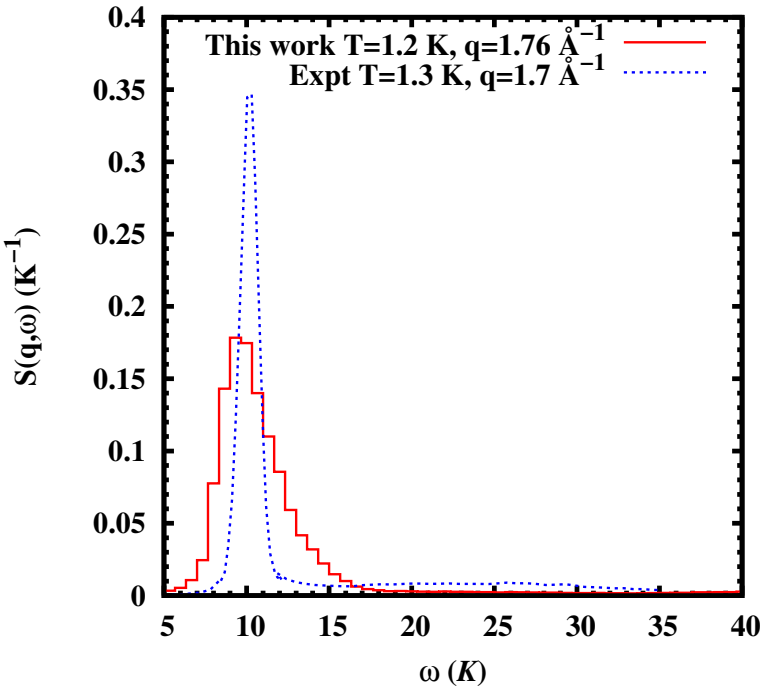

Fig. 5.6 Dynamic structure factor at $T = 1.2$ K and $q = 1.76\,\text{Å}^{-1}$ compared with experimental data ($T = 1.3K$, $q = 1.7\,\text{Å}^{-1}$) [121].

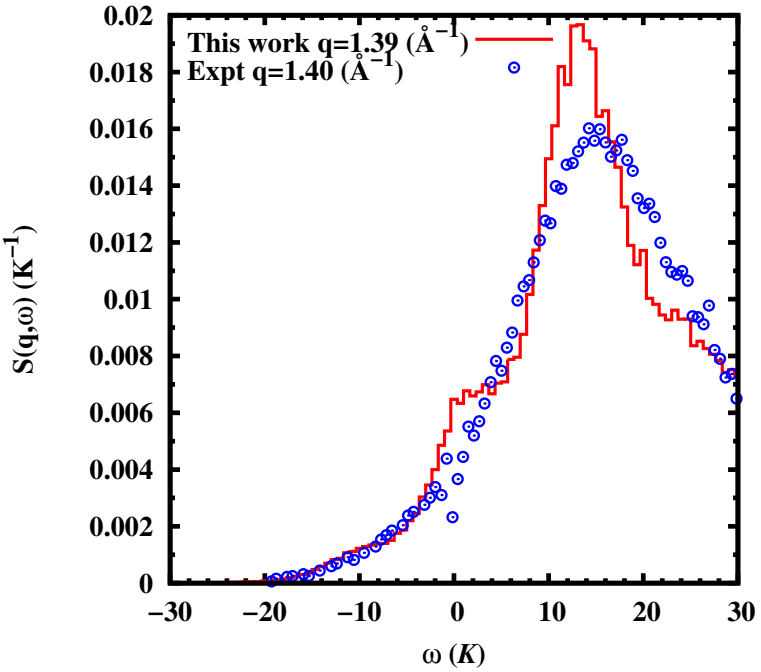

Fig. 5.7 Dynamic structure factor at $T = 4.0$ K and $q = 1.40\,\text{Å}^{-1}$. The experimental data is from Ref. [121].

is in good agreement with the experimental one, as we will comment later. The quasi-particle peak disappears in the normal phase, above T_λ, as we can see in Fig. 5.7. In this figure, we compare our results at $T = 4$ K with experimental outcomes at the same T. In this case, we see that both the position of the peak and its shape is in an overall agreement with the experiment.

5.5 Dynamic structure factor in the momentum-energy plane

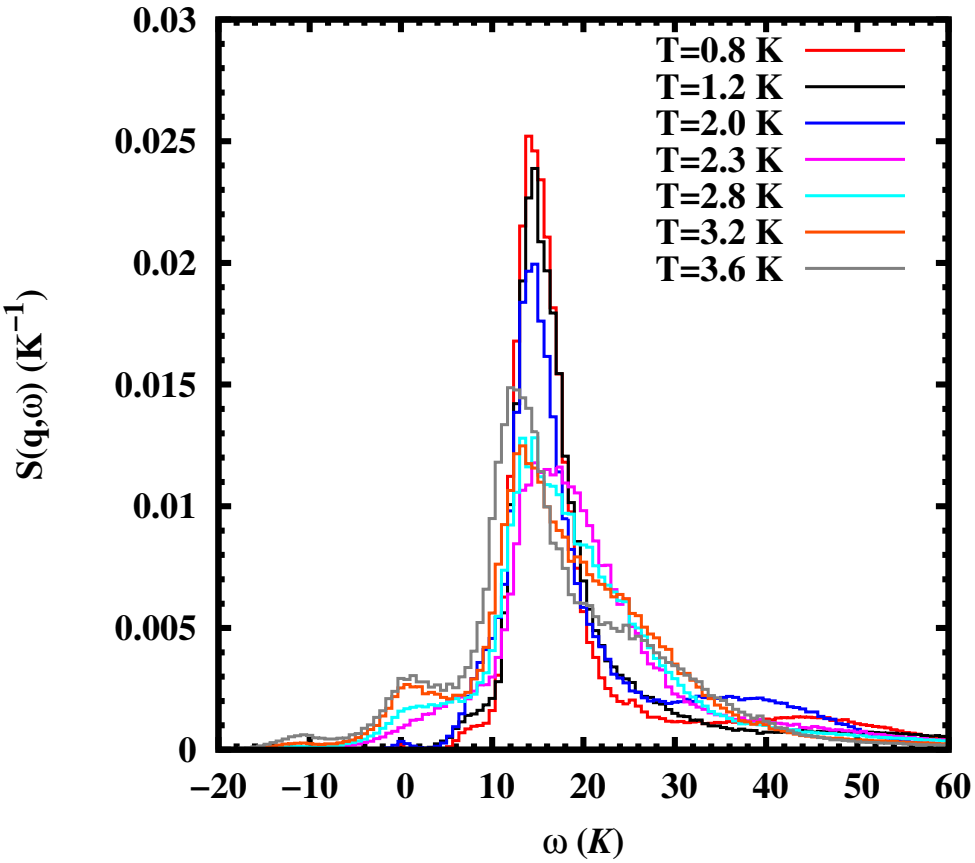

Fig. 5.8 Dynamic structure factor of liquid ^{4}He for $q = 0.88\,\text{Å}^{-1}$ at different temperatures.

One of the main goals of our study has been the study of the effect of the temperature on the dynamics of liquid ^{4}He. In Fig. 5.8, we report results of $S(q,\omega)$ in a range of temperatures from $T = 0.8$ to 4 K in the phonon region of the spectrum, with $q = 0.88$ Å^{-1}. At this low q value, the behavior with T is not much different for the superfluid and normal phases, a feature which is also

observed in neutron scattering data [120]. We observe a progressive broadening of the peak with T which appears already below T_λ and continues above it. Even at the highest temperature $T = 4$ K, we identify a collective peak corresponding to a sound excitation [120]. The main difference between both regimes is that the quasi-particle energy below T_λ is nearly independent of T whereas, in the normal phase, this energy decreases in a monotonous way.

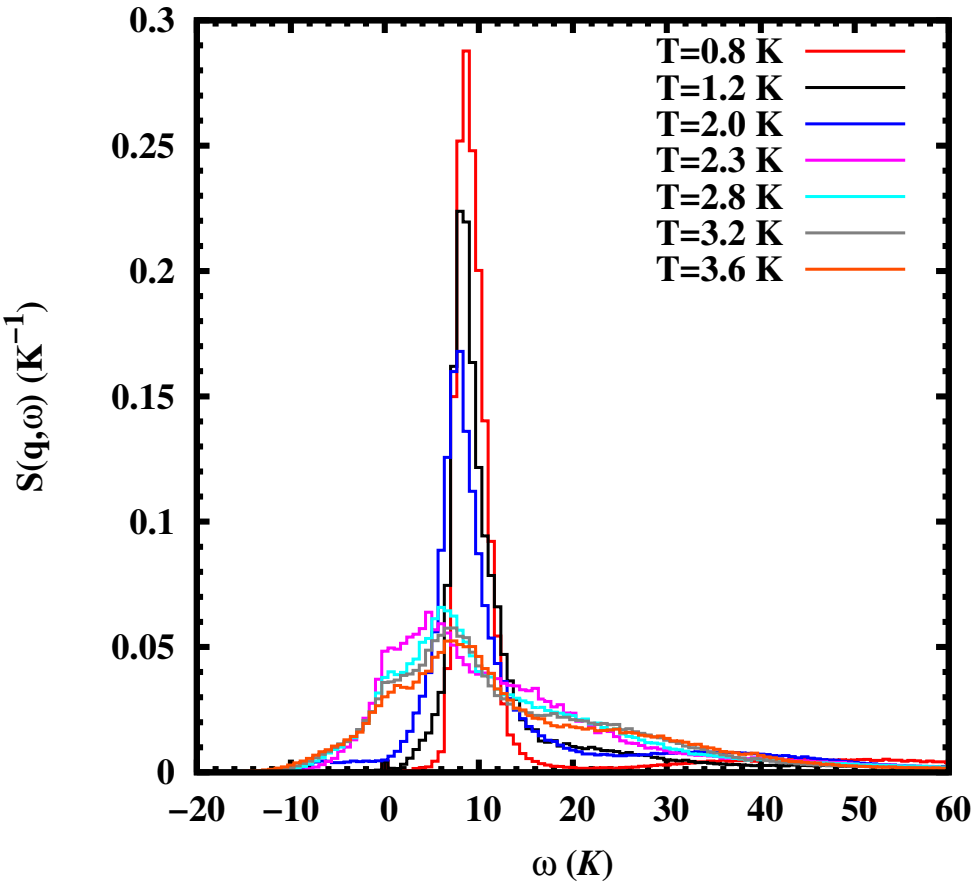

Fig. 5.9 Dynamic structure factor of liquid ^{4}He for $q = 1.91\,\text{Å}^{-1}$ at different temperatures.

Near the roton, the dependence of the dynamic response with T is significantly different. In Fig. 5.9, we report results of $S(q,\omega)$ at $q = 1.91$ Å^{-1} at different temperatures across T_λ. The most relevant feature is the drop of the quasi-particle peak for $T > T_\lambda$. In the superfluid phase, the peak remains sharp with a nearly constant energy. Just crossing the transition (in our data for $T \geq 2.3$ K), the peak disappears and only a broad response is observed, with an energy that moves slightly down. According to the Landau criterium the existence of a roton gap implies a critical velocity larger than zero and thus a

superfluid phase. Our PIMC data is consistent with this picture since we observe as the resulting superfluid density, derived from the winding number estimator, goes to zero at T_λ, in agreement with the disappearance of the roton excitation in $S(q,\omega)$.

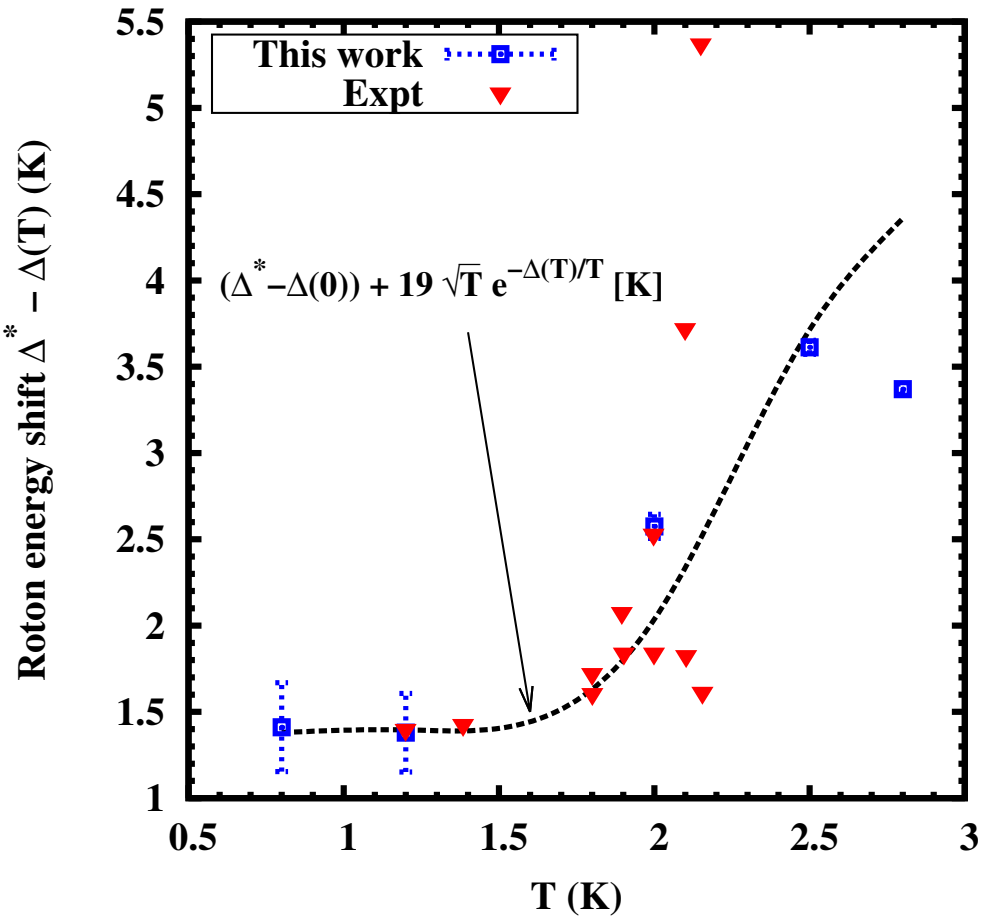

Fig. 5.10 Temperature dependence of the roton energy. The experimental points and suggested fit are from Ref. [148] with $\Delta(0) = 8.62$ K . In the fit, $\Delta^* > \Delta(T)$ stands for an arbitrary energy value.

Our results for the temperature dependence of the roton energy $\Delta(T)$ are shown in Fig. 5.10. For temperatures $T < 1.5$ K, $\Delta(T)$ is practically constant around a value 8.60 K, in agreement with experiment [148]. For larger temperatures, still in the superfluid part, this energy gap starts to decrease with the largest change around the transition temperature. For temperatures $T > 2.5$ K, the peak vanishes and $\Delta(T)$ flattens but then one really can not continue speaking about the roton mode. In the same figure we report experimental results for the roton energy in the superfluid phase. At same temperature, our results agree well with the experimental ones which show some erratic behavior around

$T \simeq 2$ K but compatible with a decrease of the roton gap with T. Still in the same figure, we report the fit used in Ref. [148], that is based on the roton-roton interaction derived from Landau and Khalatnikov theory [149]. This law seems to be right only at the qualitative level, with significant deviation with our results and still larger discrepancies with the experimental values.

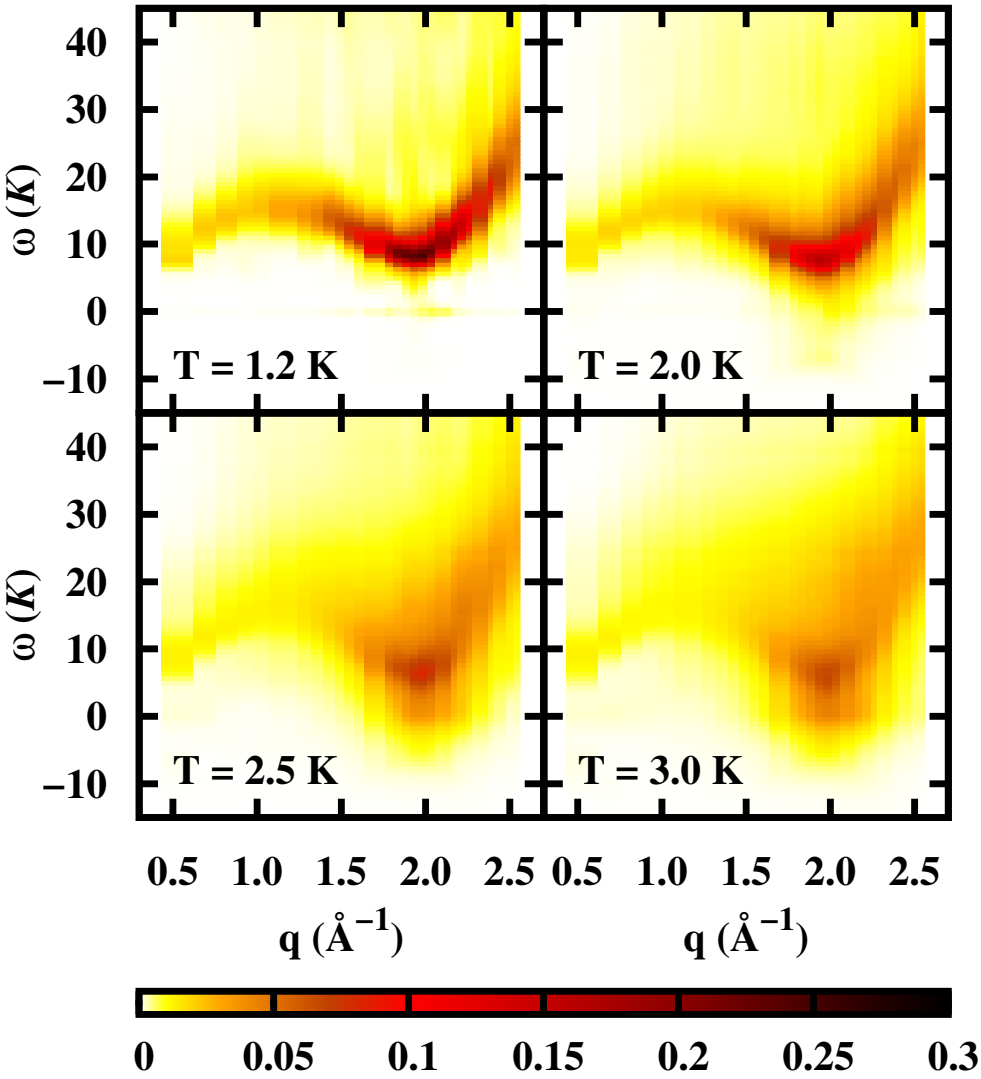

Fig. 5.11 Color map of the dynamic response in the momentum-energy plane at different temperatures, below and upper T_λ.

The results obtained for $S(q, \omega)$ in the present calculation are summarized in Fig. 5.11 as a color map in the momentum-energy plane. In the superfluid phase, the phonon-roton curve is clearly observed, with the highest strength of the quasi-particle peak located in the roton minimum, in agreement with experiment. The multiparticle part above the single-mode peak is also observed but without any particular structure. At $T = 2$ K the roton peak is still observed

but some intensity starts to appear below it, At $T = 2.5$ and 3 K, we still obtain intensity in the roton but the peak, and in general, all the spectrum appears much more diffuse.

5.6 Phonon-roton spectrum

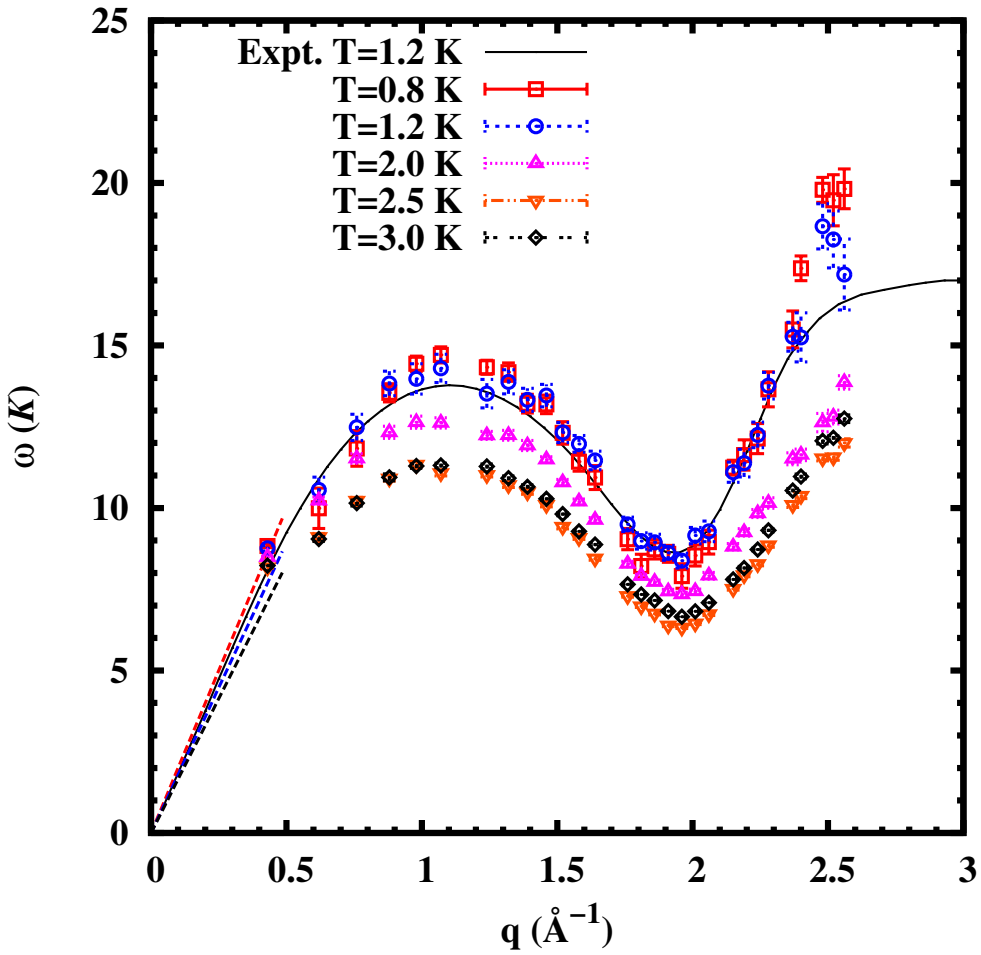

Fig. 5.12 Phonon-roton spectrum of liquid ^{4}He at different temperatures. The line corresponds to experimental data at $T = 1.2$ K [150, 151]. Straight lines at small q stand for the low q behavior, $\omega = cq$ with c the speed of sound, at temperatures $T = 0.8$, 1.2, and 3.0 K (from larger to smaller slope).

The excitation energy of the collective mode is shown in Fig. 5.12 at different temperatures. Our results at the lowest temperatures, $T = 0.8$ and 1.2 K, are indistinguishable within the statistical errors and are in close agreement with the inelastic neutron scattering data at $T = 1.2$ K from Refs. [150, 151], except at the end of the spectrum (Pitaevskii plateau). In fact, for $q > 2.5$ Å^{-1} the

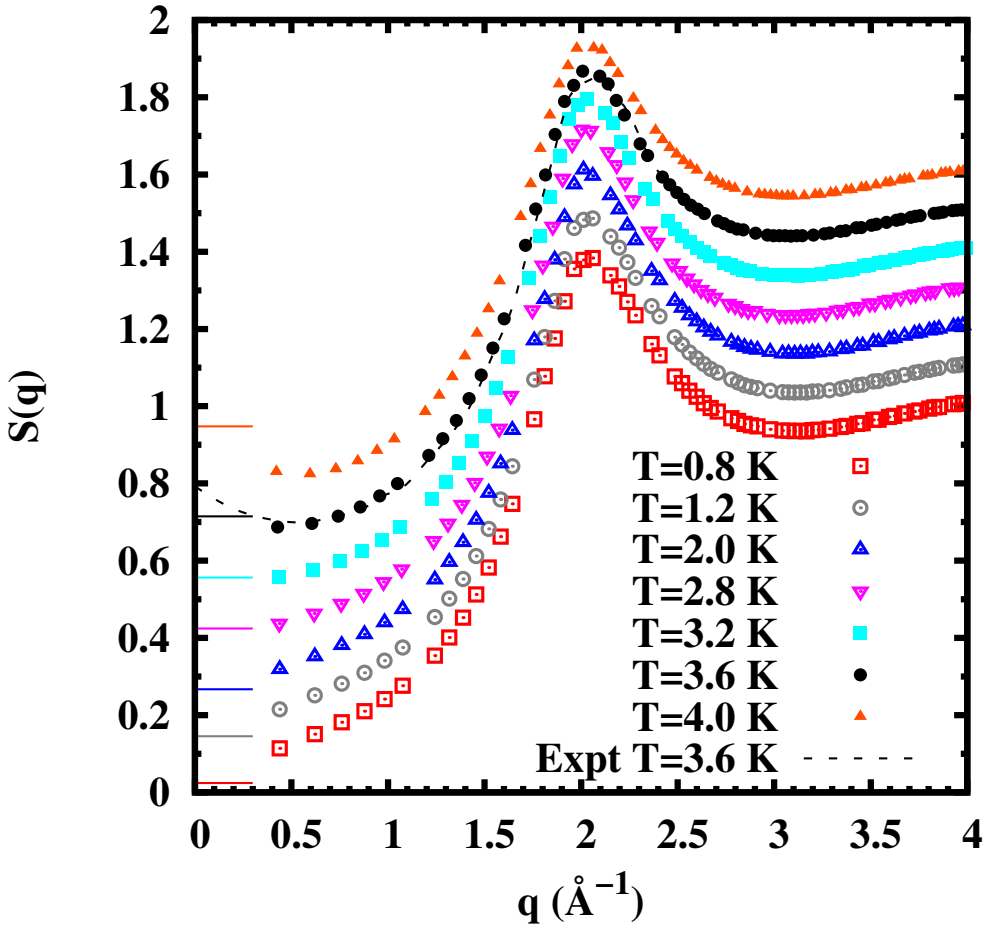

Fig. 5.13 Static structure factor $S(q)$ at different temperatures across T_λ. The results have been shifted vertically a constant value to make its reading easier. The dashed line stands for experimental data from Ref. [152]. Short horizontal lines at $q = 0$ correspond to the value (Eq. 5.8) obtained from PIMC.

dynamic response that we obtain from the reconstruction of the imaginary-time intermediate scattering function is rather broad and one can not distinguish the double peak structure observed in experiments. Also, notice that the energies corresponding to $q \lesssim 0.5$ Å^{-1} are not accessible in our simulations since our minimum $q_{\rm min}$ value is restricted to be $2\pi/L$, with L the length of the simulation box. At $T = 2$ K, very close to the superfluid transition temperature, we observe as the energies of the maxon and roton modes significantly decrease whereas the phonon part is less changed. When the temperature is above the transition, we can observe that the maximum of the peaks, now much broader, seem to collapse again in a common curve around the maxon. Instead, in the roton it seems that the energy could increase again at the largest temperature. This latter feature is quite unexpected and could be a result of our difficulty in the localization of

the maximum in a rather broad dynamic response. The overall description on the evolution of the phonon-roton spectrum with T is in close agreement with experimental data [120].

The static structure factor $S(q)$ is the zero energy-weighted sum rule of the dynamic response (Eq. 5.3). This function can be exactly calculated using the PIMC method as it is the value of the imaginary-time intermediate scattering function at $\tau = 0$. In Fig. 5.13, we show results of $S(q)$ for the range of analyzed temperatures. The effect of the temperature on the position and height of the main peak is quite small, in agreement with the x-ray experimental data from Ref. [152]. We observe a small displacement of the peak to larger q values and a simultaneous decrease of the height when T increases. These effects can be mainly associated to the decrease of the density along SVP when the temperature grows. For values $q \lesssim 0.5$ Å^{-1} we do not have available data due to the finite size of our simulation box. Therefore, we can not reach the zero momentum value which is related to the isothermal compressibility χ_T through the exact relation

$$S(q = 0) = \rho k_B T \chi_T \ , \tag{5.8}$$

with k_B the Boltzmann constant and ρ the density. The requirement of this condition produces that $S(q)$ starts to develop a minimum around $q \simeq 0.5$ Å^{-1} when T increases. Our results also show this feature but for larger T (~ 3.6 K) than in experiments (~ 3 K) due to our lack of data at low q.

5.7 Static response function and area below quasiparticle peak

From the dynamic structure factor, we can calculate the static response function $\chi(q)$ since this is directly related to the $1/\omega$ sum rule through the relation

$$\chi(q) = -2\rho \int_{-\infty}^{\infty} d\omega \, \frac{S(q,\omega)}{\omega} = -2\rho m_{-1} \ . \tag{5.9}$$

The dominant contribution to the m_{-1} sum rule is the quasi-particle peak and thus it is less sensitive to the multi-phonon part [153]. In Fig. 5.14, we report the results obtained for $\chi(q)$ at temperatures 1.2, 2.0, and 2.5 K. We observe that at low q the effect of T is negligible but around the peak, $q \simeq 2$ Å^{-1}, is really large. In the superfluid regime, the height of the peak clearly increases with T, a feature that has not been reported previously neither from theory nor from experiment. At $T = 2.5$ K, in the normal phase, the main peak decreases again

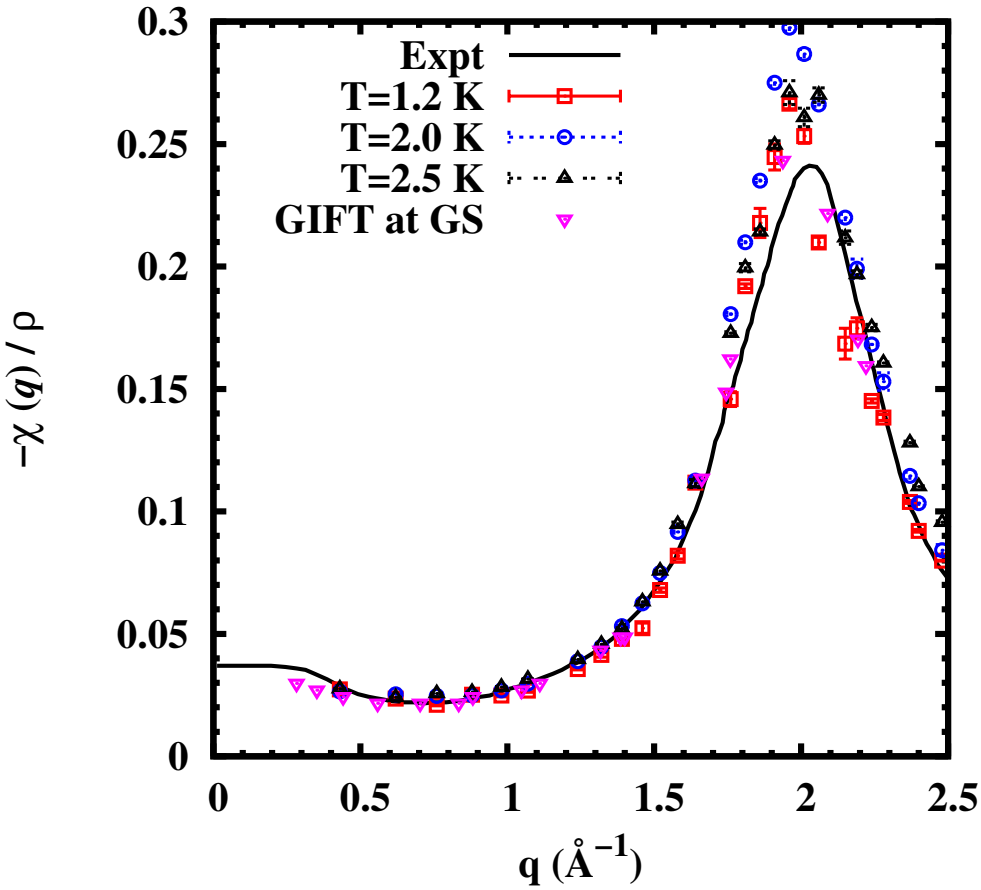

Fig. 5.14 Static response function at $T = 1.2$, 2.0, and 2.5 K. For comparison, we also report zero-temperature QMC results [135] and experimental data obtained at $T = 1.2$ K [150, 151].

in agreement with the absence of the roton. In the figure, we plot experimental data [150, 151] at $T = 1.2$ K which is close to our result at low q but with less strength in the peak. Results from QMC at zero temperature from Ref. [135] are in an overall agreement with ours at the lowest T, but somehow ours have a slightly higher peak.

The dynamic response of liquid ^{4}He is usually written as the sum of two terms,

$$S(q,\omega) = S_1(q,\omega) + S_{\rm m}(q,\omega) \ , \tag{5.10}$$

where $S_1(q,\omega)$ stands for the sharp quasi-particle peak and $S_{\rm m}(q,\omega)$ includes the contributions from scattering of more than one phonon (multiphonon part). The intensity (area) below the sharp peak is the function $Z(q)$ which we report in Fig. 5.15. Our results are compared with experimental data at $T = 1.2$ K from Refs. [150, 151]. As we commented previously, our quasi-particle peaks are

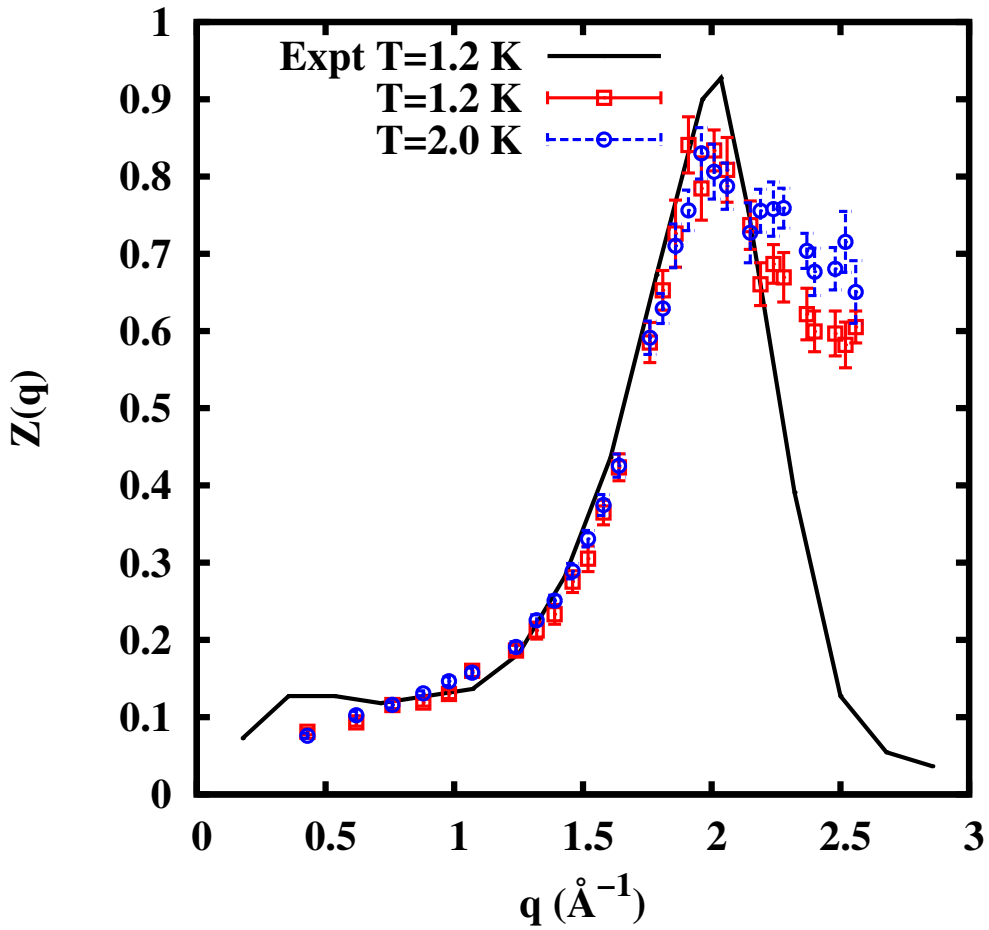

Fig. 5.15 One-phonon contribution to the dynamic response, $Z(q)$, at different temperatures. Experimental results at $T = 1.2$ K from Refs. [150, 151].

less sharp than the experimental ones due to the uncertainties in the inversion problem from imaginary time to energy. However, the area below the peak is not so far from the experimental outcomes. Up to the maximum of the peak, our results are compatible with the experimental function. However, our data lead to a peak with less strength and after that, for larger momenta, our results scatter significantly due to the difficulties in the determination of the area below the peak. The uncertainties in the area estimation do not allow for the observation of an enhancement of the peak's height when T increases, as reported in experiments [153].

5.8 Momentum distribution across λ transition

In order to study the effects of the λ transition on the momentum distribution, we need first to compute the one-body density matrix as explained in section

2.5.6. The results are shown in Fig. 5.16, sampled from non-diagonal configurations along the simulation. As it is well known, there are significant differences between results for $\rho_1(r)$ obtained below and above the critical temperature T_λ. In the superfluid regime, $T < T_\lambda$, the one-body density matrix shows a plateau at large distances corresponding to the presence of a finite occupation of the zero-momentum state. Instead, in the normal phase, $T > T_\lambda$, the one-body density matrix decays exponentially to zero pointing to the absence of off-diagonal long range order in the system.

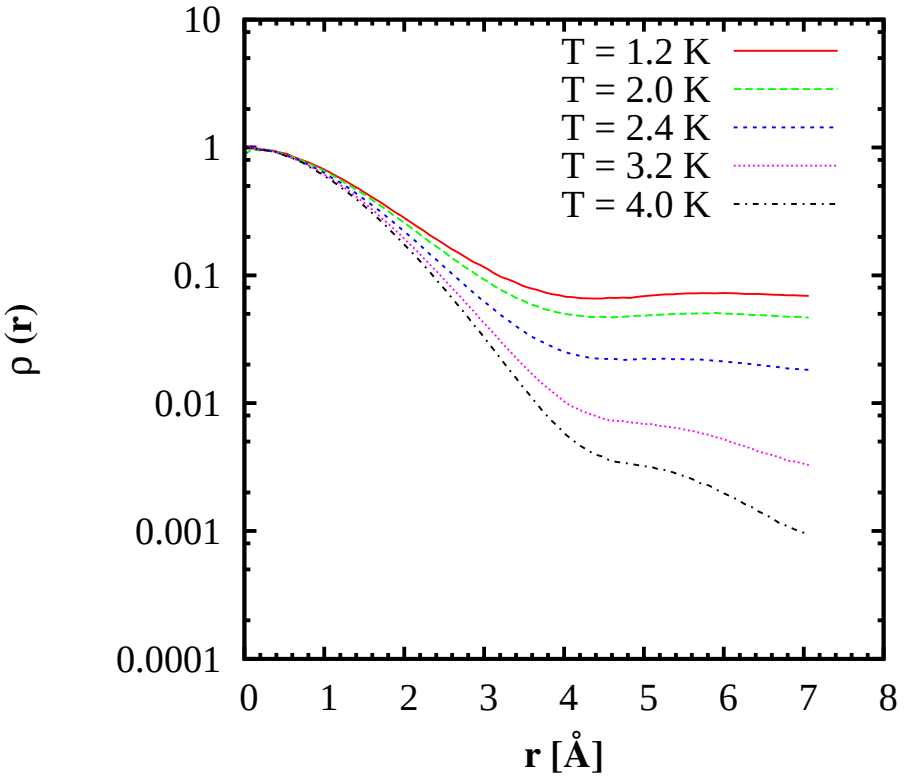

Fig. 5.16 One-body density matrix of liquid ^{4}He at different temperatures at saturated vapor pressure (SVP).

The momentum distribution $n(\boldsymbol{k})$ can be obtained from the Fourier transform of the one-body density matrix $\rho_1(\boldsymbol{r})$ as

$$n(\boldsymbol{k}) = n_0\delta(\boldsymbol{k}) + \rho \int d^3r\, e^{i\boldsymbol{k}\cdot\boldsymbol{r}}\,(\rho_1(r) - n_0)\ , \tag{5.11}$$

where ρ stands for the density of our system and $n_0 = \lim_{r\to\infty}\rho_1(r)$ is the condensate fraction. Results of $n(k)$ for a range of temperatures across T_λ are reported in Fig. 5.17, plotted as $kn(k)$. Our data start at a k value compatible

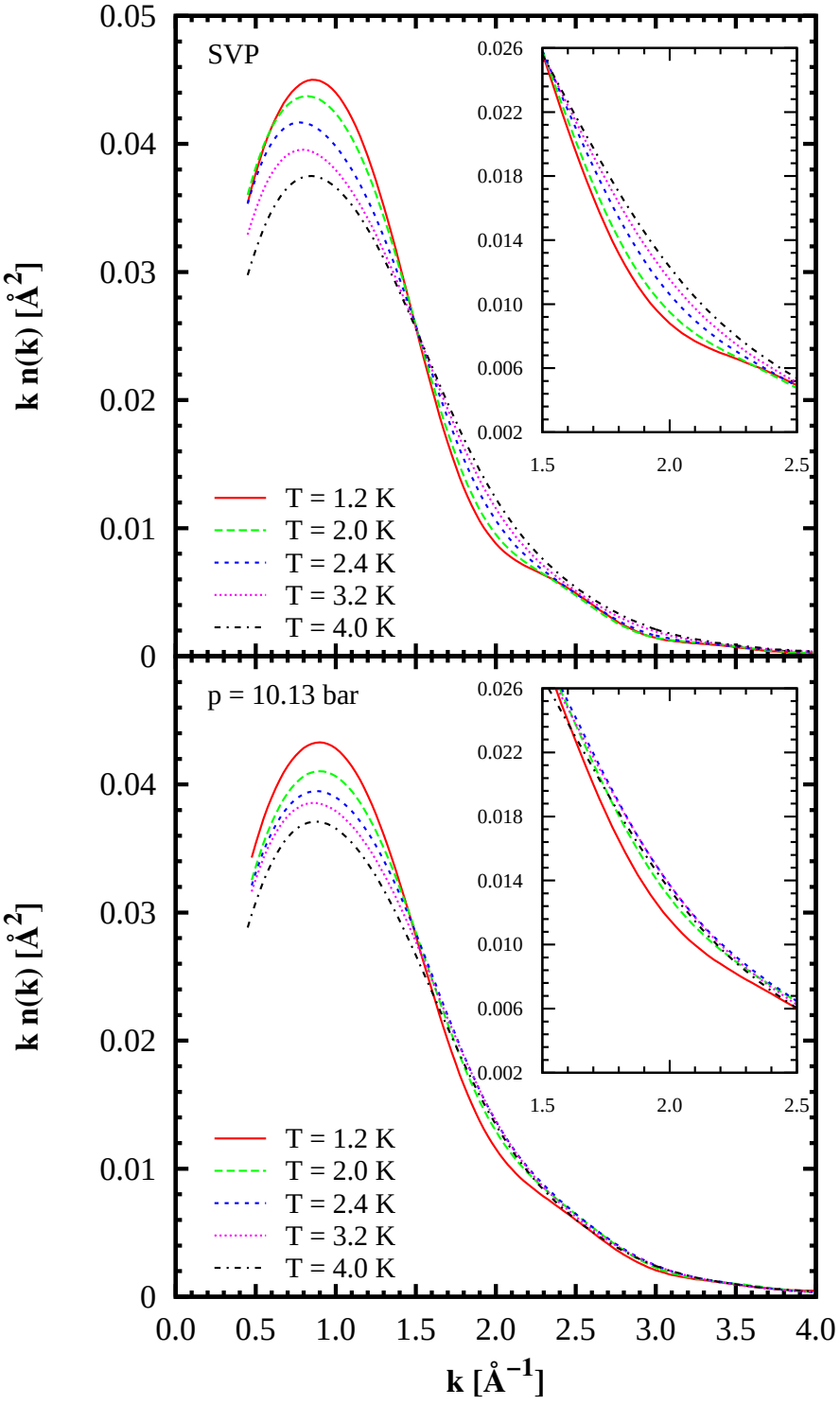

Fig. 5.17 The momentum distribution plotted as $kn(k)$ at two different pressures and temperatures. The insets show the same results but focused around $k \simeq 2$ Å^{-1}. *Top:* Results at saturated vapor pressure (SVP). *Bottom:* Results at a higher pressure $p = 10.13$ bar.

with the finite size of the system, $k_{\min} = 2\pi/L$, with L the length of any side of the cubic simulation box. Therefore, we are not able to show the $k \to 0$ behavior of the momentum distribution.

When T increases we see a progressive broadening of the distribution due to a *classical* thermal effect. However, in this evolution with T we can observe a non-trivial effect that appears at intermediate k values, $1.5 < k < 2.5$ Å^{-1}. As we show in Fig. 5.17, and in particular in the inset, there is a kink of $n(k)$ within this k range for temperatures smaller than T_λ, i.e., in the superfluid regime. As the temperature increases, and goes near the transition point, the kink becomes smoother, and it completely disappears for $T > T_\lambda$. We also notice that the kink is a bit more pronounced at SVP, when the intensity of the roton peak in the dynamic structure factor is larger (see Fig 5.18a). The location of this kink around $k \simeq 2$ Å^{-1} leads us to think that the kink can be related to the characteristic momentum of the roton excitation. It is known that the roton quasi-particle excitation is associated to the superfluidity of the system through the Landau criterium. In the normal phase, the roton disappears (Fig. 5.9) as a quasi-particle peak in the dynamic response $S(\boldsymbol{k}, \omega)$. Therefore, the connection between this kink in $n(k)$ and the roton excitation seems rather plausible.

In Fig. 5.18 (top panel), we show how the maximum height of the dynamic structure factor slowly decreases in the superfluid phase as we increase the temperature, until it experiences an abrupt drop once we enter the normal phase and then it remains constant. This is an expected result since the quasi-particle peak of the roton excitation disappears once we cross T_λ. Our data, reported in the figure, also show that the strength of the roton peak is slightly reduced when the pressure increases.

We can also look for the energy of the roton excitation, as well as the phonon and maxon excitations, and see how they evolve with temperature (see Fig. 5.18, bottom panel). In the superfluid phase, for the roton, the energy decreases as we increase the temperature. At higher temperatures, in the normal phase, it seems that the energy raises again, but one can not really speak about roton mode anymore due to the substantial broadening of its peak. As a matter of comparison, we report in Fig. 5.18 data obtained for the maxon and phonon energies. For the maxon excitation, the behavior is similar to the one of the roton, but in this case the strength of the peak when crossing T_λ is not so drastically reduced (Fig. 5.8). In the case of the phonon, the influence of the temperature is much smaller than in the previous cases.

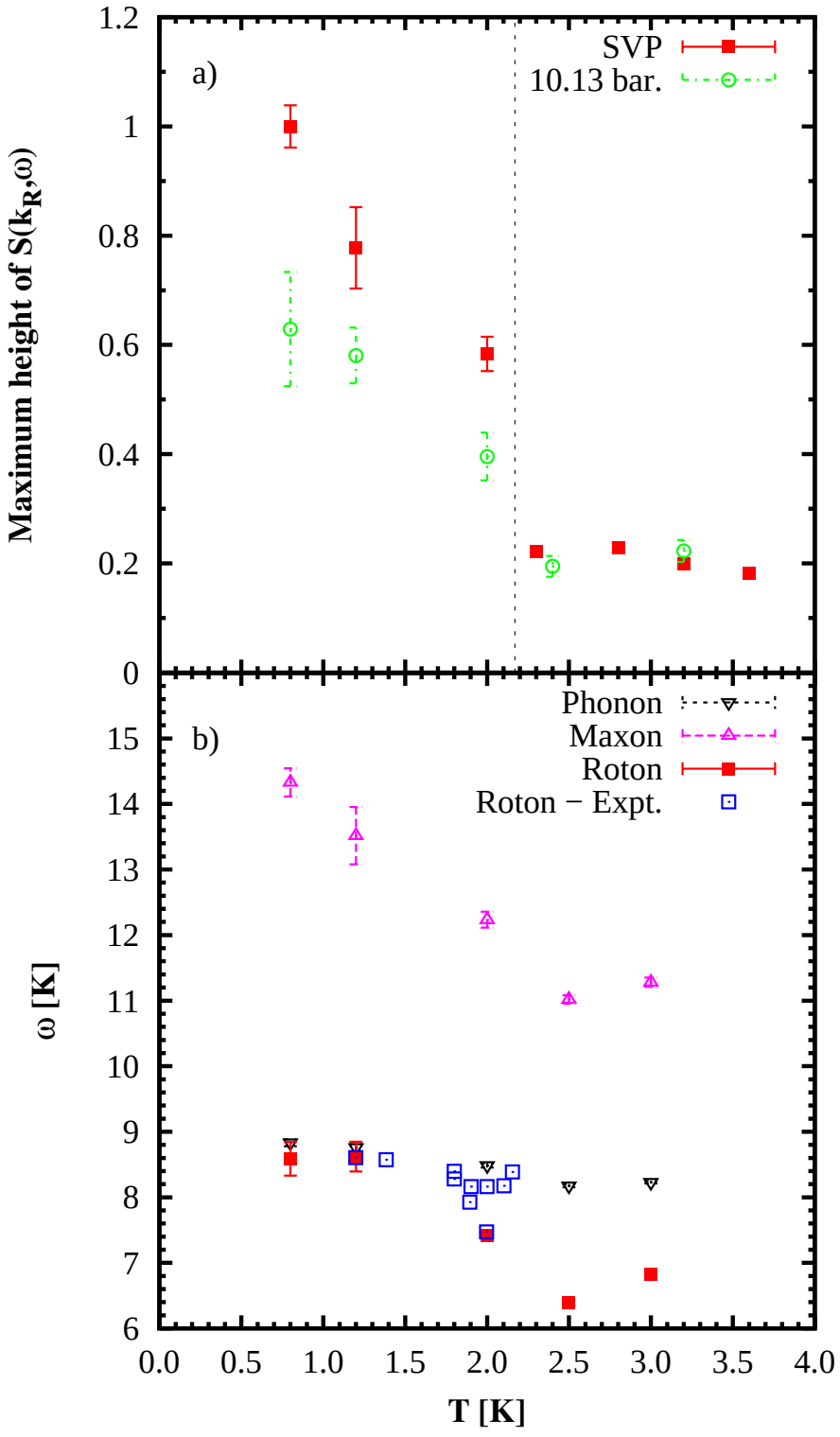

Fig. 5.18 *Top:* Maximum height of the dynamic structure factor $S(\boldsymbol{k}, \omega)$ of the roton ($k \sim 1.91$ Å^{-1}) across the normal-superfluid phase transition. All data are normalized by the maximum height at $T = 0.8$ K and SVP. *Bottom:* Temperature dependence of the phonon ($k \sim 0.43$ Å^{-1}), maxon ($k \sim 1.24$ Å^{-1}) and roton ($k \sim 1.91$ Å^{-1}) energy. Experimental results for the roton energy from Ref. [148]. In both figures k_R and ω_R are the momentum and the energy of the roton, respectively.

5.9 Summary

We have carried out PIMC calculations of liquid ^{4}He in a wide range of temperatures across the normal-superfluid transition T_λ to calculate the imaginary-time intermediate scattering function $F(q,\tau)$. From these functions one can in principle access to the dynamic response $S(q,\omega)$ through an inverse Laplace transform. But this is an ill-conditioned problem that can not be solved to deal with a unique solution. In recent works [135], it has been shown that the use of stochastic optimization tools can produce results with a richer structure than previous attempts relying on the maximum entropy method [131]. We have adopted here the well-known simulated annealing technique to extract the dynamic response, without any a priori bias in the search in order to get a result as unbiased as possible. In spite of the lack of any constraint in the cost function, we have verified that the three lowest energy-weighted sum rules are satisfactorily satisfied giving us some confidence on the reliability of our algorithm.

The results of the dynamic response are still not enough sharp in the quasiparticle peaks of the superfluid phase but the position of the peaks and the area below them are in nice agreement with experimental data. Interestingly, our results show clearly the signature of the transition in the roton peak, whose amplitude drops rapidly for $T > T_\lambda$. The effect of the temperature on the phonon-roton spectrum, static structure factor, and static response has been also studied.

The difficulties of extending correlated perturbative approaches to finite T have lead to a really unexplored dynamics of superfluid liquid ^{4}He, at least from a microscopic approach. With the present work, which can be considered an extension and improvement of a previous work based on the maximum entropy method [141], we have shown that the combination of PIMC and stochastic reconstruction is able to produce a satisfactory description of the quantum dynamics at finite temperature. We are also convinced that in the near future we can improve even more the present results. In this respect, one of the more promising avenues could be the estimation of complex-time correlation functions, instead of the merely imaginary ones, which can reduce the ill-posed character of the inversion problem due to its non-monotonic structure [136] (see chapter 6).

As for the study of the momentum distribution, our aim has been to determine the possible origin of the kink that $n(k)$ shows at k values around the roton momentum. This is not the first observation of this kink in theoretical calculations since it was already obtained more that twenty years ago [144]. The

location of the kink around the roton momentum led the idea of its relation with the roton but without further analysis. Now, we have shown that this scenario is more plausible because the kink vanishes when T_λ is crossed, mimicking the behavior of the roton quasi-particle peak.

Chapter 6

Sampling of complex-time correlation functions

In this chapter we present results of the sampling of complex-time correlation functions in multi-particle systems. The used method relies on the Path Integral Ground State (PIGS) formalism, but taking into consideration the time as a complex variable instead of as an imaginary one with a phase δ that acts as an adjustable parameter. This method already proved to produce good results for one-dimensional systems composed of only one particle [136]. The main goal of this approach is to be able to obtain better results for the dynamic structure factor $S(q, \omega)$ in multi-particle systems by reducing the ill-posed character of the inversion problem.

6.1 Introduction

As explained in the previous chapter, quantum Monte Carlo (QMC) methods simulate systems using imaginary-time dynamics. Therefore, we have no direct access to real-time evolution and thus we are not able to get the dynamic structure factor directly by a Fourier transform. Usually, this problem is solved by computing the intermediate scattering factor in imaginary time $F(q, \tau)$ and performing a numerical inversion of the Laplace transform, which gives us access to the dynamic structure factor. However, the ill-posed nature of this inversion makes difficult to recover a unique and well-defined solution. As we have shown in the previous chapter, the results obtained by these inversions provide a satisfactory description of the quantum dynamics at finite temperature, but fail to obtain a good description of high-energy contributions. In order to get more accurate results from quantum Monte Carlo data, it is necessary to develop new

estimators for the quantum correlation functions. This can be done by changing the kernel from the Laplace transform to a Lorentz one [138].

Recently, a work by Rota *et al.* [136] proposed the the estimation of complex-time correlation functions for the ground state using QMC methods in order to obtain a description of the dynamic structure factor. At finite temperature, the term $\exp(-\beta\hat{H})$ with $\beta = 1/T$ can be considered as an evolution operator in imaginary time, as explained in previous chapters (2.1). Thus, by rewriting imaginary-time correlation functions in complex time we can access to real-time correlation functions [154, 155]. These correlation functions in complex time can be calculated using the path-integral formalism [18] and estimated via QMC calculations [156]. Using this approach one can obtain significant improvements in the spectral functions over results obtained from imaginary-time correlation functions [157–164].

Despite the notion of complex time does not have a direct physical meaning at zero temperature, we can extend this formalism to the calculation of ground-state correlation functions. An adjustable parameter δ is introduced, which acts as a phase of a the complex time, $t_c = |t_c|e^{-i\delta}$. For $\delta = \pi/2$ our complex time will be fully imaginary, while for $\delta = 0$ it will be fully real. However, as one goes from $\delta = \pi/2$ to $\delta = 0$, the statistical errors become large, thus forcing us to use an optimal value of δ from which the estimated correlation functions present relevant information on the real dynamics of the system while maintaining moderate statistical errors. Also, the statistical error becomes larger by increasing $|t_c|$, thus the calculations are also only reliable up to a certain value of the complex time. This makes using high-order approximations for the quantum propagator extremely important [38]. However, Rota *et al.* proved that the Chin action (section 2.3.1) presents some problems in the estimation of complex-time correlation functions [136] due the chance of a positive term inside an exponential becoming exceedingly large. In their case, they used the propagator introduced by Zillich *et al.* [165], that proved to be suitable for this complex-time evolution.

Following the work of Rota *et al.* [136], we extend the calculation of complex-time correlation functions for the ground state to systems with more than one particle and with interparticle interactions. We want to analyze if the same methodology can be used in interacting systems, and if the statistical errors are controllable, within a value of δ, when the number of particles in the system increases.

6.2 Formalism

The general expression for a complex-time $t_c = t_m e^{-i\delta}$ correlation function at zero temperature is

$$C_{AB}(t_c) = \left\langle \Psi_0 | e^{it_c \hat{H}/\hbar} \hat{A} e^{-it_c \hat{H}/\hbar} \hat{B} | \Psi_0 \right\rangle \ , \tag{6.1}$$

where $\hat{H}$ is the Hamiltonian, Ψ_0 is the ground state wave-function and $\hat{A}$ and $\hat{B}$ are time-independent quantum operators corresponding to measurable observables. As we are mainly interested in the recovery of the dynamic structure factor, our complex-time correlation function of interest is the density-density correlation function.

$$S(\boldsymbol{q}, t_c) = \left\langle \Psi_0 | e^{it_c \hat{H}/\hbar} \hat{\rho}_{\boldsymbol{q}} e^{-it_c \hat{H}/\hbar} \hat{\rho}_{-\boldsymbol{q}} | \Psi_0 \right\rangle \ , \tag{6.2}$$

where $\hat{\rho}_{\boldsymbol{q}} = \sum_{i=1}^{N} e^{i\boldsymbol{q}\boldsymbol{r}_i}$ is the density-fluctuation operator as appears in equation 2.86. We can improve equation 6.2 in order to make it suitable for computer simulations:

$$\begin{aligned} S(\boldsymbol{q}, t_c) &= \int \mathrm{d}\boldsymbol{R}_0 \mathrm{d}\boldsymbol{R}_M e^{it_c E_0} \langle \Psi_0 | \boldsymbol{R}_M \rangle \left\langle \boldsymbol{R}_M | \hat{\rho}_{\boldsymbol{q}} e^{-it_c \hat{H}} \hat{\rho}_{-\boldsymbol{q}} | \boldsymbol{R}_0 \right\rangle \langle \boldsymbol{R}_0 | \Psi_0 \rangle \\ &= \mathcal{N} \int \mathrm{d}\boldsymbol{R}_0 \mathrm{d}\boldsymbol{R}_M \Psi_0^{\star}(\boldsymbol{R}_M) \rho_{\boldsymbol{q}}(\boldsymbol{R}_M) G(\boldsymbol{R}_0, \boldsymbol{R}_M; t_c) \rho_{-\boldsymbol{q}}(\boldsymbol{R}_0) \Psi_0(\boldsymbol{R}_0) \ , \end{aligned} \tag{6.3}$$

where $\mathcal{N}$ is a normalization constant, and $G(\boldsymbol{R}_0, \boldsymbol{R}_M; t_c) = \left\langle \boldsymbol{R}_M | e^{-it_c \hat{H}} | \boldsymbol{R}_0 \right\rangle$ is the propagator from a configuration $\boldsymbol{R}_0$ to $\boldsymbol{R}_M$ in a complex time t_c. In the general case, $G(\boldsymbol{R}_0, \boldsymbol{R}_M; t_c)$ only becomes real and positive when $\delta = \pi/2$, meaning t_c is purely imaginary-time. This means that we can not use $G(\boldsymbol{R}_0, \boldsymbol{R}_M; t_c)$ as a probability distribution for the sampling of our PIGS coordinates as it is usually done. However, we can sample the configurations $\boldsymbol{R}_0$ and $\boldsymbol{R}_M$ normally using standard imaginary-time PIGS method, and then calculate $S(\boldsymbol{q}, t_c)$ by estimating the quantity $\rho_{\boldsymbol{q}}(\boldsymbol{R}_M) G(\boldsymbol{R}_0, \boldsymbol{R}_M; t_c) \rho_{-\boldsymbol{q}}(\boldsymbol{R}_0)$.

In general, the exact form for the Green's function $G(\boldsymbol{R}_0, \boldsymbol{R}_M; t_c)$ is unknown. Being able to construct accurate approximations in the limit of small time $t_m = |t_c|$, we can estimate it for larger values of t_m using path-integral formalism and rewriting $G(\boldsymbol{R}_0, \boldsymbol{R}_M; t_c)$ as a convolution of M propagators of shorter time $\tau_c = t_c/M$,

$$G(\boldsymbol{R}_0, \boldsymbol{R}_M; t_c) = \int \mathrm{d}\boldsymbol{R}_1 \ldots \mathrm{d}\boldsymbol{R}_{M-1} \prod_{\alpha=1}^{M} G(\boldsymbol{R}_\alpha, \boldsymbol{R}_{\alpha-1}; \tau_c) \ . \tag{6.4}$$

Following this approach, we need to sample all the configurations $\boldsymbol{R}_1, \boldsymbol{R}_2, \ldots \boldsymbol{R}_{M-1}$, meaning that we need to build paths between the configurations $\boldsymbol{R}_0$ and $\boldsymbol{R}_M$ obtained via standard PIGS method. In order to sample these paths, we can use importance sampling using a certain probability $p_{path}(\boldsymbol{R}_0, \boldsymbol{R}_1, \ldots \boldsymbol{R}_M)$. The simplest option for this implementation is to make use of M free propagators with time-step τ_s, resulting in

$$p_{path}(\boldsymbol{R}_0, \boldsymbol{R}_1, \ldots \boldsymbol{R}_M) = \prod_{\alpha=1}^{M} G_{free}(\boldsymbol{R}_\alpha, \boldsymbol{R}_{\alpha-1}; \tau_s) \ , \tag{6.5}$$

where

$$G_{free}(\boldsymbol{R}_\alpha, \boldsymbol{R}_{\alpha-1}; \tau_s) = (4\pi\lambda\tau_s)^{dN/2} \exp\left(-\frac{(\boldsymbol{R}_\alpha - \boldsymbol{R}_{\alpha-1})^2}{4\lambda\tau_s}\right) \ , \tag{6.6}$$

is the Green's function of the free propagator, with N is the number of particles, d is the dimensionality of the system, and $\lambda = \hbar^2/2m$.

In general, this method for sampling the configurations $\boldsymbol{R}_1, \boldsymbol{R}_2, \ldots \boldsymbol{R}_{M-1}$ works well for quantum systems interacting with a smooth potential. In these cases, the variance for the complex-time estimators (Eq. 6.1) is reduced when the imaginary time of the free propagator τ_s is similar to the modulus of the kinetic propagator in complex time $|\tau_c| = \tau_m$. Another option for the sampling of the paths is to use the staging algorithm (section 2.4.1), whose probability distribution follows

$$\begin{aligned} p_{path}(\boldsymbol{R}_0, \boldsymbol{R}_1, \ldots \boldsymbol{R}_M) = &\left(\frac{m}{2\pi\hbar^2 M\tau_s}\right)^{dN/2} \exp\left(-\frac{m}{2\hbar^2 M\tau_s}(\boldsymbol{R}_M - \boldsymbol{R}_0)^2\right) \times \\ &\times \prod_{\alpha=1}^{M-2} \left(\frac{m_\alpha}{2\pi\hbar^2\tau_s}\right)^{dN/2} \exp\left(-\frac{m_\alpha}{2\hbar^2\tau_s}(\boldsymbol{R}_{\alpha+1} - \boldsymbol{R}^*_{\alpha+1})^2\right) \ , \end{aligned} \tag{6.7}$$

with $m_\alpha = m\frac{M-\alpha}{M-\alpha-1}$ and $\boldsymbol{R}^*_{\alpha+1} = \frac{\boldsymbol{R}_M + \boldsymbol{R}_\alpha(M-\alpha-1)}{M-\alpha}$.

With $p_{path}(\boldsymbol{R}_0, \boldsymbol{R}_1, \ldots \boldsymbol{R}_M)$, the expression for the estimator of the density-density correlation becomes

$$\begin{aligned} S(\boldsymbol{q}, t_c) = \mathcal{N}^* \int \mathrm{d}\boldsymbol{R}_0 \ldots \mathrm{d}\boldsymbol{R}_M \rho_{\boldsymbol{q}}(\boldsymbol{R}_M) \frac{\prod_{\alpha=1}^{M} G(\boldsymbol{R}_\alpha, \boldsymbol{R}_{\alpha-1}; \tau_c)}{p_{path}(\boldsymbol{R}_0, \boldsymbol{R}_1, \ldots \boldsymbol{R}_M)} \rho_{-\boldsymbol{q}}(\boldsymbol{R}_0) \times \\ \times \Psi_0(\boldsymbol{R}_M) p_{path}(\boldsymbol{R}_0, \boldsymbol{R}_1, \ldots \boldsymbol{R}_M) \Psi_0(\boldsymbol{R}_0) \ . \end{aligned} \tag{6.8}$$

The normalization factor $\mathcal{N}^*$ can be estimated considering that, for $\boldsymbol{q} = 0$, the density-density correlation is $S(0, t_c) = \langle \Psi_0 | \Psi_0 \rangle = 1$. Therefore, we can define

the value

$$O_A(\boldsymbol{R}_0 \dots \boldsymbol{R}_M) = \frac{\prod_{\alpha=1}^{M} G_A(\boldsymbol{R}_\alpha, \boldsymbol{R}_{\alpha-1}; \tau_c)}{p_{path}(\boldsymbol{R}_0, \boldsymbol{R}_1, \dots \boldsymbol{R}_M)} \ , \tag{6.9}$$

where $G_A(\boldsymbol{R}_\alpha, \boldsymbol{R}_{\alpha-1}; \tau_c)$ is an approximation for the complex-time propagator. Using this, we can write equation 6.8 as

$$S(\boldsymbol{q}, t_c) = \frac{\langle \hat{\rho}_{\boldsymbol{q}} O_A(\boldsymbol{R}_0 \dots \boldsymbol{R}_M) \hat{\rho}_{-\boldsymbol{q}} \rangle}{\langle O_A(\boldsymbol{R}_0 \dots \boldsymbol{R}_M) \rangle} \ . \tag{6.10}$$

In order to further simplify this equation to get an expression suited to be implemented in a simulation, we need to choose an approximation for $G(\boldsymbol{R}_\alpha, \boldsymbol{R}_{\alpha+1}; \tau_c)$. As happens for a standard PIMC scheme, the exact correlation function will be obtainable by increasing the number of convolution terms M. However, every propagator introduces an oscillating phase term, meaning that with a large value of M the increase in statistical noise is significant. As was commented in previous sections (2.3), it is important to use good approximations in order to keep the number of convolution terms M at minimum and yet recover the converged correlation function.

The simplest approximation applicable is the primitive approximation, as appeared in section 2.3, that in this case is factorized as $e^{it_c\hat{H}} \simeq e^{it_c\hat{K}} e^{it_c\hat{V}}$. With this approximation, the complex-time propagator is written as

$$\begin{aligned} G_{PA}(\boldsymbol{R}_\alpha, \boldsymbol{R}_{\alpha-1}; \tau_c) = \exp\left(-\frac{(\boldsymbol{R}_\alpha - \boldsymbol{R}_{\alpha-1})^2}{4\lambda i \tau_c}\right) \times \\ \times \exp\left(-i\frac{V(\boldsymbol{R}_\alpha) + V(\boldsymbol{R}_{\alpha-1})}{2\hbar}\tau_c\right) \ . \end{aligned} \tag{6.11}$$

As commented before, in this case the variance of the complex-time estimators will be reduced when $\tau_m = t_m/M \simeq \tau_s \sin(\delta)$. As happens in the standard PIMC scheme, the Primitive Approximation is easy to implement but requires a large number of convolution terms in order to converge to the exact result. However, using high-order approximations with double commutator terms could not be convenient in this case, as explained by Rota [136], since for a certain value of δ, the double commutator term could appear with a positive sign, producing largely increasing amplitudes and making the results unreliable.

Still, we could use high-order approximations without the double commutator term. In this sense, we can use linear combinations of different symplectic expansions, as presented by Zillich *et al.* [165]. Some of the coefficients of such linear combination are negative, which present a drawback when used in a conventional PIMC scheme, since the approximation of the imaginary-time propa-

gator will not be positive definite. However, this does not represent a problem here, since the complex propagator is used as an estimator instead of a probability distribution. These combinations are constructed from a basis second-order propagator

$$G_{PA}(\boldsymbol{R}_\alpha, \boldsymbol{R}_{\alpha-1}; \tau_c) = e^{-\tau_c \hat{V}/2} e^{-\tau_c \hat{T}} e^{-\tau_c \hat{V}/2} \tag{6.12}$$

from which are derived combinations of higher-order propagators. In our case, we will use fourth-order

$$G_4(\boldsymbol{R}_\alpha, \boldsymbol{R}_{\alpha-1}; \tau_c) = -\frac{1}{3} G_{PA}(\boldsymbol{R}_\alpha, \boldsymbol{R}_{\alpha-1}; \tau_c) + \frac{4}{3} G_{PA}^2\left(\boldsymbol{R}_\alpha, \boldsymbol{R}_{\alpha-1}; \frac{\tau_c}{2}\right) \tag{6.13}$$

and sixth-order propagators,

$$\begin{aligned} G_6(\boldsymbol{R}_\alpha, \boldsymbol{R}_{\alpha-1}; \tau_c) = \frac{1}{45} G_{PA}(\boldsymbol{R}_\alpha, \boldsymbol{R}_{\alpha-1}; \tau_c) - \frac{4}{9} G_{PA}^2\left(\boldsymbol{R}_\alpha, \boldsymbol{R}_{\alpha-1}; \frac{\tau_c}{2}\right) \\ + \frac{64}{45} G_{PA}^4\left(\boldsymbol{R}_\alpha, \boldsymbol{R}_{\alpha-1}; \frac{\tau_c}{4}\right) \ . \end{aligned} \tag{6.14}$$

Once we have obtained data for the density-density correlation function, we can recover the dynamic structure factor $S(\boldsymbol{q}, \omega)$ by inverting the integral transform

$$S(\boldsymbol{q}, t_c) = \int \mathrm{d}\omega \, e^{-i t_c \omega} S(\boldsymbol{q}, \omega) \ , \tag{6.15}$$

as done by Rota *et al.* [136] for one-particle systems. Both $S(\boldsymbol{q}, t_c)$ and $S(\boldsymbol{q}, \omega)$ are evaluated over a finite set of complex times $(t_c)_i$ and frequencies ω_j respectively. We can equation 6.15 as a linear equation

$$y = Ax \ , \tag{6.16}$$

where y represents the data from the density-density correlation function $S(\boldsymbol{q}, t_c)$, x is the data for the dynamic structure factor $S(\boldsymbol{q}, \omega)$ that we aim to obtain, and A is a matrix defined from the kernel of the integral transform from equation 6.15. The best least-squares solution to equation 6.16 is

$$x = A^T (A A^T)^{-1} y \ , \tag{6.17}$$

that works well for well-posed problems. As happened in chapter 5, we are facing an ill-posed problem due to the statistical noise of the $S(\boldsymbol{q}, t_c)$, unavoidable for any QMC calculation, being uncontrollably magnified in the inversion process, and thus not recovering acceptable results for $S(\boldsymbol{q}, \omega)$.

In order to solve that, we introduce a well-conditioned linear operator C_a depending on a regularization parameter $a > 0$ that approaches $A^T(AA^T)^{-1}$ in the limit of $a \to 0$. The solution of the original problem will then be $x = \lim_{a\to 0} C_a y$. In this case, we have chose the Tikhonov regularization [137], with the form

$$C_a = A^T(AA^T + Ia^2)^{-1} \ , \tag{6.18}$$

where I is the identity matrix. Also, since the physical solution must verify $x_i \geq 0$ since $S(\boldsymbol{q}, \omega) \geq 0$, we introduce this requirement explicitly as a diagonal matrix $Q = \mathrm{Diag}(q_1, \ldots, q_N)$, where each q_i is a factor restricted to 0 or 1. Finally, the solution can be written as

$$x = QA^T(AQA^T + Ia^2)^{-1}y \ , \tag{6.19}$$

and satisfies $x_i = 0$ if $q_i = 0$ and $y = Ax$, irrespective of Q.

6.3 Results for a model one-particle system

We applied the formalism introduced in the previous section to the simple case of a single particle in a one-dimensional harmonic potential. For this case, the exact result for the density-density correlation function is known [166],

$$S\left(q, t_c\right) = \exp[\frac{q^2}{2}\left(e^{-it_c} - 1\right)] \tag{6.20}$$

In order to apply the formalism explained in the previous section, we proceed as follows: we perform a standard PIGS simulation and we make sure to reach the ground state through thermalization. Then, we abilitate the sampling movements of the *worm* algorithm, choosing the only particle of the system as the worm, to move the system to the ensamble G. Once the system is in off-diagonal configurations, we forbid the movements to return to the ensamble Z. While in off-diagonal configurations, we construct the paths following equation 6.7 by using the chosen complex time propagator. These paths are only reconstructed to compute the density-density correlation function (Eq. 6.8), and are not taken into account in the movement proposals of the PIGS algorithm. That means that we need to reconstruct the paths each time we perform a calculation, and differents paths need to be constructed for different number of *beads* M and values of t_m.

By having the exact result we can test the correctness of our results, as well as the maximum time t_m we can reach. This calculation was also done by Rota

et al. [136], and it showed that the Primitive Approximation is only accurate at short times. They also performed a calculation using the Chin Approximation that, despite behaving better than the Primitive Approximation, still falls short in recovering high time correlations when compared with the Zillich sixth-order expansion (Eq. 6.14).

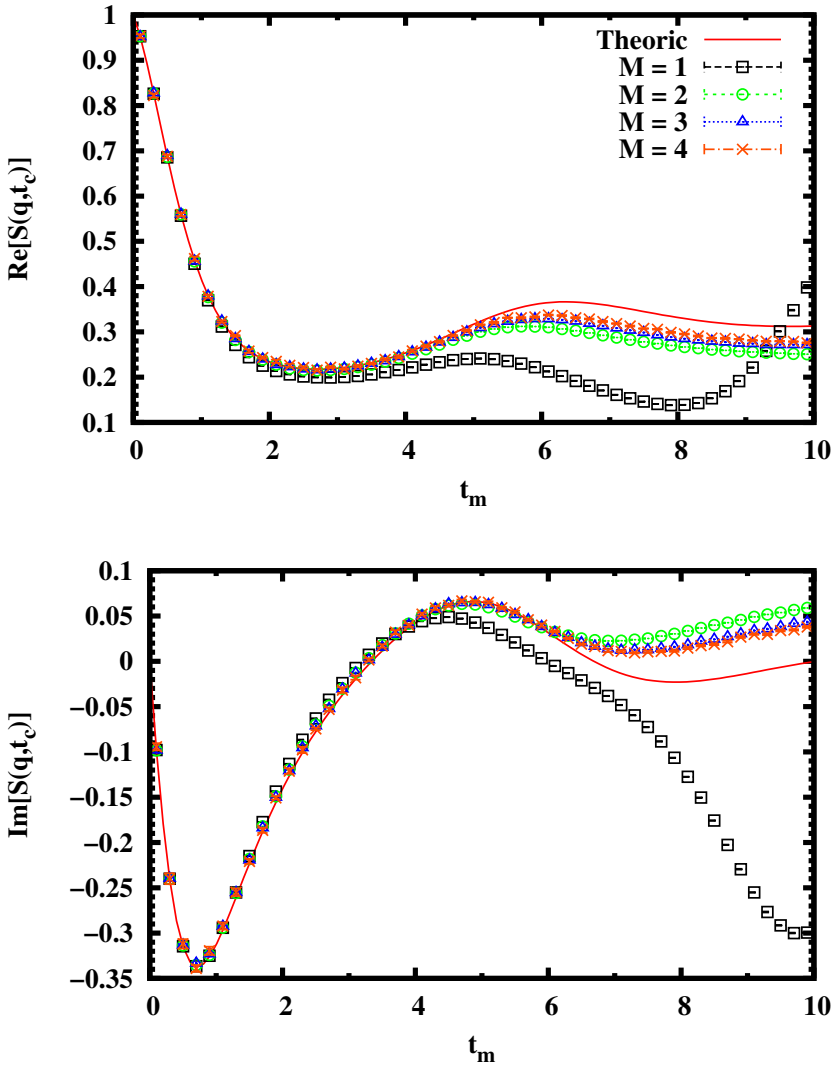

Fig. 6.1 Real (top) and imaginary (bottom) parts of the $S(q, t_c)$ results for one particle in a one-dimensional harmonic potential as a function of t_m, for a value of $q = 1.5$ and $\delta = \pi/9$. The solid line stands for the exact result from equation 6.20. The results are calculated with different number of *beads* M of the Zillich sixth-order expansion (Eq. 6.14)

.

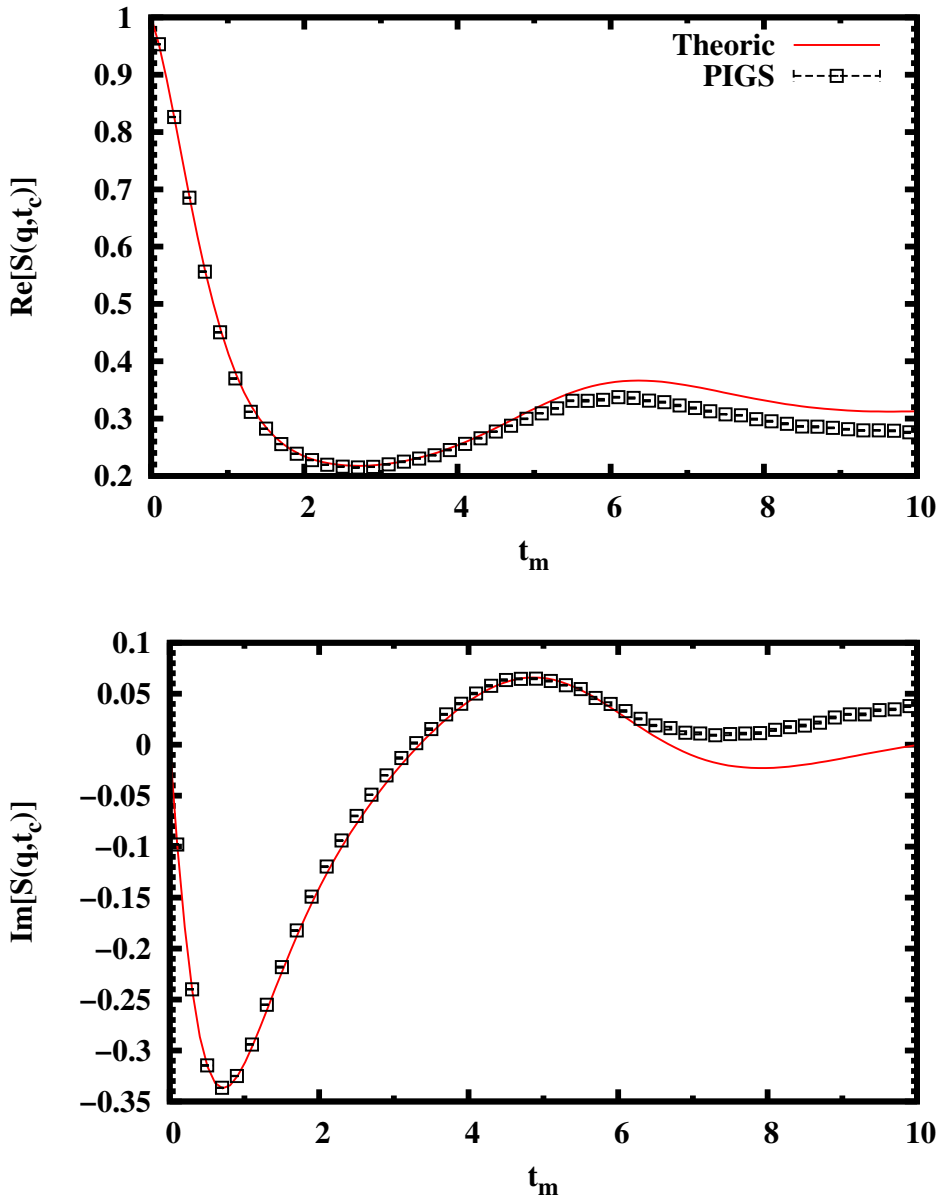

Fig. 6.2 Real (top) and imaginary (bottom) parts of the $S(q, t_c)$ results for one particle in a one-dimensional harmonic potential as a function of t_m, for a value of $q = 1.5$ and $\delta = \pi/9$. The solid line stands for the exact result from equation 6.20. The results are calculated with different number of *beads* M, and they are put together by selecting the best results for a certain time interval

.

In figure 6.1 we show the results obtained for $q = 1.5$ and $\delta = \pi/9$, as well as the exact value obtained via equation 6.20. The results are computed using different numbers of *beads* M. A higher value of M means a longer path to be sampled following equation 6.7, so this will yield an increased variance over all

the time range when compared with results with less *beads*. However, increasing the value of M is necessary in order to achieve results closer to the exact values. This can be seen clearly at $t_m > 4$ in the figure 6.20, where the results with $M = 1$ clearly diverge from the exact result despite having less variance. In the end, this increased variance can be reduced by running a longer simulation. However, as can be seen, reaching the exact result at high times $t_m > 6$ its difficult, and will require a higher number of *beads*.

In equation 6.2 we have put all the results together in order to obtain a single result for the density-density correlation function to be able to perform the inversion. At lower time t_m we choose the results for small number of *beads*, since they have lower variance. As can be seen, at $t_m \simeq 2$ the results for $M = 1$ diverge from the results at higher M. From this value of t_m up we choose the results for $M = 2$, and so on.

6.4 Results for a model multi-particle interacting system

In the previous section we have shown the results obtained for a single particle in a one-dimensional potential. The goal of this section is to extrapolate the same formalism to many-particle interacting systems, and to see if the maximum time t_m we can reach with a reasonable number of *beads* M decreases significantly when increasing the number of particles. In this sense, we have chosen a one-dimensional system of particles interacting via a harmonic potential.

We need to apply some changes in the PIGS algorithm in order to work with more than one particle. As the reconstruction needs to be made at the ground state Ψ_0, we need to open all the polymers as if all of them are the worm. We proceed as for one-particle system, by first reaching the ground state and then opening all the polymers. Then, we proceed to the sampling of the system and performing estimations after a certain number of steps.

However, a problem arises in this system when opening all the polymers. Since we are not under periodic boundary conditions, both halfs of the opened polymers can drift away from each other since, when proposing a staging movement, they only feel the presence of the *beads* of the same index from other particles. This can result in having two drops far away from each other, each composed by the same-numbered halfs of the particles. In order to avoid this, we introduce an external harmonic potential applied to each *bead* as $\gamma/2(\sum_{i=1}^{N} x_{\alpha,i})^2$, with γ being a parameter. For $\gamma = 1/N$ we can perform a change of variable

in order to uncouple the oscillators, allowing us to recover the exact energy and density-density correlation function.

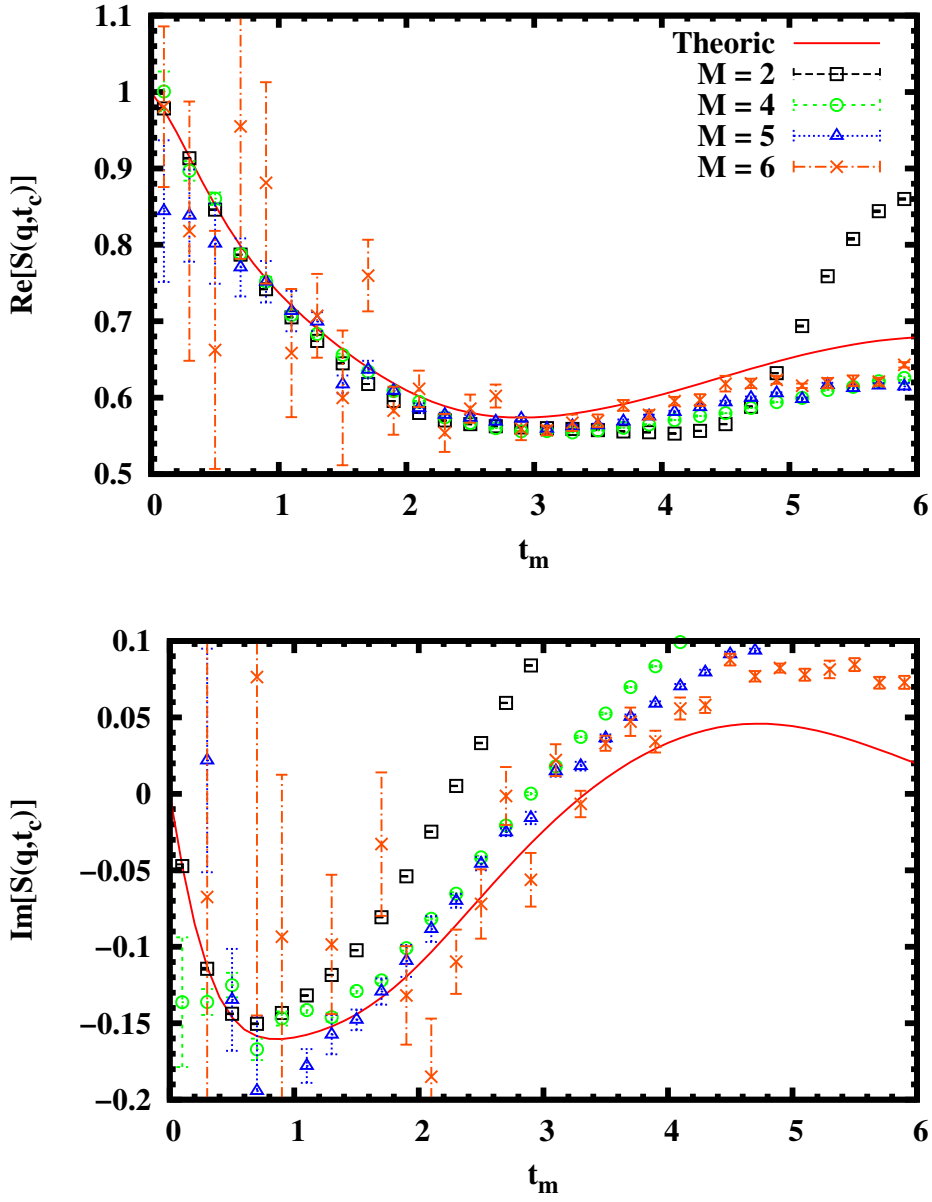

Fig. 6.3 Real (top) and imaginary (bottom) parts of the $S(q, t_c)$ results for a system with $N = 3$ interacting particles as a function of t_m, for a value of $q = 1.5$ and $\delta = \pi/9$. The solid line stands for the exact result computed numerically. The results are calculated with different number of *beads* M of the Zillich fourth-order expansion (Eq. 6.13)

.

It is important to note that the path constructions can be done between any pair of particles, and in fact one must take into account all the possible pairs when computing equation 6.10. The number of pairs increases with the number of particles N as $N!$, making it unpractical with systems with a high number of particles. To solve this, we perform calculations with $N = 3$ and $N = 4$ taking into account all the pairs, and by choosing only N pairs randomly. The results are strictly the same, despite taking into account all the pairs yields less variance for the sole fact that we accumulate more statistics.

Another important fact of the path construction is that equation 6.7 does not take into account the other paths, meaning that some paths may fall pretty close or far from each other. Taking all that into account, we performed calculations using sixth-order Zillich action for the density-density correlation function. However, we found some unexpected behaviour in the function obtained, as for a certain phase δ and number of *beads* M we found a divergence in a certain time t_m. As this divergence dissappears when increasing M, we supect it could arise from the term $G_{PA}(\boldsymbol{R}_\alpha, \boldsymbol{R}_{\alpha-1}; \tau_c)$ in equation 6.14 being too inaccurate. To avoid this divergence, we switch the used propagator to equation 6.13, which is a fourth-order approximation.

In figure 6.3 we show the result with different number of *beads* for a system composed by $N = 3$ particles. We can see clearly how the variance has increased when comparing this results with the ones obtained at the same angle $\delta = \pi/9$ for one particle (Figure 6.1). For low number of *beads* we recover the expected theoretical result at low time scale. On the other hand, results with the highest value of M show large variance at low time-scales while it decreases at high t_m. We can expect to recover the exact value, given a higher number of *beads* and long enough simulation time. In the figure 6.4 we can see the results for the different number of *beads* put together, as with the one-dimensional case. Despite having a large degree of variance overall the time range, the obtained results become acceptable by running longer simulations.

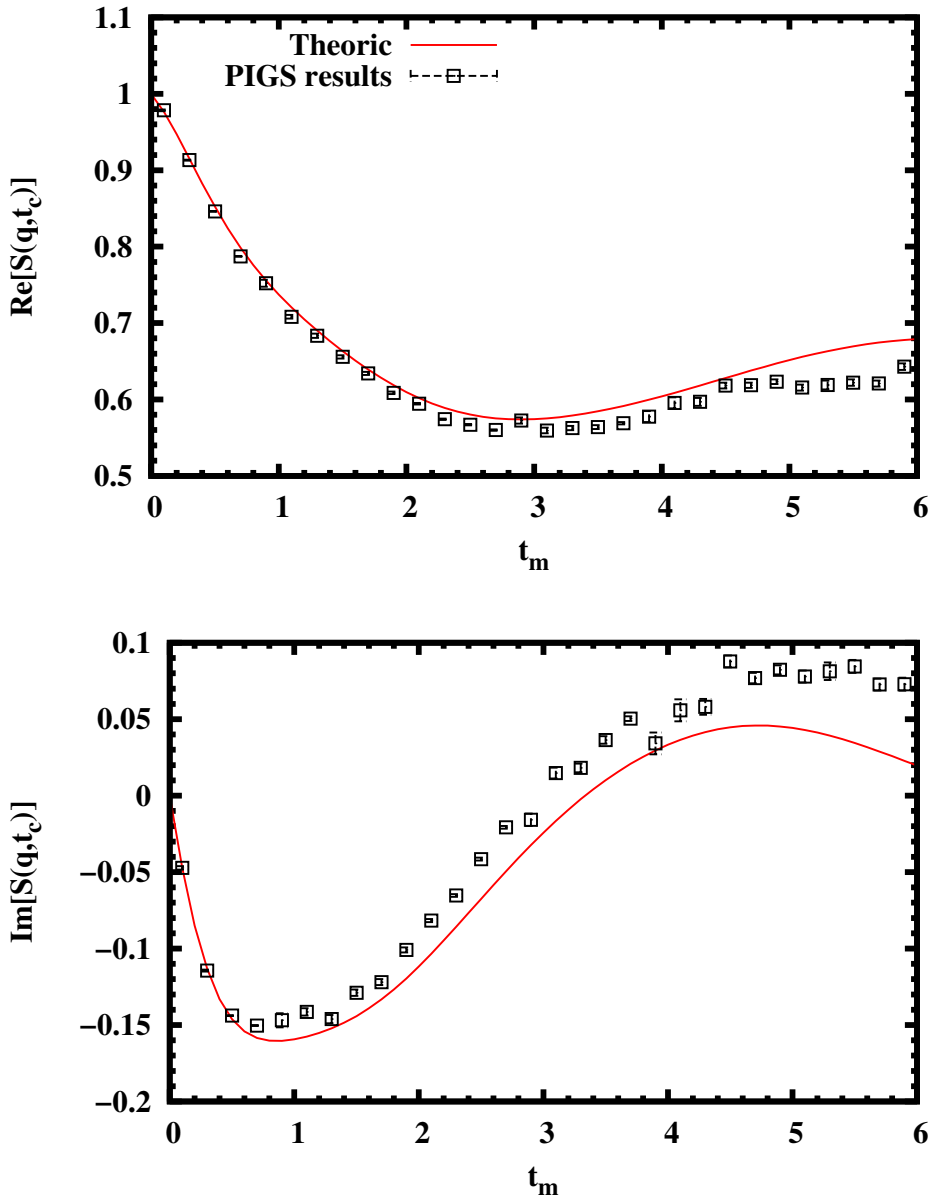

Fig. 6.4 Real (top) and imaginary (bottom) parts of the $S(q, t_c)$ results for a system with $N = 3$ interacting particles as a function of t_m, for a value of $q = 1.5$ and $\delta = \pi/9$. The solid line stands for the exact result computed numerically. The results are calculated with different number of *beads* M, and they are put together by selecting the best results for a certain time interval

.

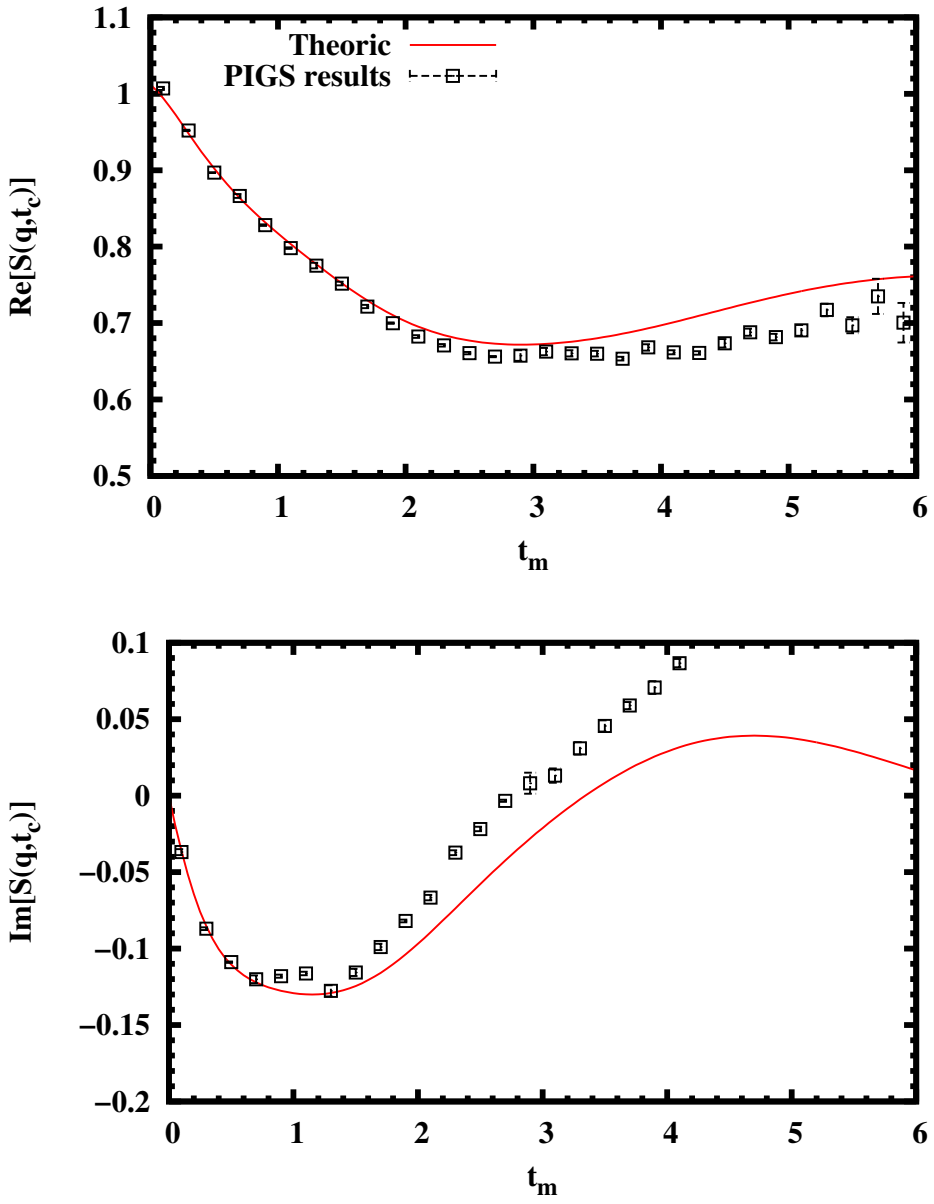

Fig. 6.5 Real (top) and imaginary (bottom) parts of the $S(q, t_c)$ results for a system with $N = 4$ interacting particles as a function of t_m, for a value of $q = 1.5$ and $\delta = \pi/9$. The solid line stands for the exact result computed numerically. The results are calculated with different number of *beads* M, and they are put together by selecting the best results for a certain time interval

.

We do the same for $N = 4$ particles. In figure 6.5 we show the results for different number of *beads*. Both results for $N = 3$ and $N = 4$ are obtained with the same number of sampling steps, but when comparing figure 6.4 and 6.5 we can see how the results obtained for $N = 4$ are in less accordance with the

theoretical ones than the results for $N = 3$. Also, we can see how we have more difficulties recovering the imaginary part of the complex time density-density correlation function. Despite the results being improved by longer simulation times or a higher number of *beads*, the cost of the simulation step increases with the number of particles and *beads*, meaning that with a number of particles closer to the typical PIMC simulation (i.e. $N = 64$) it could become extremely demanding to recover results good enough to perform the inversion.

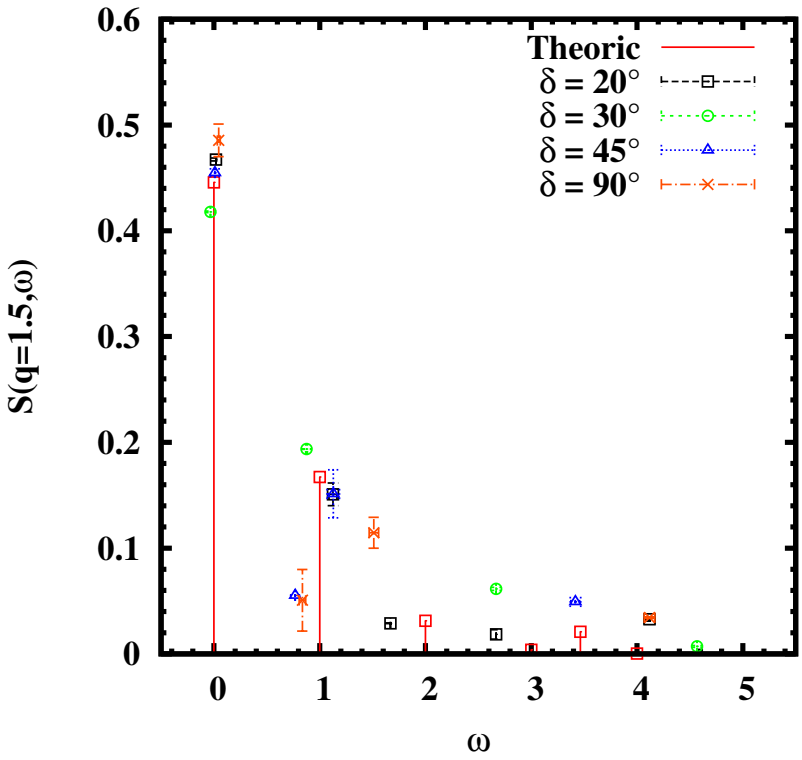

Fig. 6.6 Dynamic structure factor $S(q, \omega)$ for a system with $N = 3$ interacting particles at $q = 1.5$. The impulse red lines correspond to the exact value, while the others correspond to the results derived from QMC via the inversion method explained above, for different values of δ

.

In figure 6.6 we show the exact results for the dynamic structure factor $S(q, \omega)$ for $N = 3$ particles with the ones obtained using the inversion method explained in section 6.2 for different values of δ. The exact results are plotted with vertical lines as the exact value is defined by a set of delta functions.

For one-particle systems, the work by Rota *et al.* [136] proved that reducing the value of the phase δ provided with results closer to the exact values. In our case, the same seems to apply since for low values of δ we recover results for high transition lines that are not recovered at higher values. However, the precision of such results is not as good as for the one-particle systems, probably because the density-density correlation function has higher variance.

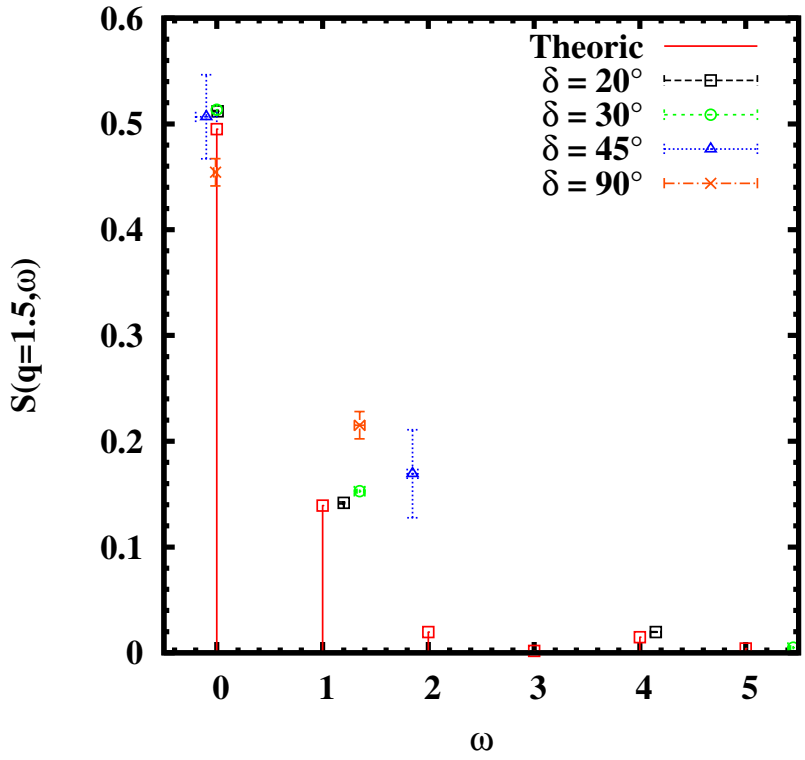

Fig. 6.7 Dynamic structure factor $S(q,\omega)$ for a system with $N = 4$ interacting particles at $q = 1.5$. The impulse red lines correspond to the exact value, while the others correspond to the results derived from QMC via the inversion method explained above, for different values of δ

.

The same can be done by $N = 4$, as shown in figure 6.7. In this case we see more clearly how the results at a high value of δ, mainly $\delta = 90°$ and $\delta = 45°$ provide a poor approximation to the exact value, since the inversion for these phases only recovers the initial delta at $\omega = 0$, and then a value with high variance between 1 and 2. For $\delta = 30°$ and $\delta = 20°$ we obtain the value at $\omega = 1$ with good enough precision. We may fail to recover some of the high-

transition deltas, but we achieved some results at high values of ω that go with good accordance with the exact values of $S(q = 1.5, \omega)$.

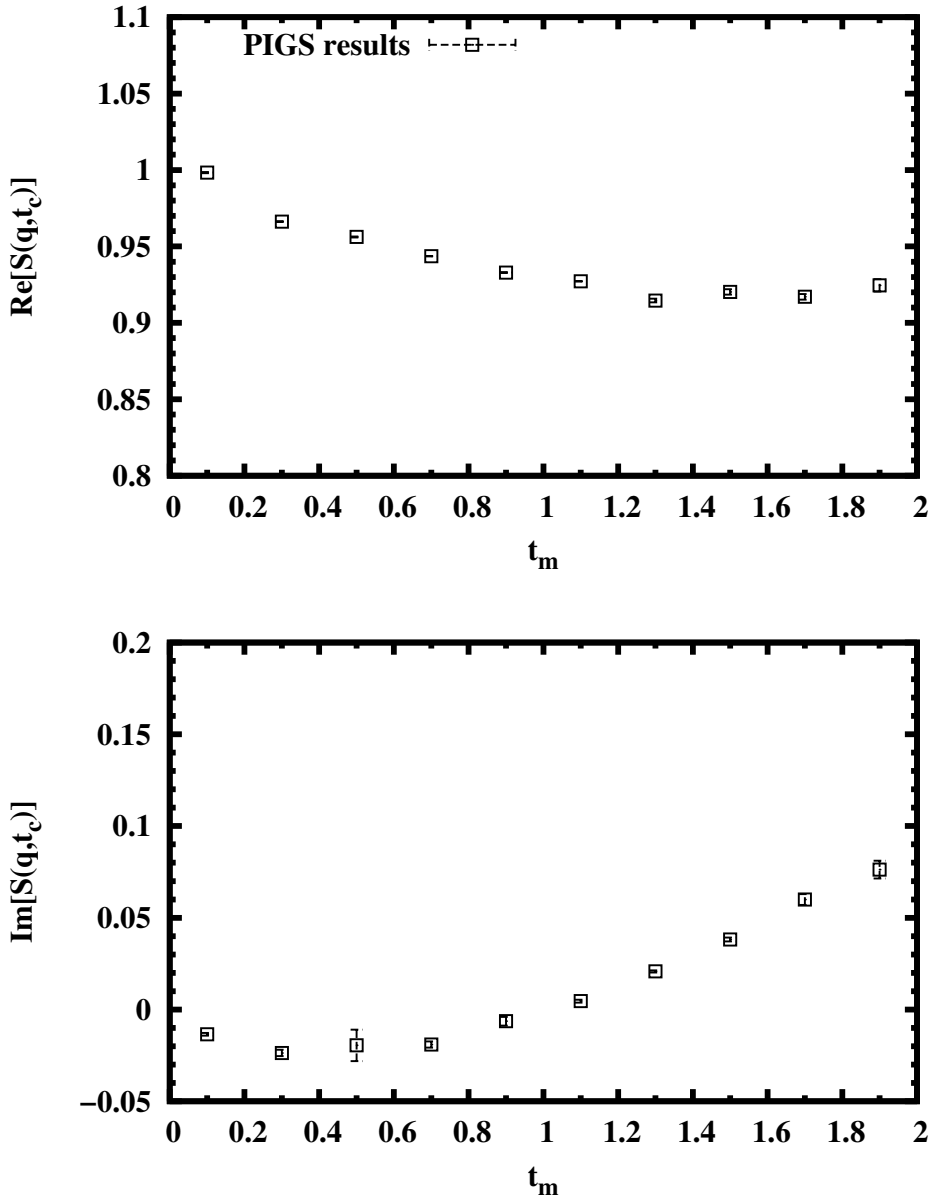

Fig. 6.8 Real (top) and imaginary (bottom) parts of the $S(q, t_c)$ results for a system with $N = 10$ interacting particles as a function of t_m, for a value of $q = 1.5$ and $\delta = \pi/6$. The results are calculated with different number of *beads* M, and they are put together by selecting the best results for a certain time interval

.

It is clear that using the information provided by the complex-time correlation function improves the dynamic structure function obtained via inversion, despite the ill-posed nature of the problem. With this concluded, as our final objective is to extend this formalism to real systems such as ^{4}He, we need to check if by increasing the number of particles by a great number the noise of the density-density correlation function still holds acceptable values. He have performed calculations of the density-density correlation function for a system with $N = 10$ particles, as shown in the figure 6.8. The time window has been reduced tu $t_m = 2$, since for higher times the variance of the results increases drastically. For the time window chosen, the results behave with an acceptable variance. Apart for the computational cost increasing intrinsically with the number of particles, for $N = 10$ we needed to perform a longer simulation run in order to reduce the variance of the chosen time interval.

In the end, applying this method for obtaining the dynamic structure factor to real systems with a larger number of particles seems feasible, despite the computation time needed to be large in order to reduce the variance to a values acceptable enough in order to perform the inversion.

6.5 Summary

We have extended the calculation of complex-time correlation functions, specifically the density-density correlation function, previously studied in the work of Rota *et al.* [136] to multi-particle systems interacting with an harmonic potential. The results obtained for the density-density correlation function in complex time show a higher variance that the ones obtained for one-particle systems, but still are in a good enough accordance with the exact values. By solving the inversion problem, we obtain the dynamic structure factor for such systems, that clearly benefits for the parameter δ, thus obtaining better results for a low value of δ, near the pure real time, as happens for the one-particle system. The results for the density-density correlation function for a higher number of particles show that, despite the cost of the sampling rising, it is possible to obtain good results within a certain time window.

In further works we intend to apply the used method to real systems such as ^{4}He, in order to improve the currently obtained results for the dynamic structure factor using pure imaginary-time correlation functions.

Chapter 7

Conclusions

Along this Thesis, we have performed numerical simulations on relevant quantum fluids using the Path Integral Monte Carlo method (PIMC) at finite temperature, as well as Path Integral Ground State method (PIGS) when dealing with systems at zero temperature. The exact results provided by the PIMC method are of great relevance, as well as its adaptability that allows us to use the same code within different systems by only performing some minor changes in the Hamiltonian.

All the results obtained in the calculations where obtained using the Chin action as our approximation for the thermal density matrix. We have studied other possible actions that, in principle, could provide us with faster convergence to the exact result. However, in the end, the Chin action proved to be superior in almost all the cases. We also presented a parallelization scheme for the PIMC method. Despite the PIMC proposals of movement not having any N^2 loop, where N is the number of particles, we established a procedure to obtain some speed gain in the calculation. This gain is strongly tied to the number of particles and length of the polymer chains, thus being important when dealing with low temperature systems since the number of *beads* needed in a PIMC scheme greatly increases when lowering the temperature. However, as the PIGS method usually requires a reasonable number of *beads*, it cannot obtain any substantial gain from this parallelization scheme.

Finally, as an outlook, we report the main conclusions of each chapter.

Phase diagram of a one-dimensional Coulomb gas

In Chapter 3 we have carried out a complete PIMC study of the density-temperature phase diagram of a 1D quantum Coulomb wire. The singularity of the Coulomb interaction at $x = 0$ allows us to solve the sign problem and makes it possible to carry out an exact calculation of the electron gas problem since we know a priori the exact position of the Fermi nodes. This is clearly a special feature of the 1D environment which cannot be translated to higher dimensions. There, in 2D and 3D, one can only access to approximate solutions to the many-body problem which worsen when the the temperature is not zero. Focusing our analysis on energetic and structural properties we have been able to characterize the different regimes of the electron wire. In spite of the lack of real phase transitions due to the strictly 1D character of the system, we have been able to define different physical regimes, including the Wigner crystal (classical and quantum), the classical Coulomb gas, and the universal ideal Fermi gas. Two relevant features make this phase diagram specially interesting: the large stability domain of the ideal Fermi gas and the double crossing gas-crystal-gas with increasing density within a quite wide temperature window. Our results are relevant to current and future experiments with electrons in a quantum wire and to Coulomb ions in one-dimensional confinement.

Luttinger parameter of quasi-one-dimensional para-H_2

In Chapter 4, we have studied the ground-state (zero temperature) properties of 1D and quasi-1D p-H_2 by means of the path integral ground state Monte Carlo method. For the quasi-1D case we have used two models: the inner channel inside a (10,10) carbon nanotube preplated with H_2 and a radial harmonic confinement with variable strength. The calculation of the equations of state in the three cases has allowed for an accurate determination of the equilibrium densities of the three systems. As expected, ρ_0 increases slightly when radial direction opens because the strong H_2-H_2 interaction is effectively reduced. The effect is however quite small. The spinodal point of the three problems is indistinguishable within our numerical resolution and remains very close to ρ_0.

From the low-k behavior of the static structure factor we estimate the speed of sound, and from it, the Luttinger parameter K. In this way, we report results

for the evolution of K with the density. K decreases monotonically with ρ in all cases. In all the density regime in which the system is stable, $K < 1/2$ and thus, according to Luttinger theory p-H_2 is a quasi-crystal. For a particular density, we observe as K increases going from strictly 1D to quasi-1D but the effect is not large enough to surpass the quasi-crystal threshold.

Dynamic structure factor of ^{4}He across the normal-superfluid transition

In Chapter 5, we have carried out PIMC calculations of liquid ^{4}He in a wide range of temperatures across the normal-superfluid transition T_λ to calculate the imaginary-time intermediate scattering function $F(q, \tau)$. From these functions one can in principle access to the dynamic response $S(q, \omega)$ through an inverse Laplace transform. But this is an ill-conditioned problem that can not be solved to deal with a unique solution. In recent works [135], it has been shown that the use of stochastic optimization tools can produce results with a richer structure than previous attempts relying on the maximum entropy method [131]. We have adopted here the well-known simulated annealing technique to extract the dynamic response, without any a priori bias in the search in order to get a result as unbiased as possible. In spite of the lack of any constraint in the cost function, we have verified that the three lowest energy-weighted sum rules are satisfactorily satisfied giving us some confidence on the reliability of our algorithm.

The results of the dynamic response are still not enough sharp in the quasi-particle peaks of the superfluid phase but the position of the peaks and the area below them are in nice agreement with experimental data. Interestingly, our results show clearly the signature of the transition in the roton peak, whose amplitude drops rapidly for $T > T_\lambda$. The effect of the temperature on the phonon-roton spectrum, static structure factor, and static response has been also studied.

The difficulties of extending correlated perturbative approaches to finite T have lead to a really unexplored dynamics of superfluid liquid ^{4}He, at least from a microscopic approach. With the present work, which can be considered an extension and improvement of a previous work based on the maximum entropy method [141], we have shown that the combination of PIMC and stochastic reconstruction is able to produce a satisfactory description of the quantum dynamics at finite temperature. We are also convinced that in the near future we can improve even more the present results. In this respect, one of the more

promising avenues could be the estimation of complex-time correlation functions, instead of the merely imaginary ones, which can reduce the ill-posed character of the inversion problem due to its non-monotonic structure [136] (see chapter 6).

As for the study of the momentum distribution, our aim has been to determine the possible origin of the kink that $n(k)$ shows at k values around the roton momentum. This is not the first observation of this kink in theoretical calculations since it was already obtained more that twenty years ago [144]. The location of the kink around the roton momentum led the idea of its relation with the roton but without further analysis. Now, we have shown that this scenario is more plausible because the kink vanishes when T_λ is crossed, mimicking the behavior of the roton quasi-particle peak.

Sampling of complex-time correlation functions

In Chapter 6 we have extended the calculation of complex-time correlation functions, specifically the density-density correlation function, previously studied in the work of Rota *et al.* [136] to multi-particle systems interacting with an harmonic potential. The results obtained for the density-density correlation function in complex time show a higher variance that the ones obtained for one-particle systems, but still are in a good enough accordance with the exact values. By solving the inversion problem, we obtain the dynamic structure factor for such systems, that clearly benefits for the parameter δ, thus obtaining better results for a low value of δ, near the pure real time, as happens for the one-particle system. The results for the density-density correlation function for a higher number of particles show that, despite the cost of the sampling rising, it is possible to obtain good results within a certain time window.

In further works we intend to apply the used method to real systems such as ^{4}He, in order to improve the currently obtained results for the dynamic structure factor using pure imaginary-time correlation functions.

Appendix A

Staging algorithm for the Chin action

In this appendix, we provide a detailed description of the staging algorithm (section 2.4.1) for its implementation with the Chin action (section 2.3.1). Actually, this description works for every propagator with different time steps, as is the case of symplectic expansions.

We want to construct a path corresponding to free action between two fixed points $r_{i,0}$ and $r_{i,m}$, with i being the particle where we are performing the staging. We will refer to $m+1$ as the length of the staging, and the number of *beads* moved will be $m-1$.

The free action for this segment $r_{i,0} \dots r_{i,m}$ is given by

$$p_{\text{free}} = \exp\left[-\sum_{j=1}^{m} c_j \left(\boldsymbol{r}_{i,j} - \boldsymbol{r}_{i,j-1}\right)^2\right] , \tag{A.1}$$

where c_j will be different for each Chin Action stage, as

$$c_j = \frac{1}{4\lambda\tau t_j} , \tag{A.2}$$

with t_j being t_1 or $2t_0$ as can be seen in equation 2.32.

We want the staging transformation to yield a formula for our reconstruction path as

$$p_{\text{staging}} = C(\boldsymbol{r}_{i,0}, \boldsymbol{r}_{i,m}) \ \exp\left[-\sum_{j=1}^{m-1} q_j \left[\boldsymbol{r}_{i,j} - (a_j \boldsymbol{r}_{i,j-1} + b_j \boldsymbol{r}_{i,m})\right]^2\right] , \tag{A.3}$$

where $C(r_{i,0}, r_{i,m})$ is a constant factor which only depends on the initial and final coordinates. This constant is not important in our implementation of the staging algorithm for Chin, since the boundaries of the staging $r_{i,0}$ and $r_{i,m}$ are constants.

The problem now is to know the relations between the new parameters $\{q_j, a_j, b_j\}$ and the original ones $\{c_j\}$. The first ones only have a finite value for values of $j = \{1 \dots m-1\}$, so $q_m = a_m = b_m = 0$. Knowing this, we can begin computing the unknown coefficients of $j = m-1$:

$$\begin{aligned} c_{m-1}(\boldsymbol{r}_{i,m-1} - \boldsymbol{r}_{i,m-2})^2 + c_m(\boldsymbol{r}_{i,m} - \boldsymbol{r}_{i,m-1})^2 = \\ \boldsymbol{r}_{i,m-1}^2(c_{m-1} + c_m) - 2c_{m-1}\boldsymbol{r}_{i,m-1}\boldsymbol{r}_{i,m-2} \\ -2c_m\boldsymbol{r}_{i,m}\boldsymbol{r}_{i,m-1} + c_{m-1}\boldsymbol{r}_{i,m-2}^2 + c_m\boldsymbol{r}_{i,m}^2 \end{aligned}$$

and

$$\begin{aligned} q_{m-1}\left[\boldsymbol{r}_{i,m-1} - (a_{m-1}\boldsymbol{r}_{i,m-2} + b_{m-1}\boldsymbol{r}_{i,m})\right]^2 = \\ q_{m-1}\Big[\boldsymbol{r}_{i,m-1}^2 - 2a_{m-1}\boldsymbol{r}_{i,m-1}\boldsymbol{r}_{i,m-2} + 2a_{m-1}b_{m-1}\boldsymbol{r}_{i,m-2}\boldsymbol{r}_{i,m} \\ -2b_{m-1}\boldsymbol{r}_{i,m-1}\boldsymbol{r}_{i,m} + a_{m-1}^2\boldsymbol{r}_{i,m-2}^2 + b_{m-1}^2\boldsymbol{r}_{i,m}^2\Big] \end{aligned}$$

By equaling the terms with $\boldsymbol{r}_{i,m-1}$, we obtain:

$$\begin{aligned} \boldsymbol{r}_{i,m-1}(c_m + c_{m-1}) - 2c_m\boldsymbol{r}_{i,m} - 2c_{m-1}\boldsymbol{r}_{i,m-2} = \\ \boldsymbol{r}_{i,m-1}q_{m-1} - 2q_{m-1}b_{b-1}\boldsymbol{r}_{i,m} - 2q_{m-1}a_{m-1}\boldsymbol{r}_{i,m-2}\ , \end{aligned}$$

that yields an expression for our staging coefficients:

$$\begin{aligned} q_{m-1} &= c_{m-1} + c_m \\ a_{m-1} &= \frac{c_{m-1}}{q_{m-1}} \\ b_{m-1} &= \frac{c_m}{q_{m-1}} \end{aligned} \tag{A.4}$$

As can be observed, the terms without $\boldsymbol{r}_{i,m-1}$ appear in the previous expressions, being

$$c_{m-1}\boldsymbol{r}_{i,m-2}^2 + c_m\boldsymbol{r}_{i,m}^2$$

and

$$q_{m-1}\left[2a_{m-1}b_{m-1}\boldsymbol{r}_{i,m-2}\boldsymbol{r}_{i,m}+a_{m-1}^2\boldsymbol{r}_{i,m-2}^2+b_{m-1}^2\boldsymbol{r}_{i,m}^2\right]\ .$$

We must carry over this terms when we repeat this procedure at a lower value of j. Is not needed to carry over the terms with only $\boldsymbol{r}_{i,m}^2$ dependence, since they only lead to a final constant value at $j=1$.

We do the same for $j=m-2$:

$$c_{m-2}(\boldsymbol{r}_{i,m-2}-\boldsymbol{r}_{i,m-3})^2=c_{m-2}(\boldsymbol{r}_{i,m-2}^2+\boldsymbol{r}_{i,m-3}^2-2\boldsymbol{r}_{i,m-2}\boldsymbol{r}_{i,m-3})\ .$$

When adding the remaining terms of the first term, this results in:

$$(c_{m-2}+c_{m-1})\boldsymbol{r}_{i,m-2}^2+c_{m-2}(\boldsymbol{r}_{i,m-3}^2-2\boldsymbol{r}_{i,m-2}\boldsymbol{r}_{i,m-3})$$

For the staging expression:

$$\begin{aligned}q_{m-2}\left[\boldsymbol{r}_{i,m-2}-(a_{m-2}\boldsymbol{r}_{i,m-3}+b_{m-2}\boldsymbol{r}_{i,m})\right]^2=\\ q_{m-2}\Big[\boldsymbol{r}_{i,m-2}^2-2a_{m-2}\boldsymbol{r}_{i,m-2}\boldsymbol{r}_{i,m-3}+2a_{m-2}b_{m-2}\boldsymbol{r}_{i,m-3}\boldsymbol{r}_{i,m}\\ -2b_{m-2}\boldsymbol{r}_{i,m-2}\boldsymbol{r}_{i,m}+a_{m-2}^2\boldsymbol{r}_{i,m-3}^2+b_{m-2}^2\boldsymbol{r}_{i,m}^2\Big]\ ,\end{aligned}$$

and we must add the remaining terms of the first part, that are:

$$2q_{m-1}a_{m-1}b_{m-1}\boldsymbol{r}_{i,m-2}\boldsymbol{r}_{i,m}+q_{m-1}a_{m-1}^2\boldsymbol{r}_{i,m-2}^2+q_{m-1}b_{m-1}^2\boldsymbol{r}_{i,m}^2\ .$$

Therefore:

$$\begin{aligned}q_{m-2}&=c_{m-2}+c_{m-1}-q_{m-1}a_{m-1}^2\\ a_{m-2}&=\frac{c_{m-2}}{q_{m-2}}\\ b_{m-2}&=\frac{q_{m-1}a_{m-1}b_{m-1}}{q_{m-2}}\end{aligned}\tag{A.5}$$

Iterating, one arrives to the general recursive relations:

$$\begin{aligned}q_j&=c_j+c_{j+1}-q_{j+1}a_{j+1}^2\\ a_j&=\frac{c_j}{q_j}\\ b_j&=\frac{q_{j+1}a_{j+1}b_{j+1}+c_m\delta_{j,m-1}}{q_j}\end{aligned}\tag{A.6}$$

with starting conditions as before

$$q_m = a_m = b_m = 0 \tag{A.7}$$

and the recursive relations go from $j = m - 1$ to $j = 1$.

Appendix B

Virial estimator for the energy using the Chin action

The virial estimator can be computed from

$$\begin{aligned}\frac{E_V}{N} = \Bigg\langle \frac{d}{2\beta} + \frac{1}{12\lambda N M^2 \tau^2} \sum_{\alpha=1}^{M}\sum_{i=1}^{N} \left(\boldsymbol{r}_{M+\alpha,i} - \boldsymbol{r}_{\alpha,i}\right)\left(\vec{r}_{M+\alpha-1,i} - \boldsymbol{r}_{M+\alpha,i}\right) \\ + \frac{1}{2N\beta} \sum_{\alpha=1}^{M}\sum_{i=1}^{N} \left(\boldsymbol{r}_{\alpha,i} - \boldsymbol{r}^{C}_{\alpha,i}\right) \frac{\partial}{\partial \boldsymbol{r}_{\alpha,i}} \left(U(\boldsymbol{R}_\alpha)\right) \\ + \frac{1}{NM} \sum_{\alpha=1}^{M} \frac{\partial U(\boldsymbol{R}_\alpha)}{\partial \tau} \Bigg\rangle\end{aligned} \tag{B.1}$$

where

$$\begin{aligned}U(\boldsymbol{R}_\alpha) = \tau \sum_{i<j}^{N} \left(\frac{v_1}{2} V(r_{\alpha,ij}) + v_2 V(r_{\alpha A,ij}) + v_1 V(r_{\alpha B,ij}) + \frac{v_1}{2} V(r_{\alpha+1,ij})\right) \\ + 2\tau^3 u_0 \lambda \sum_{i=1}^{N} \left(\frac{a_1}{2} \left|\boldsymbol{F}_{\alpha,i}\right|^2 + (1-2a_1)\left|\boldsymbol{F}_{\alpha A,i}\right|^2 + a_1 \left|\boldsymbol{F}_{\alpha B,i}\right|^2 + \frac{a_1}{2}\left|\boldsymbol{F}_{\alpha+1,i}\right|^2\right)\end{aligned} \tag{B.2}$$

is the potential part of the action and

$$\boldsymbol{r}^{C}_{\alpha,i} = \frac{1}{2M} \sum_{l=0}^{M-1} \left(\boldsymbol{r}_{\alpha+l,i} + \boldsymbol{r}_{\alpha-l,i}\right)$$

The 4th term is the same that arises from the potential computed via thermodynamic estimator.

$$\frac{1}{NM} \sum_{\alpha=1}^{M} \frac{\partial U(\boldsymbol{R}_\alpha)}{\partial \tau} = \frac{1}{NM} \left(V_{MN} + 6\tau^2 u_0 \lambda W_{MN}\right)$$

From the 3rd term two terms arises, one from the potential and another from the gradient (or double commutator).

$$\begin{aligned}\frac{E_V^{(3)}}{N} = &\frac{1}{2N\beta}\sum_{\alpha=1}^{M}\sum_{k=1}^{N}\left(\boldsymbol{r}_{\alpha,k}-\boldsymbol{r}_{\alpha,k}^{C}\right)\frac{\partial}{\partial \boldsymbol{r}_{\alpha,k}}\\ &\left(\tau\sum_{i<j}^{N}\left(\frac{v_1}{2}V(r_{\alpha,ij})+v_2V(r_{\alpha A,ij})+v_1V(r_{\alpha B,ij})+\frac{v_1}{2}V(r_{\alpha+1,ij})\right)\right.\\ &\left.+\,2\tau^3u_0\lambda\sum_{i=1}^{N}\left(\frac{a_1}{2}\left|\boldsymbol{F}_{\alpha,i}\right|^2+(1-2a_1)\left|\boldsymbol{F}_{\alpha A,i}\right|^2+a_1\left|\boldsymbol{F}_{\alpha B,i}\right|^2+\frac{a_1}{2}\left|\boldsymbol{F}_{\alpha+1,i}\right|^2\right)\right)\end{aligned}$$

We will solve this derivatives ignoring the bead index α, so a simplified expression will look like

$$\frac{E_V^{(3)}}{N} = \frac{1}{2N\beta}\sum_{k=1}^{N}\left(\boldsymbol{r}_k-\boldsymbol{r}_k^{C}\right)\frac{\partial}{\partial \boldsymbol{r}_k}\left(\tau\sum_{i<j}^{N}V(r_{ij})+2\tau^3u_0\lambda\sum_{i=1}^{N}\left|\boldsymbol{F}_i\right|^2\right)$$

For the fist of these terms:

$$\begin{aligned}\frac{E_V^{(3,1)}}{N} &= \frac{\tau}{2N\beta}\sum_{k=1}^{N}\left(\boldsymbol{r}_k-\boldsymbol{r}_k^{C}\right)\frac{\partial}{\partial \boldsymbol{r}_k}\sum_{i<j}^{N}V(r_{ij}) = \frac{1}{2NM}\frac{1}{2}\sum_{k=1}^{N}\sum_{i=1}^{N}\sum_{\substack{j=1\\ j\neq i}}^{N}\left(\boldsymbol{r}_k-\boldsymbol{r}_k^{C}\right)\boldsymbol{\nabla}_kV(r_{ij})\\ &= \frac{1}{2NM}\frac{1}{2}\sum_{i=1}^{N}\sum_{\substack{j=1\\ j\neq i}}^{N}\left[\left(\boldsymbol{r}_i-\boldsymbol{r}_i^{C}\right)\boldsymbol{\nabla}_iV(r_{ij})+\left(\boldsymbol{r}_j-\boldsymbol{r}_j^{C}\right)\boldsymbol{\nabla}_j\underbrace{V(r_{ij})}_{V(r_{ji})}\right]\\ &= \frac{1}{2NM}\frac{1}{2}\sum_{i=1}^{N}\sum_{\substack{j=1\\ j\neq i}}^{N}\left[\left(\boldsymbol{r}_i-\boldsymbol{r}_i^{C}\right)\boldsymbol{\nabla}_iV(r_{ij})+\left(\boldsymbol{r}_j-\boldsymbol{r}_j^{C}\right)\boldsymbol{\nabla}_jV(r_{ji})\right] \qquad \text{(B.3)}\\ &= \frac{1}{2NM}\sum_{i=1}^{N}\sum_{\substack{j=1\\ j\neq i}}^{N}\left(\boldsymbol{r}_i-\boldsymbol{r}_i^{C}\right)\boldsymbol{\nabla}_iV(r_{ij}) = \frac{1}{2NM}\sum_{i=1}^{N}\left(\boldsymbol{r}_i-\boldsymbol{r}_i^{C}\right)\boldsymbol{F}_i\end{aligned}$$

For the second term:

$$\frac{E_V^{(3,2)}}{N} = \frac{2\tau^3u_0\lambda}{2N\beta}\sum_{k=1}^{N}\left(\boldsymbol{r}_k-\boldsymbol{r}_k^{C}\right)\frac{\partial}{\partial \boldsymbol{r}_k}\sum_{i=1}^{N}\left|\boldsymbol{F}_i\right|^2 = \frac{\tau^2u_0\lambda}{NM}\sum_{k=1}^{N}\sum_{i=1}^{N}\left(\boldsymbol{r}_k-\boldsymbol{r}_k^{C}\right)\frac{\partial}{\partial \boldsymbol{r}_k}\left|\boldsymbol{F}_i\right|^2$$

We decompose this expression for d coordinates of the system, knowing that $|\boldsymbol{F}_i|^2 = \sum_{b=1}^{d} (F_i)_b^2$:

$$\begin{aligned}\frac{E_V^{(3,2)}}{N} &= \frac{\tau^2 u_0 \lambda}{NM} \sum_{a=1}^{d} \sum_{b=1}^{d} \sum_{k=1}^{N} \sum_{i=1}^{N} \left(r_k - r_k^C\right)^a \frac{\partial (F_i)_b^2}{\partial (r_k)^a} \\ &= \frac{2\tau^2 u_0 \lambda}{NM} \sum_{a=1}^{d} \sum_{b=1}^{d} \sum_{k=1}^{N} \sum_{i=1}^{N} \left(r_k - r_k^C\right)^a \frac{\partial (F_i)_b}{\partial (r_k)^a} (F_i)_b\end{aligned}$$

The term $\partial (F_i)_b / \partial (r_k)^a$ will be expanded separately:

$$\begin{aligned}\frac{\partial (F_i)_b}{\partial (r_k)^a} &= \frac{\partial}{\partial (r_k)^a} \left(\sum_{\substack{j=1 \\ j \neq i}}^{N} \frac{\partial}{\partial (r_i)_b} V(r_{ij}) \right) = \sum_{\substack{j=1 \\ j \neq i}}^{N} \frac{\partial}{\partial (r_k)^a} \left(\frac{\partial r_{ij}}{\partial (r_i)_b} \frac{\partial V(r_{ij})}{\partial r_{ij}} \right) \\ &= \sum_{\substack{j=1 \\ j \neq i}}^{N} \frac{\partial}{\partial (r_k)^a} \left(\frac{(r_{ij})_b}{r_{ij}} \frac{\partial V(r_{ij})}{\partial r_{ij}} \right)\end{aligned}$$

where we used $r_{ij} = \sqrt{\sum_{a=1}^{d} (r_{ij})_a^2}$ to simplify. Further computations lead to:

$$\begin{aligned}\frac{\partial (F_i)_b}{\partial (r_k)^a} &= \sum_{\substack{j=1 \\ j \neq i}}^{N} \left[\frac{\partial V(r_{ij})}{\partial r_{ij}} \left(\frac{\partial}{\partial (r_k)^a} \frac{(r_{ij})_b}{r_{ij}} \right) + \frac{(r_{ij})_b}{r_{ij}} \left(\underbrace{\frac{\partial}{\partial (r_k)^a}}_{\frac{\partial r_{ij}}{\partial (r_{ij})^a} \frac{\partial}{\partial r_{ij}}} \frac{\partial V(r_{ij})}{\partial r_{ij}} \right) \right] \\ &= \sum_{\substack{j=1 \\ j \neq i}}^{N} \underbrace{\left[\frac{\partial V(r_{ij})}{\partial r_{ij}} \left(\frac{\frac{\partial (r_{ij})_b}{\partial (r_k)^a} r_{ij} - \frac{\partial r_{ij}}{\partial (r_k)^a} (r_{ij})_b}{r_{ij}^2} \right) + \frac{\partial^2 V(r_{ij})}{\partial r_{ij}^2} \frac{(r_{ij})_b}{r_{ij}} \frac{\partial r_{ij}}{\partial (r_k)^a} \right]}_{\Upsilon(i,j,k)_a^b}\end{aligned} \tag{B.4}$$

with

$$\frac{\partial r_{ij}}{\partial (r_k)^a} = \begin{cases} \frac{(r_{ij})^a}{r_{ij}} & i = k \\ -\frac{(r_{ij})^a}{r_{ij}} & j = k \\ 0 & i \neq k \neq j \end{cases}$$

$$\frac{\partial (r_{ij})_b}{\partial (r_k)^a} = \begin{cases} \delta_a^b & i = k \\ -\delta_a^b & j = k \\ 0 & i \neq k \neq j \end{cases}$$

Since k can only take values equal to i or j, the tensor Υ falls to tensor T:

$$\begin{aligned}\Upsilon(i,j,i)^b_a &= T(i,j)^b_a \\ \Upsilon(i,j,j)^b_a &= -T(i,j)^b_a \\ T(i,j)^b_a &= T(j,i)^b_a\end{aligned}$$

Where $T(i,j)^b_a$ is

$$T(i,j)^b_a = \left[\frac{\delta^b_a}{r_{ij}} - \frac{(r_{ij})^b(r_{ij})_a}{r^3_{ij}}\right]\frac{dV(r_{ij})}{dr_{ij}} + \frac{(r_{ij})^b(r_{ij})_a}{r^2_{ij}}\frac{d^2V(r_{ij})}{dr^2_{ij}} \tag{B.5}$$

Thus, the expression for this term ends as:

$$\begin{aligned}\frac{E^{(3,2)}_V}{N} &= \frac{2\tau^2 u_0\lambda}{NM}\sum_{a=1}^{d}\sum_{b=1}^{d}\sum_{i=1}^{N}\sum_{\substack{j=1\\j\neq i}}^{N}\left[\left(r_i - r^C_i\right)^a T(i,j)^b_a(F_i)_b - \left(r_j - r^C_j\right)^a \underbrace{T(i,j)^b_a}_{T(j,i)^b_a}(F_i)_b\right] \\ &= \frac{2\tau^2 u_0\lambda}{NM}\sum_{a=1}^{d}\sum_{b=1}^{d}\sum_{i=1}^{N}\sum_{\substack{j=1\\j\neq i}}^{N}\left(r_i - r^C_i\right)^a T(i,j)^b_a\left(F_i - F_j\right)_b\end{aligned} \tag{B.6}$$

In order to ease the resulting equation, one can write some terms similar to the equations 2.55 and 2.57.

$$\begin{aligned}T^{\text{off}}_{MN} = \sum_{\alpha=1}^{M}\sum_{i=1}^{N}\Bigg(&\frac{1}{t_1}\left(\boldsymbol{r}_{M+\alpha,i} - \boldsymbol{r}_{\alpha,i}\right)\left(\boldsymbol{r}_{\alpha,i} - \boldsymbol{r}_{\alpha A,i}\right) \\ &+\frac{1}{t_1}\left(\boldsymbol{r}_{M+\alpha A,i} - \boldsymbol{r}_{\alpha A,i}\right)\left(\boldsymbol{r}_{\alpha A,i} - \boldsymbol{r}_{\alpha B,i}\right) \\ &+\frac{1}{2t_0}\left(\boldsymbol{r}_{M+\alpha B,i} - \boldsymbol{r}_{\alpha B,i}\right)\left(\boldsymbol{r}_{\alpha B,i} - \boldsymbol{r}_{\alpha+1,i}\right)\Bigg)\end{aligned} \tag{B.7}$$

$$\begin{aligned}T^{V}_{MN} = \sum_{\alpha=1}^{M}\sum_{i=1}^{N}\Bigg(&\frac{v_1}{2}(\boldsymbol{r}_{\alpha,i} - \boldsymbol{r}_{o,i})\boldsymbol{F}_{\alpha,i} + v_2(\boldsymbol{r}_{\alpha A,i} - \boldsymbol{r}_{o,i})\boldsymbol{F}_{\alpha A,i} \\ &+ v_1(\boldsymbol{r}_{\alpha B,i} - \boldsymbol{r}_{o,i})\boldsymbol{F}_{\alpha B,i} + \frac{v_1}{2}(\boldsymbol{r}_{\alpha+1,i} - \boldsymbol{r}_{o,i})\boldsymbol{F}_{\alpha+1,i}\Bigg)\end{aligned} \tag{B.8}$$

$$Y_{MN} = \sum_{\alpha=1}^{M}\sum_{i=1}^{N}\sum_{\substack{j=1\\ j\neq i}}^{N}\sum_{a=1}^{d}\sum_{b=1}^{d}\Big(\frac{a_1}{2}(r_{\alpha,i}-r_{o,i})^a T(\alpha,i,j)_a^b (F_{\alpha,i}-F_{\alpha,j})_b$$
$$+(1-2a_1)(r_{\alpha A,i}-r_{o,i})^a T(\alpha A,i,j)_a^b (F_{\alpha A,i}-F_{\alpha A,j})_b \tag{B.9}$$
$$+a_1(r_{\alpha B,i}-r_{o,i})^a T(\alpha B,i,j)_a^b (F_{\alpha B,i}-F_{\alpha B,j})_b$$
$$+\frac{a_1}{2}(r_{\alpha+1,i}-r_{o,i})^a T(\alpha+1,i,j)_a^b (F_{\alpha+1,i}-F_{\alpha+1,j})_b\Big)$$

So, we can write the virial estimator as:

$$\frac{E_V}{N} = \frac{d}{2\beta} + \frac{1}{NM}\Big(\frac{1}{12\lambda M\tau^2}T^{\text{off}}_{MN} + \frac{1}{2}T^V_{MN}$$
$$+2\tau^2 u_0\lambda Y_{MN} + V_{MN} + 6\tau^2 u_0\lambda W_{MN}\Big) \tag{B.10}$$

$$\frac{K_V}{N} = \frac{d}{2\beta} + \frac{1}{NM}\Big(\frac{1}{12\lambda M\tau^2}T^{\text{off}}_{MN} + \frac{1}{2}T^V_{MN} + 2\tau^2 u_0\lambda(W_{MN}+Y_{MN})\Big) \tag{B.11}$$

The potential part of the energy is the same as the one computed via the thermodynamic estimator 2.63.

$$\frac{V}{N} = \frac{1}{NM}\Big(V_{MN} + 4\tau^2 u_0\lambda W_{MN}\Big) \tag{B.12}$$

Appendix C

Derivation of estimators for the pressure using the Chin action

Thermodynamic estimator

The pressure can be derived from the partition function.

$$P = \frac{1}{\beta Z}\frac{\partial Z}{\partial V} \tag{C.1}$$

In order to do so, we need to introduce the rescaled coordinates $\boldsymbol{R}_m^* = \boldsymbol{R}_m/V^{1/d}$, where d is the dimension of the system. The partition function follows the equation 2.53, while the action follows 2.54.

In order to the calculate the partial derivative of the volume, we need to introduce the rescaled coordinates.

$$\frac{\partial}{\partial V} = \sum_{k=1}^{N}\frac{\partial \boldsymbol{r}_{\alpha,k}}{\partial V}\frac{\partial}{\partial \boldsymbol{r}_{\alpha,k}} = \frac{1}{dV}\sum_{k=1}^{N}\boldsymbol{r}_{\alpha,k}\frac{\partial}{\partial \boldsymbol{r}_{\alpha,k}} \tag{C.2}$$

So, calculating the equation C.1, we find:

$$\begin{aligned}\frac{\partial Z}{\partial V} &= 3NMV^{3NM-1}\left(\frac{1}{4\pi\lambda\tau}\right)^{\frac{3dMN}{2}}\left(\frac{1}{2t_1^2t_0}\right)^{\frac{dNM}{2}}\int(...) - Z\frac{\partial S_0}{\partial V} \\ &= \frac{3NM}{V}Z - \frac{\partial S_0}{\partial V}Z\end{aligned} \tag{C.3}$$

Now, we derive the three terms of the action S_0.

$$\begin{aligned}\frac{\partial S_0^{(1)}}{\partial V} &= \frac{\partial}{\partial V}\left(\frac{1}{4\lambda\tau}\sum_{i=1}^{N}\sum_{\alpha=1}^{M}\left(\frac{1}{t_1}\left(\boldsymbol{r}^*_{\alpha,i}-\boldsymbol{r}^*_{\alpha A,i}\right)^2 V^{2/d}+...\right)\right)\\ &= \frac{2}{4\lambda\tau d}V^{2/d-1}\sum_{i=1}^{N}\sum_{\alpha=1}^{M}\left(\frac{1}{t_1}\left(\boldsymbol{r}^*_{\alpha,i}-\boldsymbol{r}^*_{\alpha A,i}\right)^2+...\right)\\ &= \frac{1}{2d\lambda\tau V}\sum_{i=1}^{N}\sum_{\alpha=1}^{M}\left(\frac{1}{t_1}\left(\boldsymbol{r}_{\alpha,i}-\boldsymbol{r}_{\alpha A,i}\right)^2+...\right)\end{aligned} \tag{C.4}$$

The second term is quite similar from the one obtained for the virial estimator of the energy B.3.

$$\begin{aligned}\frac{\partial S_0^{(2)}}{\partial V} &= \frac{\partial}{\partial V}\left(\tau\sum_{i<j}^{N}\sum_{\alpha=1}^{M}\left(\frac{v_1}{2}V(r_{\alpha,ij})+...\right)\right) = \frac{\tau}{2dV}\sum_{\alpha=1}^{M}\sum_{i=1}^{N}\sum_{\substack{j=1\\j\neq i}}^{N}\sum_{k=1}^{N}\left(\frac{v_1}{2}\boldsymbol{r}_{\alpha,k}\frac{\partial V(r_{\alpha,ij})}{\partial \boldsymbol{r}_{\alpha,k}}+...\right)\\ &= \frac{\tau}{2dV}\sum_{\alpha=1}^{M}\sum_{i=1}^{N}\sum_{\substack{j=1\\j\neq i}}^{N}\left(\frac{v_1}{2}\left(\boldsymbol{r}_{\alpha,i}\frac{\partial}{\partial \boldsymbol{r}_{\alpha,i}}V(r_{\alpha,ij})+\boldsymbol{r}_{\alpha,j}\underbrace{\frac{\partial}{\partial \boldsymbol{r}_{\alpha,j}}V(r_{\alpha,ij})}_{-\partial_{\boldsymbol{r}_{\alpha,i}}V(r_{\alpha,ij})}\right)+...\right)\\ &= \frac{\tau}{2dV}\sum_{\alpha=1}^{M}\sum_{i=1}^{N}\sum_{\substack{j=1\\j\neq i}}^{N}\left(\frac{v_1}{2}\left(\boldsymbol{r}_{\alpha,i}-\boldsymbol{r}_{\alpha,j}\right)\frac{\partial}{\partial \boldsymbol{r}_{\alpha,i}}V(r_{\alpha,ij})+...\right)\\ &= \frac{\tau}{2dV}\sum_{\alpha=1}^{M}\sum_{i=1}^{N}\sum_{\substack{j=1\\j\neq i}}^{N}\left(\frac{v_1}{2}\boldsymbol{r}_{\alpha,ij}\boldsymbol{f}_{\alpha,ij}+v_2\boldsymbol{r}_{\alpha A,ij}\boldsymbol{f}_{\alpha A,ij}+v_1\boldsymbol{r}_{\alpha B,ij}\boldsymbol{f}_{\alpha B,ij}+\frac{v_1}{2}\boldsymbol{r}_{\alpha+1,ij}\boldsymbol{f}_{\alpha+1,ij}\right)\end{aligned} \tag{C.5}$$

with $\boldsymbol{f}_{\alpha,ij}=\partial_{\boldsymbol{r}_{\alpha,i}}V(r_{\alpha,ij})$. In this case we make use of $(\boldsymbol{r}_i\boldsymbol{\nabla}_i V(r_{ij})+\boldsymbol{r}_j\boldsymbol{\nabla}_j V(r_{ij}))=(\boldsymbol{r}_i-\boldsymbol{r}_j)\boldsymbol{\nabla}_i V(r_{ij})$ in order to avoid using absolute coordinates $\boldsymbol{r}_i$ since they are ill-defined. Remember that in the virial estimator of the energy (Appendix B) we use $(\boldsymbol{r}_i\boldsymbol{\nabla}_i V(r_{ij})+\boldsymbol{r}_j\boldsymbol{\nabla}_j V(r_{ij}))=2\boldsymbol{r}_i\boldsymbol{\nabla}_i V(r_{ij})$ since the position in that case is corrected by the center of mass.

The last term is the harder one.

$$\begin{aligned}\frac{\partial S_0^{(3)}}{\partial V} &= \frac{\partial}{\partial V}\left(2\tau^3 u_0\lambda\sum_{\alpha=1}^{M}\sum_{i=1}^{N}\left(\frac{a_1}{2}\left|\boldsymbol{F}_{\alpha,i}\right|^2+...\right)\right)\\ &= \frac{2\tau^3 u_0\lambda}{dV}\sum_{\alpha=1}^{M}\sum_{i=1}^{N}\sum_{k=1}^{N}\left(\boldsymbol{r}_{\alpha,k}\frac{\partial\left|\boldsymbol{F}_{\alpha,i}\right|^2}{\partial \boldsymbol{r}_{\alpha,k}}+...\right)\end{aligned} \tag{C.6}$$

We decompose the module of the force in the coordinates $\left|\boldsymbol{F}_{\alpha,i}\right|^2=\sum_{a=1}^{d}F^2_{\alpha,i,a}$

$$\boldsymbol{r}_{\alpha,k}\frac{\partial}{\partial \boldsymbol{r}_{\alpha,k}}\left|\boldsymbol{F}_{\alpha,i}\right|^2=\sum_{a=1}^{d}\sum_{b=1}^{d}(r_{\alpha,k})^a\frac{\partial(F_{\alpha,i})_b^2}{\partial(r_{\alpha,k})_a}=2\sum_{a=1}^{d}\sum_{b=1}^{d}(r_{\alpha,k})^a\frac{\partial(F_{\alpha,i})^b}{\partial(r_{\alpha,k})_a}(F_{\alpha,i})_b$$

In this expression, the value of $\frac{\partial(F_{\alpha,i})^b}{\partial(r_{\alpha,k})_a}=\Upsilon(\alpha,i,j,k)_a^b$ is the same that appears for the virial estimator in expression B.4.

Again, k can only take values of i and j since the others combinations are equal to zero.

$$\begin{aligned}\frac{\partial S_0^{(3)}}{\partial V}&=\frac{2\tau^3u_0\lambda}{dV}\sum_{a=1}^{d}\sum_{b=1}^{d}\sum_{\alpha=1}^{M}\sum_{i=1}^{N}\sum_{k=1}^{N}\sum_{\substack{j=1\\j\neq i}}^{N}\left(2(r_{\alpha,k})^a\Upsilon(\alpha,i,j,k)_a^b(F_{\alpha,i})_b+...\right) \qquad \text{(C.7)}\\
&=\frac{2\tau^3u_0\lambda}{dV}\sum_{a=1}^{d}\sum_{b=1}^{d}\sum_{\alpha=1}^{M}\sum_{i=1}^{N}\sum_{\substack{j=1\\j\neq i}}^{N}2\left((r_{\alpha,i})^a\Upsilon(\alpha,i,j,i)_a^b(F_{\alpha,i})_b+(r_{\alpha,j})^a\Upsilon(\alpha,i,j,j)_a^b(F_{\alpha,i})_b+...\right)\\
&=\frac{2\tau^3u_0\lambda}{dV}\sum_{a=1}^{d}\sum_{b=1}^{d}\sum_{\alpha=1}^{M}\sum_{i=1}^{N}\sum_{\substack{j=1\\j\neq i}}^{N}2\left((r_{\alpha,i})^aT(\alpha,i,j)_a^b(F_{\alpha,i})_b-(r_{\alpha,j})^aT(\alpha,i,j)_a^b(F_{\alpha,i})_b+...\right)\\
&=\frac{4\tau^3u_0\lambda}{dV}\sum_{a=1}^{d}\sum_{b=1}^{d}\sum_{\alpha=1}^{M}\sum_{i=1}^{N}\sum_{\substack{j=1\\j\neq i}}^{N}\left((r_{\alpha,i}-r_{\alpha,j})^aT(\alpha,i,j)_a^b(F_{\alpha,i})_b+...\right)\end{aligned}$$

Again, knowing that $T(i,j)=T(j,i)$, we arrange the expression as $r_iT(i,j)F_i-r_jT(i,j)F_i=r_{ij}T(i,j)F_i$ in order to express it in terms of relative distances. It's, again, different from the virial estimator of energy in equation B.6, where we arrange them as $r_iT(i,j)F_i-r_jT(i,j)F_i=r_iT(i,j)(F_i-F_j)$.

So finally, the final expression for the thermodynamic estimator of the pressure using Chin action is.

$$\begin{aligned}P=&\frac{3N}{\tau V}-\frac{1}{2d\lambda M\tau^2V}\sum_{\alpha=1}^{M}\sum_{i=1}^{N}\left[\frac{1}{t_1}(\boldsymbol{r}_{\alpha,i}-\boldsymbol{r}_{\alpha A,i})^2+\frac{1}{t_1}(\boldsymbol{r}_{\alpha A,i}-\boldsymbol{r}_{\alpha B,i})^2+\frac{1}{2t_0}(\boldsymbol{r}_{\alpha B,i}-\boldsymbol{r}_{\alpha+1,i})^2\right]\\
&-\frac{1}{2dVM}\sum_{\alpha=1}^{M}\sum_{i=1}^{N}\sum_{\substack{j=1\\j\neq i}}^{N}\left[\frac{v_1}{2}\boldsymbol{r}_{\alpha,ij}\boldsymbol{f}_{\alpha,ij}+v_2\boldsymbol{r}_{\alpha A,ij}\boldsymbol{f}_{\alpha A,ij}+v_1\boldsymbol{r}_{\alpha B,ij}\boldsymbol{f}_{\alpha B,ij}+\frac{v_1}{2}\boldsymbol{r}_{\alpha+1,ij}\boldsymbol{f}_{\alpha+1,ij}\right]\\
&-\frac{4\tau^2u_0\lambda}{dVM}\sum_{a=1}^{d}\sum_{b=1}^{d}\sum_{\alpha=1}^{M}\sum_{i=1}^{N}\sum_{\substack{j=1\\j\neq i}}^{N}\left[\frac{a_1}{2}(r_{\alpha,ij})^aT(\alpha,i,j)_a^b(F_{\alpha,i})_b \qquad \text{(C.8)}\right.\\
&+(1-2a_1)(r_{\alpha A,ij})^aT(\alpha A,i,j)_a^b(F_{\alpha A,i})_b\\
&\left.+a_1(r_{\alpha B,ij})^aT(\alpha B,i,j)_a^b(F_{\alpha B,i})_b+\frac{a_1}{2}(r_{\alpha+1,ij})^aT(\alpha+1,i,j)_a^b(F_{\alpha+1,i})_b\right]\end{aligned}$$

with $T(\alpha,i,j)_a^b$ as shown at equation B.5 and $(F_{\alpha,i})_b = \sum_{j\neq i}^{N} \partial_{(r_{\alpha,i})^b} V(r_{\alpha,ij})$.

Virial estimator

For the virial estimator for the pressure we follow the same procedure as with the energy. First, we define $P_{1,L+1}$, which is the pressure corresponding to the time-slices $\boldsymbol{R}_1, ..., \boldsymbol{R}_{L+1}$ (with $1 \leq L \leq 3M$, since we have three times more beads than with other estimators).

$$P_{1,L+1} = \langle \frac{NL}{V\beta} - \frac{M}{2d\lambda\beta^2 V} \sum_{\alpha=1}^{L} (\boldsymbol{R}_\alpha - \boldsymbol{R}_{\alpha+1})^2 - \frac{1}{\beta}\frac{\partial}{\partial V} \sum_{\alpha=1}^{L} U(\boldsymbol{R}_\alpha) \rangle \tag{C.9}$$

where $\boldsymbol{R}_\alpha$ are the positions of the α-bead of the N particles, and $U(\boldsymbol{R}_\alpha) = \tau \sum_{i<j}^{N} V(r_{\alpha,ij}) + 2\tau^3 u_0 \lambda \sum_{i=1}^{N} |\boldsymbol{F}_{\alpha,i}|^2$

We can simplify equation C.9 by writing

$$P_{1,L+1} = \langle \frac{NL}{V\beta} - \frac{2}{dV}\alpha - \frac{1}{\beta}\frac{\partial}{\partial V} u \rangle \tag{C.10}$$

with

$$\alpha = \sum_{m=1}^{L} \frac{1}{4\lambda\tau^2 M} (\boldsymbol{R}_m - \boldsymbol{R}_{m+1})^2$$
$$u = \sum_{m=1}^{L} U(\boldsymbol{R}_m)$$

We now can recover the expression for this α derived for the virial estimator of energy.

$$\alpha = \frac{dN(L-1)}{2\beta} - \frac{1}{4\lambda\tau^2 M} (\boldsymbol{R}_L - \boldsymbol{R}_{L+1}) (\boldsymbol{R}_{L+1} - \boldsymbol{R}_1) - \frac{1}{2\beta} \sum_{m=2}^{L} (\boldsymbol{R}_m - \boldsymbol{R}_1) \frac{\partial u}{\partial \boldsymbol{R}_m} \tag{C.11}$$

Now we substitute the expression above in C.10.

$$
\begin{aligned}
P_{1,L+1} &= \left\langle \frac{NL}{V\beta} - \frac{N(L-1)}{V\beta} + \frac{M}{2d\lambda\beta^2 V}\left(\boldsymbol{R}_L - \boldsymbol{R}_{L+1}\right)\left(\boldsymbol{R}_{L+1} - \boldsymbol{R}_1\right) \right. \\
&\left. + \frac{1}{dV\beta}\sum_{\alpha=2}^{L}(\boldsymbol{R}_\alpha - \boldsymbol{R}_1)\frac{\partial u}{\partial \boldsymbol{R}_\alpha} - \frac{1}{\beta}\frac{\partial u}{\partial V} \right\rangle \\
&= \left\langle \frac{N}{V\beta} + \frac{M}{2d\lambda\beta^2 V}\left(\boldsymbol{R}_L - \boldsymbol{R}_{L+1}\right)\left(\boldsymbol{R}_{L+1} - \boldsymbol{R}_1\right) \right. \\
&\left. + \frac{1}{dV\beta}\sum_{\alpha=2}^{L}(\boldsymbol{R}_\alpha - \boldsymbol{R}_1)\frac{\partial u}{\partial \boldsymbol{R}_\alpha} - \frac{1}{dV\beta}\sum_{\alpha=1}^{L}\boldsymbol{R}_\alpha\frac{\partial u}{\partial \boldsymbol{R}_\alpha} \right\rangle \\
&= \left\langle \frac{N}{V\beta} + \underbrace{\frac{M}{2d\lambda\beta^2 V}\left(\boldsymbol{R}_L - \boldsymbol{R}_{L+1}\right)\left(\boldsymbol{R}_{L+1} - \boldsymbol{R}_1\right)}_{P^{(1)}_{1,L+1}} - \underbrace{\frac{1}{dV\beta}\sum_{\alpha=1}^{L}\boldsymbol{R}_1\frac{\partial u}{\partial \boldsymbol{R}_\alpha}}_{P^{(2)}_{1,L+1}} \right\rangle
\end{aligned}
$$

Now we have to arrange the two last terms. We will begin with $P^{(2)}_{1,L+1}$:

$$
\begin{aligned}
P^{(2)}_{1,L+1} &= \frac{1}{dV\beta}\sum_{\alpha=1}^{L}\boldsymbol{R}_1\frac{\partial u}{\partial \boldsymbol{R}_\alpha} = \frac{1}{dV\beta}\sum_{\alpha=1}^{L}\boldsymbol{R}_1\frac{\partial U(\boldsymbol{R}_\alpha)}{\partial \boldsymbol{R}_\alpha} \\
&= \frac{1}{dV\beta}\sum_{\alpha=1}^{L}\boldsymbol{R}_1\frac{\partial}{\partial \boldsymbol{R}_\alpha}\left[\tau\sum_{i<j}^{N}V(r_{\alpha,ij}) + 2\tau^3 u_0\lambda\sum_{i=1}^{N}\left|\boldsymbol{F}_{\alpha,i}\right|^2\right]
\end{aligned}
$$

We solve separately

$$
\begin{aligned}
\sum_{k=1}^{N}\sum_{i<j}^{N}\tau\boldsymbol{r}_{1,k}\frac{\partial}{\partial \boldsymbol{r}_{\alpha,k}}V(r_{\alpha,ij}) &= \frac{1}{2}\sum_{i,j=1}^{N}\left(\boldsymbol{r}_{1,i}\frac{\partial V(r_{\alpha,ij})}{\partial \boldsymbol{r}_{\alpha,i}} + \boldsymbol{r}_{1,j}\frac{\partial V(r_{\alpha,ij})}{\partial \boldsymbol{r}_{\alpha,j}}\right) \\
&= \frac{1}{2}\sum_{i,j=1}^{N}\boldsymbol{r}_{1,ij}\boldsymbol{f}_{\alpha,ij}
\end{aligned}
$$

and

$$
\begin{aligned}
\sum_{k=1}^{N}\sum_{i=1}^{N}\boldsymbol{r}_{1,k}\frac{\partial}{\partial \boldsymbol{r}_{\alpha,k}}\left|\boldsymbol{F}_{\alpha,i}\right|^2 &= \sum_{\substack{a=1\\b=1}}^{d}\sum_{k=1}^{N}\sum_{i=1}^{N}(r_{1,k})^a\frac{\partial(F_{\alpha,i})^b}{\partial(r_{\alpha,k})_a}2(F_{\alpha,i})_b \\
&= 2\sum_{\substack{a=1\\b=1}}^{d}\sum_{\substack{i=1\\j=1}}^{N}(r_{1,ij})^a T(\alpha,i,j)^b_a(F_{\alpha,i})_b
\end{aligned}
$$

so we find

$$
P^{(2)}_{1,L+1} = \frac{\tau}{2}\sum_{\alpha=1}^{L}\sum_{i,j=1}^{N}\boldsymbol{r}_{1,ij}\boldsymbol{f}_{\alpha,ij} + 4\tau^3 u_0\lambda\sum_{\alpha=1}^{L}\sum_{\substack{a=1\\b=1}}^{d}\sum_{\substack{i=1\\j=1}}^{N}(r_{1,ij})^a T(\alpha,i,j)^b_a(F_{\alpha,i})_b \quad \text{(C.12)}
$$

For $P^{(1)}_{1,L+1}$ we simply average over the L slices so we find:

$$P^{(1)}_{1,L+1} = \frac{M}{2d\lambda\beta^2 VL}\sum_{\alpha=1}^{L}\left(\boldsymbol{R}_{M+\alpha-1}-\boldsymbol{R}_{M+\alpha}\right)\left(\boldsymbol{R}_{M+\alpha}-\boldsymbol{R}_{\alpha}\right) \tag{C.13}$$

Finally, as with the virial estimator for the energy, we set $L = 3M$ (since we are using Chin action) and change the reference slice from $\boldsymbol{R}_1$ to $\boldsymbol{R}^C_m = \frac{1}{2L}\left[\sum_{j=0}^{L-1}\boldsymbol{R}_{m+j} + \sum_{j=0}^{-L+1}\boldsymbol{R}_{m+j}\right]$ to find the virial estimator for pressure.

$$\begin{aligned}
P_{vir} = {} & \frac{N}{V\beta} + \frac{1}{6d\lambda\beta^2 V}\sum_{i=1}^{N}\sum_{\alpha=1}^{L}\left(\boldsymbol{r}_{M+\alpha-1,i}-\boldsymbol{r}_{M+\alpha,i}\right)\left(\boldsymbol{r}_{M+\alpha,i}-\boldsymbol{r}_{\alpha,i}\right) \\
& - \frac{1}{2dVM}\sum_{\alpha=1}^{M}\sum_{i=1}^{N}\left[\frac{v_1}{2}\boldsymbol{r}^C_{\alpha,ij}\boldsymbol{f}_{\alpha,ij} + v_2\boldsymbol{r}^C_{\alpha A,ij}\boldsymbol{f}_{\alpha A,ij} + v_1\boldsymbol{r}^C_{\alpha B,ij}\boldsymbol{f}_{\alpha B,ij} + \frac{v_1}{2}\boldsymbol{r}^C_{\alpha+1,ij}\boldsymbol{f}_{\alpha+1,ij}\right] \\
& - \frac{4\tau^2 u_0\lambda}{dVM}\sum_{a=1}^{d}\sum_{b=1}^{d}\sum_{\alpha=1}^{M}\sum_{i=1}^{N}\sum_{\substack{j=1\\ j\neq i}}^{N}\left[\frac{a_1}{2}(r^C_{\alpha,ij})^a T(\alpha,i,j)^b_a (F_{\alpha,i})_b\right. \\
& + (1-2a_1)(r^C_{\alpha A,ij})^a T(\alpha A,i,j)^b_a (F_{\alpha A,i})_b \\
& \left. + a_1(r^C_{\alpha B,ij})^a T(\alpha B,i,j)^b_a (F_{\alpha B,i})_b + \frac{a_1}{2}(r^C_{\alpha+1,ij})^a T(\alpha+1,i,j)^b_a (F_{\alpha+1,i})_b\right]
\end{aligned} \tag{C.14}$$

References

[1] J. N. van der Ende W. Keesom. "The specific heat of solids obtainable with liquid helium. IV. Measurements of the atomic heats of tin and zinc." *CPL* **219b**, (1932).

[2] J. F. Allen and A. D. Misener. "Flow of Liquid Helium II". *Nature* **141**, 75, (1938).

[3] P. Kapitza. "Viscosity of Liquid Helium below the lambda-point". *Nature* **141**, 74, (1938).

[4] V. L. Ginzburg and A. A. Sobyanin. "Can liquid molecular hydrogen be superfluid?" *JETP Lett.* **15**, 242, (1972).

[5] Slava Grebenev, Boris Sartakov, J. Peter Toennies, and Andrei F. Vilesov. "Evidence for Superfluidity in Para-Hydrogen Clusters Inside Helium-4 Droplets at 0.15 Kelvin". *Science* **289**, 1532–1535, (2000). ISSN: 0036-8075.

[6] M. H. Anderson, J. R. Ensher, M. R. Matthews, C. E. Wieman, and E. A. Cornell. "Observation of Bose-Einstein Condensation in a Dilute Atomic Vapor". *Science* **269**, 198–201, (1995). ISSN: 0036-8075.

[7] K. B. Davis, M. -O. Mewes, M. R. Andrews, N. J. van Druten, D. S. Durfee, D. M. Kurn, and W. Ketterle. "Bose-Einstein Condensation in a Gas of Sodium Atoms". *Phys. Rev. Lett.* **75**, 3969–3973, (1995).

[8] Nicholas Metropolis, Arianna W. Rosenbluth, Marshall N. Rosenbluth, Augusta H. Teller, and Edward Teller. "Equation of State Calculations by Fast Computing Machines". *The Journal of Chemical Physics* **21**, 1087–1092, (1953).

[9] J. Boronat. "Monte Carlo Simulations at Zero Temperature: Helium in One, Two, and Three Dimensions". In: *Microscopic Approaches to Quantum Liquids in Confined Geometries*. Ed. by E. Krotscheck and J. Navarro. Vol. 4. Advances in Quantum Many-Body Theory. Singapore: World Scientific, 2002. 21–90.

[10] W. L. McMillan. "Ground State of Liquid He^4". *Phys. Rev.* **138**, A442–A451, (1965).

[11] Robert Jastrow. "Many-Body Problem with Strong Forces". *Phys. Rev.* **98**, 1479–1484, (1955).

[12] James B. Anderson. "A random-walk simulation of the Schrödinger equation: H+3". *The Journal of Chemical Physics* **63**, 1499–1503, (1975).

[13] D. M. Ceperley and E. L. Pollock. "Path-integral computation of the low-temperature properties of liquid ^{4}He". *Phys. Rev. Lett.* **56**, 351–354, (1986).

[14] D. M. Ceperley. "Path integrals in the theory of condensed helium". *Rev. Mod. Phys.* **67**, 279–355, (1995).

[15] M. J. Gillan. "The Path-Integral Simulation of Quantum Systems". In: *Computer Modelling of Fluids, Polymers and Solids*. Ed. by M. P. Allen C. R. A. Catlow S. C. Parker. Vol. 293. Nato Science Series C. Dordrecht: Kluwer Academic Publishers, 1990. 155–188.

[16] Charusita Chakravarty. "Path integral simulations of atomic and molecular systems". *International Reviews in Physical Chemistry* **16**, 421–444, (1997).

[17] R. P. Feynman and A. R. Hibbs. *Quantum Mechanics and Path Integrals*. New York: McGraw-Hill, 1965.

[18] R. P. Feynman. *Statistical mechanics: a set of lectures*. New York: W. A. Benjamin, 1972.

[19] H. Kleinert. *Path Integrals in Quantum Mechanics, Statistics, and Polymer Physics*. Singapore: World Scientific, 1995.

[20] J. A. Barker. "A quantum-statistical Monte Carlo method; path integrals with boundary conditions". *The Journal of Chemical Physics* **70**, 2914–2918, (1979).

[21] David Chandler and Peter G. Wolynes. "Exploiting the isomorphism between quantum theory and classical statistical mechanics of polyatomic fluids". *The Journal of Chemical Physics* **74**, 4078–4095, (1981).

[22] M. Boninsegni, N. V. Prokof'ev, and B. V. Svistunov. "Worm algorithm and diagrammatic Monte Carlo: A new approach to continuous-space path integral Monte Carlo simulations". *Phys. Rev. E* **74**, 036701, (2006).

[23] D. M. Ceperley. "Path Integral Monte Carlo Methods for Fermions". In: *Monte Carlo and Molecular Dynamics of Condensed Matter Systems*. Ed. by K. Binder and G. Ciccotti. Vol. 4. Advances in Quantum Many-Body Theory. Bologna, Italy: Editrice Compositori, 1996. 21–90.

[24] A. Sarsa, K. E. Schmidt, and W. R. Magro. "A path integral ground state method". *The Journal of Chemical Physics* **113**, 1366–1371, (2000).

[25] D. E. Galli and L. Reatto. "Recent progress in simulation of the ground state of many Boson systems". *Molecular Physics* **101**, 1697–1703, (2003).

[26] Javier E. Cuervo, Pierre-Nicholas Roy, and Massimo Boninsegni. "Path integral ground state with a fourth-order propagator: Application to condensed helium". *The Journal of Chemical Physics* **122**, 114504, (2005).

[27] H. F. Trotter. "On the product of semi-groups of operators". *Proc. Amer. Math. Soc.* **10**, 545–551, (1959).

[28] R. P. Feynman. "Atomic Theory of Liquid Helium Near Absolute Zero". *Phys. Rev.* **91**, 1301–1308, (1953).

[29] R. P. Feynman. "Atomic Theory of the λ Transition in Helium". *Phys. Rev.* **91**, 1291–1301, (1953).

[30] R. P. Feynman. "The λ-Transition in Liquid Helium". *Phys. Rev.* **90**, 1116–1117, (1953).

[31] E. L. Pollock and D. M. Ceperley. "Simulation of quantum many-body systems by path-integral methods". *Phys. Rev. B* **30**, 2555–2568, (1984).

[32] Minoru Takahashi and Masatoshi Imada. "Monte Carlo Calculation of Quantum Systems. II. Higher Order Correction". *Journal of the Physical Society of Japan* **53**, 3765–3769, (1984).

[33] Xiao-Ping Li and Jeremy Q. Broughton. "High-order correction to the Trotter expansion for use in computer simulation". *The Journal of Chemical Physics* **86**, 5094–5100, (1987).

[34] K. Sakkos, J. Casulleras, and J. Boronat. "High order Chin actions in path integral Monte Carlo". *The Journal of Chemical Physics* **130**, 204109, (2009).

[35] Qin Sheng. "Solving linear partial differential equations by exponential splitting". *IMA Journal of numerical analysis* **9**, 199–212, (1989).

[36] Masuo Suzuki. "General theory of fractal path integrals with applications to many-body theories and statistical physics". *Journal of Mathematical Physics* **32**, 400–407, (1991).

[37] Siu A. Chin. "Quantum statistical calculations and symplectic corrector algorithms". *Phys. Rev. E* **69**, 046118, (2004).

[38] Siu A. Chin and C. R. Chen. "Gradient symplectic algorithms for solving the Schrödinger equation with time-dependent potentials". *The Journal of Chemical Physics* **117**, 1409–1415, (2002).

[39] Siu A. Chin. "Higher-order splitting algorithms for solving the nonlinear Schrödinger equation and their instabilities". *Phys. Rev. E* **76**, 056708, (2007).

[40] Siu A. Chin. "Symplectic and energy-conserving algorithms for solving magnetic field trajectories". *Phys. Rev. E* **77**, 066401, (2008).

[41] E. R. Hernández, S. Janecek, M. Kaczmarski, and E. Krotscheck. "Evolution-operator method for density functional theory". *Phys. Rev. B* **75**, 075108, (2007).

[42] Siu A. Chin. "Complete characterization of fourth-order symplectic integrators with extended-linear coefficients". *Phys. Rev. E* **73**, 026705, (2006).

[43] Siu A. Chin. "A fundamental theorem on the structure of symplectic integrators". *Physics Letters A* **354**, 373–376, (2006). ISSN: 0375-9601.

[44] Sergio Blanes, Fernando Casas, and J. M. Sanz-Serna. "Numerical Integrators for the Hybrid Monte Carlo Method". *SIAM Journal on Scientific Computing* **36**, A1556–A1580, (2014).

[45] L. Brualla. "Path integral Monte Carlo. Algorithms and applications to quantum fluids". PhD thesis. Universitat Politècnica de Catalunya, 2002.

[46] D. M. Ceperley. "Path-integral calculations of normal liquid ^{3}He". *Phys. Rev. Lett.* **69**, 331–334, (1992).

[47] Massimo Boninsegni. "Permutation Sampling in Path Integral Monte Carlo". *Journal of Low Temperature Physics* **141**, 27–46, (2005). ISSN: 1573-7357.

[48] N.V Prokof'ev, B.V Svistunov, and I.S Tupitsyn. ""Worm" algorithm in quantum Monte Carlo simulations". *Physics Letters A* **238**, 253–257, (1998). ISSN: 0375-9601.

[49] Massimo Boninsegni, Nikolay Prokof'ev, and Boris Svistunov. "Worm Algorithm for Continuous-Space Path Integral Monte Carlo Simulations". *Phys. Rev. Lett.* **96**, 070601, (2006).

[50] S. Pilati. "Studies of ultracold gases using quantum Monte Carlo techniques". PhD thesis. Università degli studi di Trento, 2008.

[51] R. Rota. "Path Integral Monte Carlo and Bose-Einstein condensation in quantum fluids and solids". PhD thesis. Universitat Politècnica de Catalunya, 2011.

[52] M. F. Herman, E. J. Bruskin, and B. J. Berne. "On path integral Monte Carlo simulations". *The Journal of Chemical Physics* **76**, 5150–5155, (1982).

[53] Minoru Takahashi and Masatoshi Imada. "Monte Carlo Calculation of Quantum Systems". *Journal of the Physical Society of Japan* **53**, 963–974, (1984).

[54] F. R. Krajewski and M. H. Müser. "Comparison of two non-primitive methods for path integral simulations: Higher-order corrections versus an effective propagator approach". *Phys. Rev. B* **65**, 174304, (2002).

[55] E. L. Pollock and D. M. Ceperley. "Path-integral computation of superfluid densities". *Phys. Rev. B* **36**, 8343–8352, (1987).

[56] G. F. Giuliani and G. Vignale. *Quantum Theory of the Electron Liquid*. Cambridge: Cambridge University Press, 2005.

[57] D. M. Ceperley. "Introduction to Quantum Monte Carlo Methods Applied to the Electron Gas". In: *Proceedings of the International School of Physics Enrico Fermi*. (Amsterdam). Ed. by G. F. Giuliani and G. Vignale. Course CLVII. IOS Press, 2004. 3–42.

[58] S. Tomonaga. "Remarks on Bloch's Method of Sound Waves applied to Many-Fermion Problems". *Prog. Theor. Phys.* **5**, 544–569, (1950).

[59] J. M. Luttinger. "An Exactly Soluble Model of a Many-Fermion System". *Journal of Mathematical Physics* **4**, 1154–1162, (1963).

[60] F D M Haldane. "'Luttinger liquid theory' of one-dimensional quantum fluids. I. Properties of the Luttinger model and their extension to the general 1D interacting spinless Fermi gas". *Journal of Physics C: Solid State Physics* **14**, 2585, (1981).

[61] H. J. Schulz. "Wigner crystal in one dimension". *Phys. Rev. Lett.* **71**, 1864–1867, (1993).

[62] Michael M. Fogler. "Short-range correlations and spin-mode velocities in ultrathin one-dimensional conductors". *Phys. Rev. B* **71**, 161304, (2005).

[63] Michael M. Fogler and Eugene Pivovarov. "Exchange interaction in quantum rings and wires in the Wigner-crystal limit". *Phys. Rev. B* **72**, 195344, (2005).

[64] J. P. Pouget, S. K. Khanna, F. Denoyer, R. Comès, A. F. Garito, and A. J. Heeger. "X Ray Observation of $2k_F$ and $4k_F$ Scatterings in Tetrathiafulvalene-Tetracyanoquinodimethane (TTF-TCNQ)". *Phys. Rev. Lett.* **37**, 437–440, (1976).

[65] A. R. Goñi, A. Pinczuk, J. S. Weiner, J. M. Calleja, B. S. Dennis, L. N. Pfeiffer, and K. W. West. "One-dimensional plasmon dispersion and dispersionless intersubband excitations in GaAs quantum wires". *Phys. Rev. Lett.* **67**, 3298–3301, (1991).

[66] O. M. Auslaender, A. Yacoby, R. de Picciotto, K. W. Baldwin, L. N. Pfeiffer, and K. W. West. "Tunneling Spectroscopy of the Elementary Excitations in a One-Dimensional Wire". *Science* **295**, 825–828, (2002). ISSN: 0036-8075.

[67] B. J. Kim, H. Koh, E. Rotenberg, S.-J. Oh, H. Eisaki, N. Motoyama, S. Uchida, T. Tohyama, S. Maekawa, Z.-X. Shen, and C. Kim. "Distinct spinon and holon dispersions in photoemission spectral functions from one-dimensional $SrCuO_2$". *Nature Physics* **2**, 397–401, (2006).

[68] Y. Jompol, C. J. B. Ford, J. P. Griffiths, I. Farrer, G. A. C. Jones, D. Anderson, D. A. Ritchie, T. W. Silk, and A. J. Schofield. "Probing Spin-Charge Separation in a Tomonaga-Luttinger Liquid". *Science* **325**, 597–601, (2009). ISSN: 0036-8075.

[69] D. Laroche, G. Gervais, M. P. Lilly, and J. L. Reno. "1D-1D Coulomb Drag Signature of a Luttinger Liquid". *Science* **343**, 631–634, (2014). ISSN: 0036-8075.

[70] V.V. Deshpande and M. Bockrath. "The one-dimensional Wigner crystal in carbon nanotubes". *Nature Physics* **4**, 314–318, (2008).

[71] B. Szafran, F. M. Peeters, S. Bednarek, T. Chwiej, and J. Adamowski. "Spatial ordering of charge and spin in quasi-one-dimensional Wigner molecules". *Phys. Rev. B* **70**, 035401, (2004).

[72] Erich J. Mueller. "Wigner crystallization in inhomogeneous one-dimensional wires". *Phys. Rev. B* **72**, 075322, (2005).

[73] Michele Casula, Sandro Sorella, and Gaetano Senatore. "Ground state properties of the one-dimensional Coulomb gas using the lattice regularized diffusion Monte Carlo method". *Phys. Rev. B* **74**, 245427, (2006).

[74] Luke Shulenburger, Michele Casula, Gaetano Senatore, and Richard M. Martin. "Correlation effects in quasi-one-dimensional quantum wires". *Phys. Rev. B* **78**, 165303, (2008).

[75] R. M. Lee and N. D. Drummond. "Ground-state properties of the one-dimensional electron liquid". *Phys. Rev. B* **83**, 245114, (2011).

[76] A. D. Gü çlü, C. J. Umrigar, Hong Jiang, and Harold U. Baranger. "Localization in an inhomogeneous quantum wire". *Phys. Rev. B* **80**, 201302, (2009).

[77] G. E. Astrakharchik and M. D. Girardeau. "Exact ground-state properties of a one-dimensional Coulomb gas". *Phys. Rev. B* **83**, 153303, (2011).

[78] M. Girardeau. "Relationship between Systems of Impenetrable Bosons and Fermions in One Dimension". *Journal of Mathematical Physics* **1**, 516–523, (1960).

[79] Daniel H. E. Dubin. "Minimum energy state of the one-dimensional Coulomb chain". *Phys. Rev. E* **55**, 4017–4028, (1997).

[80] S. Akhanjee. "Exact longitudinal plasmon dispersion relations for one and two dimensional Wigner crystals". *arXiv:0704.2088v3*, (2007).

[81] Shmuel Fishman, Gabriele De Chiara, Tommaso Calarco, and Giovanna Morigi. "Structural phase transitions in low-dimensional ion crystals". *Phys. Rev. B* **77**, 064111, (2008).

[82] Christophe Mora, Olivier Parcollet, and Xavier Waintal. "Quantum melting of a crystal of dipolar bosons". *Phys. Rev. B* **76**, 064511, (2007).

[83] G. E. Astrakharchik and Yu. E. Lozovik. "Super-Tonks-Girardeau regime in trapped one-dimensional dipolar gases". *Phys. Rev. A* **77**, 013404, (2008).

[84] B. M. Kim, T. Brintlinger, E. Cobas, M. S. Fuhrer, Haimei Zheng, Z. Yu, R. Droopad, J. Ramdani, and K. Eisenbeiser. "High-performance carbon nanotube transistors on SrTiO3/Si substrates". *Applied Physics Letters* **84**, 1946–1948, (2004).

[85] S. M. Apenko. "Critical temperature of the superfluid transition in Bose liquids". *Phys. Rev. B* **60**, 3052–3055, (1999).

[86] O. N. Osychenko, R. Rota, and J. Boronat. "Superfluidity of metastable glassy bulk para-hydrogen at low temperature". *Phys. Rev. B* **85**, 224513, (2012).

[87] Matthias Kühnel, José M. Fernández, Guzmán Tejeda, Anton Kalinin, Salvador Montero, and Robert E. Grisenti. "Time-Resolved Study of Crystallization in Deeply Cooled Liquid Parahydrogen". *Phys. Rev. Lett.* **106**, 245301, (2011).

[88] P. E. Sokol, R. T. Azuah, M. R. Gibbs, and S. M. Bennington. "A neutron scattering study of hydrogen in vycor glass". *J. Low Temp. Phys.* **103**, 23–33, (1996).

[89] Kirill Kuyanov-Prozument and Andrey F. Vilesov. "Hydrogen Clusters that Remain Fluid at Low Temperature". *Phys. Rev. Lett.* **101**, 205301, (2008).

[90] R. E. Grisenti, R. A. Costa Fraga, N. Petridis, R. Dörner, and J. Deppe. "Cryogenic microjet for exploration of superfluidity in highly supercooled molecular hydrogen". *Europhys. Lett.* **73**, 540–546, (2006).

[91] M. C. Gordillo and D. M. Ceperley. "Superfluidity in H_2 Films". *Phys. Rev. Lett.* **79**, 3010–3013, (1997).

[92] Claudio Cazorla and Jordi Boronat. "Possible superfluidity of molecular hydrogen in a two-dimensional crystal phase of sodium". *Phys. Rev. B* **88**, 224501, (2013).

[93] Massimo Boninsegni. "Theoretical study of H_2 in a two-dimensional crystalline matrix". *New Journal of Physics* **7**, 78, (2005).

[94] C. Cazorla and J. Boronat. "Quantum Monte Carlo study of two-dimensional H2 on a Rb substrate". *Journal of Low Temperature Physics* **134**, 43–48, (2004).

[95] Massimo Boninsegni. "Absence of superfluidity in a parahydrogen film intercalated within a crystal of Na atoms". *Phys. Rev. B* **93**, 054507, (2016).

[96] Philippe Sindzingre, David M. Ceperley, and Michael L. Klein. "Superfluidity in clusters of p-H_2 molecules". *Phys. Rev. Lett.* **67**, 1871–1874, (1991).

[97] Fabio Mezzacapo and Massimo Boninsegni. "Superfluidity and Quantum Melting of $p-H_2$ Clusters". *Phys. Rev. Lett.* **97**, 045301, (2006).

[98] Fabio Mezzacapo and Massimo Boninsegni. "Structure, superfluidity, and quantum melting of hydrogen clusters". *Phys. Rev. A* **75**, 033201, (2007).

[99] S. A. Khairallah, M. B. Sevryuk, D. M. Ceperley, and J. P. Toennies. "Interplay between Magic Number Stabilities and Superfluidity of Small Parahydrogen Clusters". *Phys. Rev. Lett.* **98**, 183401, (2007).

[100] Fabio Mezzacapo and Massimo Boninsegni. "Local Superfluidity of Parahydrogen Clusters". *Phys. Rev. Lett.* **100**, 145301, (2008).

[101] E. Sola and J. Boronat. "Solidification of Small p-H2 Clusters at Zero Temperature". *The Journal of Physical Chemistry A* **115**, PMID: 21375238, 7071–7076, (2011).

[102] R. Guardiola and J. Navarro. "A diffusion Monte Carlo study of small para-hydrogen clusters". *Central European Journal of Physics* **6**, 33–37, (2008).

[103] Javier Eduardo Cuervo and Pierre-Nicholas Roy. "Path integral ground state study of finite-size systems: Application to small (parahydrogen)N (N=2–20) clusters". *The Journal of Chemical Physics* **125**, 124314, (2006).

[104] Javier Eduardo Cuervo and Pierre-Nicholas Roy. "On the solid- and liquidlike nature of quantum clusters in their ground state". *The Journal of Chemical Physics* **128**, 224509, (2008).

[105] Javier Eduardo Cuervo and Pierre-Nicholas Roy. "Weakly bound complexes trapped in quantum matrices: Structure, energetics, and isomer coexistence in (para-H2)N(ortho-D2)3 clusters". *The Journal of Chemical Physics* **131**, 114302, (2009).

[106] Yongkyung Kwon and K. Birgitta Whaley. "Nanoscale Molecular Superfluidity of Hydrogen". *Phys. Rev. Lett.* **89**, 273401, (2002).

[107] F. Paesani, R. E. Zillich, Y. Kwon, and K. B. Whaley. "OCS in para-hydrogen clusters: Rotational dynamics and superfluidity". *The Journal of Chemical Physics* **122**, 181106, (2005).

[108] Yongkyung Kwona and K. Birgitta Whaleyb. "Superfluid Response in OCS(H2)5 and OCS(D2)5". *Journal of Low Temperature Physics* **140**, 227–240, (2005). ISSN: 1573-7357.

[109] M. C. Gordillo, J. Boronat, and J. Casulleras. "Zero-Temperature Equation of State of Quasi-One-Dimensional H_2". *Phys. Rev. Lett.* **85**, 2348–2351, (2000).

[110] Maurizio Rossi and Francesco Ancilotto. "Superfluid behavior of quasi-one-dimensional $p-H_2$ inside a carbon nanotube". *Phys. Rev. B* **94**, 100502, (2016).

[111] Tokunbo Omiyinka and Massimo Boninsegni. "Quasi-one-dimensional parahydrogen in nanopores". *Phys. Rev. B* **93**, 104501, (2016).

[112] F. D. M. Haldane. "Effective Harmonic-Fluid Approach to Low-Energy Properties of One-Dimensional Quantum Fluids". *Phys. Rev. Lett.* **47**, 1840–1843, (1981).

[113] M. A. Cazalilla. "Bosonizing one-dimensional cold atomic gases". *Journal of Physics B: Atomic, Molecular and Optical Physics* **37**, S1, (2004).

[114] T. Giamarchi. *Quantum Physics in One Dimension*. Oxford: Oxford University Press, 2004.

[115] Adilet Imambekov, Thomas L. Schmidt, and Leonid I. Glazman. "One-dimensional quantum liquids: Beyond the Luttinger liquid paradigm". *Rev. Mod. Phys.* **84**, 1253–1306, (2012).

[116] Isaac F. Silvera and Victor V. Goldman. "The isotropic intermolecular potential for H2 and D2 in the solid and gas phases". *The Journal of Chemical Physics* **69**, 4209–4213, (1978).

[117] J. Breton, J. Gonzalez-Platas, and C. Girardet. "Endohedral adsorption in graphitic nanotubules". *The Journal of Chemical Physics* **101**, 3334–3340, (1994).

[118] George Stan and Milton W. Cole. "Low coverage adsorption in cylindrical pores". *Surface Science* **395**, 280–291, (1998). ISSN: 0039-6028.

[119] S. W. Lovesey. *Condensed Matter Physics: dynamic correlations*. Sant Francisco: Benjamin-Cummings, 1986.

[120] Henry R. Glyde. *Excitations in Liquid and Solid Helium*. Oxford: Oxford University Press, 1994.

[121] K H Andersen, W G Stirling, R Scherm, A Stunault, B Fak, H Godfrin, and A J Dianoux. "Collective excitations in liquid 4 He: I. Experiment and presentation of data". *Journal of Physics: Condensed Matter* **6**, 821, (1994).

[122] B. Fåk and J. Bossy. "Excitations and Their Temperature Dependence in Superfluid 4He Beyond the Roton". *Journal of Low Temperature Physics* **113**, 531–536, (1998). ISSN: 1573-7357.

[123] H. R. Glyde, M. R. Gibbs, W. G. Stirling, and M. A. Adams. "Excitations in superfluid 4 He beyond the roton". *EPL (Europhysics Letters)* **43**, 422, (1998).

[124] M R Gibbs, K H Andersen, W G Stirling, and H Schober. "The collective excitations of normal and superfluid: the dependence on pressure and temperature". *Journal of Physics: Condensed Matter* **11**, 603, (1999).

[125] J V Pearce, R T Azuah, B Fåk, A R Sakhel, H R Glyde, and W G Stirling. "High-resolution measurements of excitations in superfluid 4 He beyond the roton". *Journal of Physics: Condensed Matter* **13**, 4421, (2001).

[126] A. R. Sakhel and H. R. Glyde. "Excitations and Bose-Einstein condensation in liquid ^{4}He". *Phys. Rev. B* **70**, 144511, (2004).

[127] S. Fantoni A. Fabrocini and E. Krotscheck. *Introduction to Modern Methods of Quantum Many-Body Theory and their Applications*. Vol. 7. Advances in Quantum Many-Body Theory. Singapore: World Scientific, 2002.

[128] C. E. Campbell, E. Krotscheck, and T. Lichtenegger. "Dynamic many–body theory: Multiparticle fluctuations and the dynamic structure of ^{4}He". *Phys. Rev. B* **91**, 184510, (2015).

[129] K. Beauvois, C. E. Campbell, J. Dawidowski, B. Fåk, H. Godfrin, E. Krotscheck, H.-J. Lauter, T. Lichtenegger, J. Ollivier, and A. Sultan. "Superfluid ^{4}He dynamics beyond quasiparticle excitations". *Phys. Rev. B* **94**, 024504, (2016).

[130] J. Kaipio and E. Somersalo. *Statistical and Computational Inverse Problems*. New York: Springer-Verlag, 2004.

[131] Mark Jarrell and J.E. Gubernatis. "Bayesian inference and the analytic continuation of imaginary-time quantum Monte Carlo data". *Physics Reports* **269**, 133–195, (1996). ISSN: 0370-1573.

[132] Anders W. Sandvik. "Stochastic method for analytic continuation of quantum Monte Carlo data". *Phys. Rev. B* **57**, 10287–10290, (1998).

[133] A. S. Mishchenko, N. V. Prokof'ev, A. Sakamoto, and B. V. Svistunov. "Diagrammatic quantum Monte Carlo study of the Fröhlich polaron". *Phys. Rev. B* **62**, 6317–6336, (2000).

[134] N. V. Prokof'ev and B. V. Svistunov. "Spectral analysis by the method of consistent constraints". *JETP Letters* **97**, 649–653, (2013). ISSN: 1090-6487.

[135] E. Vitali, M. Rossi, L. Reatto, and D. E. Galli. "Ab initio low-energy dynamics of superfluid and solid ^{4}He". *Phys. Rev. B* **82**, 174510, (2010).

[136] R. Rota, J. Casulleras, F. Mazzanti, and J. Boronat. "Quantum Monte Carlo estimation of complex-time correlations for the study of the ground-state dynamic structure function". *The Journal of Chemical Physics* **142**, 114114, (2015).

[137] A. N. Tikhonov. "On the solution of ill-posed problems and the method of regularization". *Soviet Math. Dokl.* **4**, 1035–1038, (1963).

[138] Alessandro Roggero, Francesco Pederiva, and Giuseppina Orlandini. "Dynamical structure functions from quantum Monte Carlo calculations of a proper integral transform". *Phys. Rev. B* **88**, 094302, (2013).

[139] P. Kevin MacKeown. *Stochastic Simulation in Physics*. Singapore: Springer, 1997.

[140] Akira Nakayama and Nancy Makri. "Simulation of dynamical properties of normal and superfluid helium". *Proceedings of the National Academy of Sciences of the United States of America* **102**, 4230–4234, (2005).

[141] Massimo Boninsegni and David M. Ceperley. "Density fluctuations in liquid4He. Path integrals and maximum entropy". *Journal of Low Temperature Physics* **104**, 339–357, (1996). ISSN: 1573-7357.

[142] J Gavoret and P Nozières. "Structure of the perturbation expansion for the bose liquid at zero temperature". *Annals of Physics* **28**, 349–399, (1964). ISSN: 0003-4916.

[143] P. E. Sokol. In: *Bose-Einstein Condensation*. Ed. by D. W. Snoke A. Griffin and S. Stringari. Cambridge: Cambridge University Press, 1995. 51.

[144] E. Manousakis, V. R. Pandharipande, and Q. N. Usmani. "Condensate fraction and momentum distribution in the ground state of liquid ^{4}He". *Phys. Rev. B* **31**, 7022–7028, (1985).

[145] Saverio Moroni, Gaetano Senatore, and Stefano Fantoni. "Momentum distribution of liquid helium". *Phys. Rev. B* **55**, 1040–1049, (1997).

[146] R. Rota and J. Boronat. "Condensate Fraction in Liquid 4He at Zero Temperature". *Journal of Low Temperature Physics* **166**, 21–32, (2012). ISSN: 1573-7357.

[147] Ronald A. Aziz, Frederick R.W. McCourt, and Clement C.K. Wong. "A new determination of the ground state interatomic potential for He2". *Molecular Physics* **61**, 1487–1511, (1987).

[148] F. Mezei. "High-Resolution Study of Excitations in Superfluid ^{4}He by the Neutron Spin-Echo Technique". *Phys. Rev. Lett.* **44**, 1601–1604, (1980).

[149] L. D. Landau and I. M. Khalatnikov. "The theory of viscosity of helium II. II. Calculation of the viscosity coefficient". *Zh. Eksp. Teor. Fiz.* **19**, 637, (1949).

[150] R. A. Cowley and A. D. B. Woods. "Inelastic Scattering of Thermal Neutrons from Liquid Helium". *Canadian Journal of Physics* **49**, 177–200, (1971).

[151] A D B Woods and R A Cowley. "Structure and excitations of liquid helium". *Reports on Progress in Physics* **36**, 1135, (1973).

[152] E. C. Svensson, V. F. Sears, A. D. B. Woods, and P. Martel. "Neutron-diffraction study of the static structure factor and pair correlations in liquid ^{4}He". *Phys. Rev. B* **21**, 3638–3651, (1980).

[153] Frédéric Caupin, Jordi Boronat, and Ken H. Andersen. "Static Structure Factor and Static Response Function of Superfluid Helium 4: a Comparative Analysis". *Journal of Low Temperature Physics* **152**, 108–121, (2008). ISSN: 1573-7357.

[154] P. Schofield. "Space-Time Correlation Function Formalism for Slow Neutron Scattering". *Phys. Rev. Lett.* **4**, 239–240, (1960).

[155] D. Thirumalai and B. J. Berne. "Time correlation functions in quantum systems". *The Journal of Chemical Physics* **81**, 2512–2513, (1984).

[156] Nilmadhab Chakrabarti, Tucker Carrington Jr, and Benoît Roux. "Rate constants in quantum mechanical systems: A rigorous and practical path-integral formulation for computer simulations". *Chemical Physics Letters* **293**, 209–220, (1998). ISSN: 0009-2614.

[157] Goran Krilov, Eunji Sim, and B. J. Berne. "Quantum time correlation functions from complex time Monte Carlo simulations: A maximum entropy approach". *The Journal of Chemical Physics* **114**, 1075–1088, (2001).

[158] Eunji Sim, Goran Krilov, and B. J. Berne. "Quantum Rate Constants from Short-Time Dynamics: An Analytic Continuation Approach". *The Journal of Physical Chemistry A* **105**, 2824–2833, (2001).

[159] Goran Krilov, Eunji Sim, and B.J. Berne. "On the Bayesian approach to calculating time correlation functions in quantum systems; reaction dynamics and spectroscopy". *Chemical Physics* **268**, 21–34, (2001). ISSN: 0301-0104.

[160] Akira Nakayama and Nancy Makri. "Symmetrized correlation function for liquid para-hydrogen using complex-time pair-product propagators". *The Journal of Chemical Physics* **125**, 024503, (2006).

[161] Jeb Kegerreis, Akira Nakayama, and Nancy Makri. "Complex-time velocity autocorrelation functions for Lennard-Jones fluids with quantum pair-product propagators". *The Journal of Chemical Physics* **128**, 184509, (2008).

[162] Vikram Jadhao and Nancy Makri. "Iterative Monte Carlo for quantum dynamics". *The Journal of Chemical Physics* **129**, 161102, (2008).

[163] S. Bonella, M. Monteferrante, C. Pierleoni, and G. Ciccotti. "Path integral based calculations of symmetrized time correlation functions. I." *The Journal of Chemical Physics* **133**, 164104, (2010).

[164] S. Bonella, M. Monteferrante, C. Pierleoni, and G. Ciccotti. "Path integral based calculations of symmetrized time correlation functions. II." *The Journal of Chemical Physics* **133**, 164105, (2010).

[165] Robert E. Zillich, Johannes M. Mayrhofer, and Siu A. Chin. "Extrapolated high-order propagators for path integral Monte Carlo simulations". *The Journal of Chemical Physics* **132**, 044103, (2010).

[166] S. W. Lovesey. *Theory of Neutron Scattering from Condensed Matter*. Vol. 1. Oxford: Clarendon Press, 1984.

Acknowledgements

First of all, I would like to thank my advisor, Prof. Jordi Boronat, whose continued support was vital in the development of this thesis. Jordi introduced me to Quantum Monte Carlo methods during my years as a master's student, six years ago, and from then forwards I have not stopped learning from him. Jordi provides advice and guidance when needed, otherwise giving the student freedom to tackle the difficulties on its own way. That, and his cheerful and gentle nature have made working with him daily a very rewarding experience.

I am also very grateful to all the other professorate of the Barcelona Quantum Monte Carlo group, Dr. Joaquim Casulleres, Dr. Ferran Mazzanti and Dr. Grigory Astrakharchik for all the help, guidance and useful discussions provided during all these years. I must also thank all the other professors, researchers and staff of the Departament de Física of the Universitat Politècnica de Catalunya. All of them contribute to the friendly and easygoing atmosphere that reigns in the department.

During all these years I have learned a lot of new things, not all of them related to this thesis' contents, that made me grow as a person both professionally and personally. Part of this comes from the people with whom I interacted daily. Like Oleg and Jonas, that welcomed me into their office. Grigory, for making me discover new fruits. Alfredo, for showing me the inner misteries of the *inca2* cluster. Andrés, for being such an excellent office partner. Ausias, for being a great roommate and friend before, during and after this stage of my life. Jordi, for helping each other as stress relievers. Also, to all the others that arrived here after me. Grecia and Juan for keeping the work environment in the office when needed, and for all both useful and casual conversations during this short time. And to Raul for being able to understand my coding style without going insane.

Finally, I must thank all my family. More concretely my mother Montserrat, for always caring about the state of this thesis, despite not being able to remem-

ber exactly the name of what I was doing. To my father Albert, from whom I inherited the passion for programming. And to Raquel, for being my partner during all this journey and giving me her support in times of need.